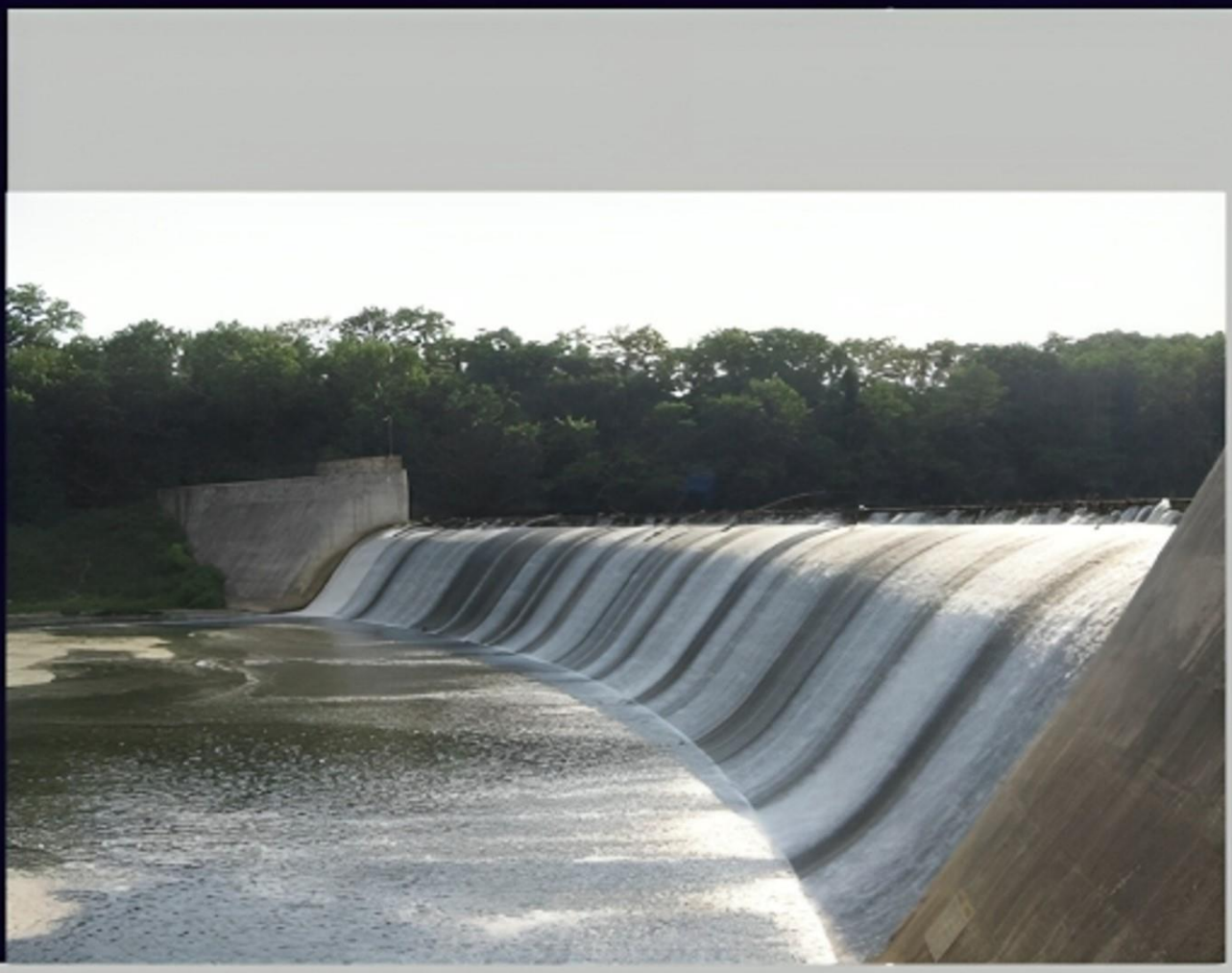
Iranian Hydraulic Association

Shahid Chamran University of Ahvaz

Journal of Hydraulic Structures

Scientific Professional Journal



October 2024
Volume 10, Issue 4

ISSN (Online): 2345-4156
https://jhs.scu.ac.ir/

Aims and Scope

Journal of Hydraulic Structures is an interdisciplinary journal which publishes high-quality peer-reviewed articles addressing the latest developments and applied methods in analysis and design, construction, maintenance, management, and operation policy of Hydraulic Structures.

The Journal aims at providing an efficient route to fast-track publication, within 10-12 weeks after manuscript submission.

The general areas covered by the Journal include:

- Advances in numerical and analytical methods applicable to hydraulic structures
- Hydro informatics and soft computing
- Hydraulic aspects of hydraulic structures
- Applied surface and subsurface hydrology and hydrometeorology
- Forecasting approaches in water resources engineering
- Economic and social aspects of hydraulic structures
- Uncertainty analysis and risk management in hydraulics and water resources engineering
- Application of Nanotechnology in hydraulic structures
- Geotechnics of hydraulic structures
- Damage detection techniques
- Technical and methodological advances in application, design/selection, production, construction materials of hydraulic structures.
- Application of Artificial Intelligence techniques in all aspects of hydraulic structures.

General Information:

Title: Journal of Hydraulic Structures

Publisher: Shahid Chamran University of Ahvaz

ISSN (Print): 2345-413X

ISSN (Online): 2345-4156

Website: https://jhs.scu.ac.ir/

Address: Faculty of Civil Engineering and Architecture, Shahid Chamran University of Ahvaz, Ahvaz, Iran

Email: jhs@scu.ac.ir

Journal of

Hydraulic Structures

Shahid Chamran University of Ahvaz

Director-in-Charge: Prof. Ali Haghighi

Editor-in-Chief: Prof. Hamid R. Ghafouri

Managing Editor: Dr. Amir H. Shafiee

Contents:

01

Comparative Assessment of the Computational Fluid Dynamics and Artificial Intelligence Methods for the Prediction of 3D Flow Field around a Single Straight Groyne

Akbar Safarzadeh; Fariborz Masoumi; Zolfaghar Safarzadeh; Maryam Abdoli

26

Adsorption characteristics of NH2-UiO-66 for the removal of hematite inorganic dye from industrial wastewater: Isotherm, thermodynamic, and kinetic study

Abbas Mohammadi; Mehdi Sedighi

46

Experimental study of river morphology downstream of the inclined and vertical grade control structures

Seyed Mohamad Mahdi Shariati; Mehdi Hamidi

61

Prediction of Manning Coefficient in Compound Channels with Converged and Diverged Floodplains using GMDH Model

Sajad Bijanvand; Mirali Mohammadi; Abbas Parsaie

82

Advanced Soft Computing Ensemble for Modeling Contaminant Transport in River Systems: A Comparative Analysis and Ecological Impact Assessment

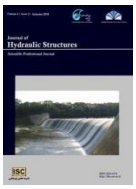
Jafar Chabokpour

97

Optimization of creep function parameters of viscoelastic pipelines based on transient pressure signal

Ebrahim Sharififard; Mohammad Azizipour; Javad Ahadiyan; Ali Haghighi

Journal of Hydraulic Structures
J. Hydraul. Struct., 2024;10(4):1-25
DOI: 10.22055/jhs.2024.46764.1295



OPEN ACCESS

Comparative Assessment of the Computational Fluid Dynamics and Artificial Intelligence Methods for the Prediction of 3D Flow Field around a Single Straight Groyne

Akbar Safarzadeh [*1]
Fariborz Masoumi [1]
Zolfaghar Safarzadeh [2]
Maryam Abdoli [1]

Abstract

In this research, we investigated the three-dimensional time averaged flow pattern around a single straight groyne. To measure the three-dimensional velocity components in the laboratory, we utilized an Acoustic Doppler Velocimeter (ADV). We employed Computational Fluid Dynamics (CFD) and Artificial Neural Network (ANN) techniques to simulate the crucial flow characteristics. To validate these methods, we compared the simulation results with the measured data. The findings demonstrate that the ANN approach, with R2 values of 0.9152, 0.9150, and 0.9315, outperforms the CFD model, with R2 values of 0.8332, 0.8726, and 0.8051, in the prediction of the u and v velocity components as well as the velocity magnitude. The transverse velocity profiles indicate that the ANN method accurately predicts the velocity components and velocity magnitude, whereas the CFD method exhibits significant disparities from the measured data, particularly in the prediction of longitudinal and vertical velocity components, especially in the near-bed regions. The ANN method and the laboratory data display variations in their patterns across the shear layer and at the flow separation boundary, while the velocity profiles in the CFD method demonstrate a consistent increase from the right wall of the channel toward the main flow zone. Other flow features around the groyne, such as horseshoe vortex, secondary flow, clockwise and counterclockwise rotational flows around the groyne head and the length and precise center of the circulation zone are reasonably predicted by the ANN method. Furthermore, the ANN method accurately predicts increased velocity in the transverse direction around the groyne head and identifies two regions of amplified velocity magnitude at the cross sections downstream of the groyne in velocity magnitude contour plots. However, the values simulated by the CFD method deviate from the laboratory data.

Keywords: Groyne, Computational Fluid Dynamics, Artificial Intelligence, Horseshoe Vortex

Received: 29 April 2024; Accepted: 12 July 2024

[*] E-mail: safarzadeh@uma.ac.ir (**Corresponding Author**)
[1] Department of Civil Engineering, University of Mohaghegh Ardabili, Ardabil, Iran.
[2] Department of Civil Engineering, Ardabil branch, Islamic Azad University, Ardabil, Iran.

1. Introduction

A crucial topic in river engineering involves the erosion of river banks and its consequential impacts. This process leads to the loss of land along the riverbanks and poses a threat to nearby establishments. One primary approach to altering the river's course involves the installation of flow diversion structures, such as river groynes. Groynes, constructed from materials like riprap, gabions, or a mix of riverbed and riprap or gabion cover, are either permeable or impermeable structures. They function as a series of walls, implemented either sequentially or individually, to redirect high velocity flow away from the riverbanks. They are widely employed to safeguard outer walls in meanders, facilitate path modification, and reduce the width of the river. Furthermore, by generating low velocity circulation zones around and downstream of them, groynes promote sediment deposition near the primary shore, gradually fostering the natural development and stabilization of the riverbanks.

Despite their simple design, the construction of groynes gives rise to intricate 3D turbulent flows around them. The direct interaction of the flow with the groyne leads to the development of various vortices, giving rise to low velocity circulation zone and the formation of a wake zone in a short length upstream and a large circulation zone downstream. The presence of these phenomena, along with turbulent eddies resulting from shear layer oscillations, contributes to the complexities of the flow around the groyne.

The earliest laboratory study on groynes was carried out by Ahmad [1]. Koken & Constantinescu [2] conducted extensive research on the 3D flow structure (average and instantaneous) around a single groyne situated in a straight channel under both flat and developed bed conditions. In their study, they employed Large Eddy Simulation (LES) method for flow modeling. The researchers highlighted the significance of both local velocity amplification around the groyne head and the formation of horseshoe vortex in bed shear stress amplification.

Koken & Constantinescu [3] further examined the flow structure around a single groyne, investigating the impact of the developed bed on the formation of vortex flows and bed shear stress distribution. They concluded that the horseshoe vortex structure is more stable in a flatbed condition and significantly more complex in the instantaneous structure in the developed bed condition. Additionally, Koken & Constantinescu [4] explored the flow around a lateral obstacle using the Detached Eddy Simulation (DES) method. The primary finding of this research is the variation in the size of Separated Shear layer (SSL) vortices with changes in Reynolds number.
Duan [5] conducted a study on the average and turbulent flow structures around a straight groyne in a laboratory channel with a flat bed. In another publication by Duan et al. [6], the researchers explored the impact of a scoured hole on average and turbulent flow structures.

Koken [7] used the DES method with a Reynolds number of 45000 to study the flow around groynes with varying attachment angles (60°, 90°, 120°). The findings revealed notable variations in the size, coherence, and direction of the horseshoe vortex around the groyne.

Safarzadeh et al. [8] conducted simulations of turbulent flow in a laboratory channel and investigated the impact of altering groyne shape by using two different T-shaped groynes. The experimental findings suggest that groyne shape exerts a substantial influence on the characteristics of both average and turbulent flows, particularly in areas close to the channel bed. Safarzadeh & Brevis [9] emphasized the significance of assessing the reliability of existing numerical models for simulations and evaluated the effectiveness of Reynolds-averaged Navier-Stokes (RANS) models in predicting flow structure in a shallow open channel with a lateral obstruction. The turbulence models RSM, and were chosen for this investigation. The comparative findings revealed that the RSM model successfully predicted the length of the main

vortex area, whereas the other two models exhibited significant limitations.

Jeongsook Jeon and colleagues [10] carried out a set of laboratory investigations to analyze the flow dynamics around a rectangular groyne in an open channel. Among their key observations was the notable influence of the horseshoe vortex on the flow pattern surrounding the groyne.

Although previous studies have shown advanced performance of numerical simulations, a comprehensive numerical model still faces limitations in predicting all aspects of complex 3D flow fields due to inherent assumptions and simplifications in turbulent flow modeling. However, advanced techniques like Large Eddy Simulation (LES) and Detached Eddy Simulation (DES) have been developed, they demand high-performance computational resources for accurately calculating high Reynolds number flows, such as those around river structures. Despite extensive laboratory studies and numerical simulations, accurately simulating all flow field parameters around groynes remains a formidable challenge.

The use of soft computing methods, such as Artificial Neural Network (ANN), Genetic Programming (GP), Genetic Algorithm (GA), and others, stands in contrast to numerical simulations, offering cost-effective and intelligent solutions for complex engineering problems. These methods serve as valuable tools for addressing extensive problems that are not easily solved with traditional rule-based programs and are widely applied across various fields. AI has been employed to predict rainfall intensity [11, 12], forecast floods [13,14], estimate water quality parameters [15-17], predict the local scour depth around hydraulic structures [18-20] and determine hydraulic jump length [21-23]. Their versatility makes soft computing methods a valuable asset in addressing a wide range of water engineering challenges.

It's evident that there has been a recent focus on leveraging soft computing methods for predicting flow fields in open channels. For instance, Yang and Chang [24] assessed the effectiveness of the ANN method in simulating longitudinal velocity profiles and predicting discharge in 90° combined open channels. Additionally, Gholami, A., et al. [25] employed Computational Fluid Dynamics (CFD) and ANN methods to predict 3D flow fields in a 90° curved channel. Ebtehaj & Bonakdari [26] successfully utilized ANN to predict sediment transport in sewer pipes which is a complex phenomenon. Furthermore, Sun et al. [27] evaluated the capability of ANN models in representing and modeling flow velocity distribution of combined open-channel flow using CFD data to construct and test the ANN models. Zaji and Bonakdari [20] applied ANN and GP methods to predict longitudinal velocity field in an open channel junction, and also compared the performance of ANN, GA, and CFD methods in the same channel. Safarzadeh et al., [28] modeled the longitudinal flow field around a single straight groyne of various lengths using two computational methods, GAA and GP. The results indicated that the final chosen GAA model outperformed the final chosen GP model. Safarzadeh et al. [29] investigated the complex 3D flow field around a straight groyne using artificial neural network methods DE-MLP and DE-RBF, demonstrating the capabilities of each method in predicting certain flow field characteristics.

According to the study by Karki et al. [30], the effect of groynes orientation on near-bank flow and morphology was assessed in a natural meander bend using a two-dimensional (2D) numerical simulation. Wu and Qin [31] investigated the influence of flow and sediment transport processes on sedimentation in groyne fields with HLES model. Also, Pourshahbaz et al. [32] simulated the morphology and hydrodynamics around groynes with Flow-3D model. Pandey et al. [33] predicted the maximum scour depth near spur dikes in uniform bed sediment using stacked generalization ensemble tree-based frameworks. Ding et al. [34] investigated the flow characteristics in a mildly meandering channel with a series of groynes. In this paper, the

numerical method based on the Renormalization Group (RNG) model is used to study the effects of groynes. Xie et al. [35] employed numerical simulation to predict the 3D flow structure and turbulence characteristics near permeable spur dike in channels with varying sinuosities.

It appears that the previous studies have focused on either numerical simulations using CFD or soft computing techniques like ANN, but a comprehensive comparative evaluation of these two approaches for the groyne flow features has not been reported in the literature. The main goal of this study is to assess and compare the capabilities of CFD and ANN methods in simulating the complex time-averaged flow structures around a single straight groyne. The results obtained from both methods will be validated using measured datasets.

The details of the laboratory study are presented in the following section. Then, the two mentioned methods are introduced and the settings for each are presented. Finally, the results of each method are compared in detail.

2. Materials and Methods

2.1. Experimental Study

Figure 1 illustrates the laboratory experiments conducted in a flume with a length of 11 meters and a rectangular cross-section with a width and depth of 1 meter. The flume's walls are made of glass, while its bottom is made of Perspex, facilitating comprehensive observation of the 3D flow field from all perspectives. Water entered the tank from below the flume through a head tank containing a curved side and bed transitions. The bed transition is outfitted with three non-submerged guide vanes designed to mitigate lateral flow oscillations upon entry into the channel. Surface waves generated by the inflowing flow are mitigated by a 1.5-meter-long polystyrene plate positioned near the inlet. Additionally, an automated flap weir is installed at the downstream end of the flume to regulate the inflow depth.

The flow rate was measured using the ISOIL-MS2500 flow meter, which has an accuracy of 0.1 l.s-1. Additionally, an ultrasonic sensor with a precision of ±0.1mm was used to gauge the free water surface of the inlet. 3D velocity measurements were carried out using a 10MHz ADV instrument (Nortek, down looking type), which provides an accuracy of 0.5% and a maximum measurement frequency of 200Hz.

To position the ADV and collect data within a predefined non-uniform Cartesian grid, a fully automated traversing system with accuracies of 0.1 mm in the lateral and vertical directions, and 1 millimeter in the longitudinal direction, was utilized. The initial velocity measurements were conducted under uniform flow conditions without a groyne at different sections along the centerline of the channel, indicating full development of the flow at a distance of 8 meters from the channel inlet. In the main study, single straight groynes of different lengths (120, 150, and 200 mm) were placed in the developed section of the channel. These groynes were constructed from Perspex plates that were 1 cm thick and 20 cm high. The specific characteristics of the groynes and the hydraulic conditions of the tests are outlined in Table 1, with Uin and Hin denoting the water depth at the inlet and the bulk velocity, respectively. The inlet discharge was consistently kept at 60 l.s-1 throughout all the experiments.

According to earlier studies, changes in depth and inlet Froude number do not result in significant differences in main flow features, such as the HSV system or flow separation region. However, variations in groyne length have a noticeable effect on both average flow characteristics and turbulence characteristics [16].

The velocity measurements were carried out within non-uniform 3D grids, as shown in Figure 1, using a cartesian coordinate system (X, Y, and Z) to capture time-averaged velocity components

in the x-direction (u), y-direction (v), and z-direction (w). The measurement domain for the flow field extends to 7L upstream of the groyne and 17L downstream of it, where L represents the length of the groyne. The selection of the flow field measurement domain's extent upstream and downstream was based on the groyne's influence on near-bed flow and the recirculation zone. To capture the 3D characteristics of the flow around the tested groynes, measurements were taken on eight horizontal planes. Table 1 presents details of the measurement domains, where Zmax denotes the final horizontal measurement plane. Additionally, Nx, Ny, and Nz represent the number of measurement points in the x, y, and z directions, respectively. The sampling frequency is 100Hz, and the measurement duration at each point is 120 seconds.

The average values of the three velocity components at each measurement point were calculated and used for training and testing the neural network. Additionally, the measured data are used to validate the results of the CFD model.

Table 1: Details of the laboratory tests and geometric specifications of the tested groynes

Experiment code	Groyne length (L)	Inlet water depth (H_{in}) (mm)	$Fr=U_{in}/(gH_{in})^{0.5}$	$Re=U_{in}H_{in}/\nu$	Z_{max} (mm)	($N_x \times N_y \times N_z$)
SG-120-143	120	143	0.35	60,000	81	(20×15×8)
SG-150-143	150	143	0.35	60,000	81	(20×15×8)
SG-200-143	200	143	0.35	60,000	81	(20×15×8)

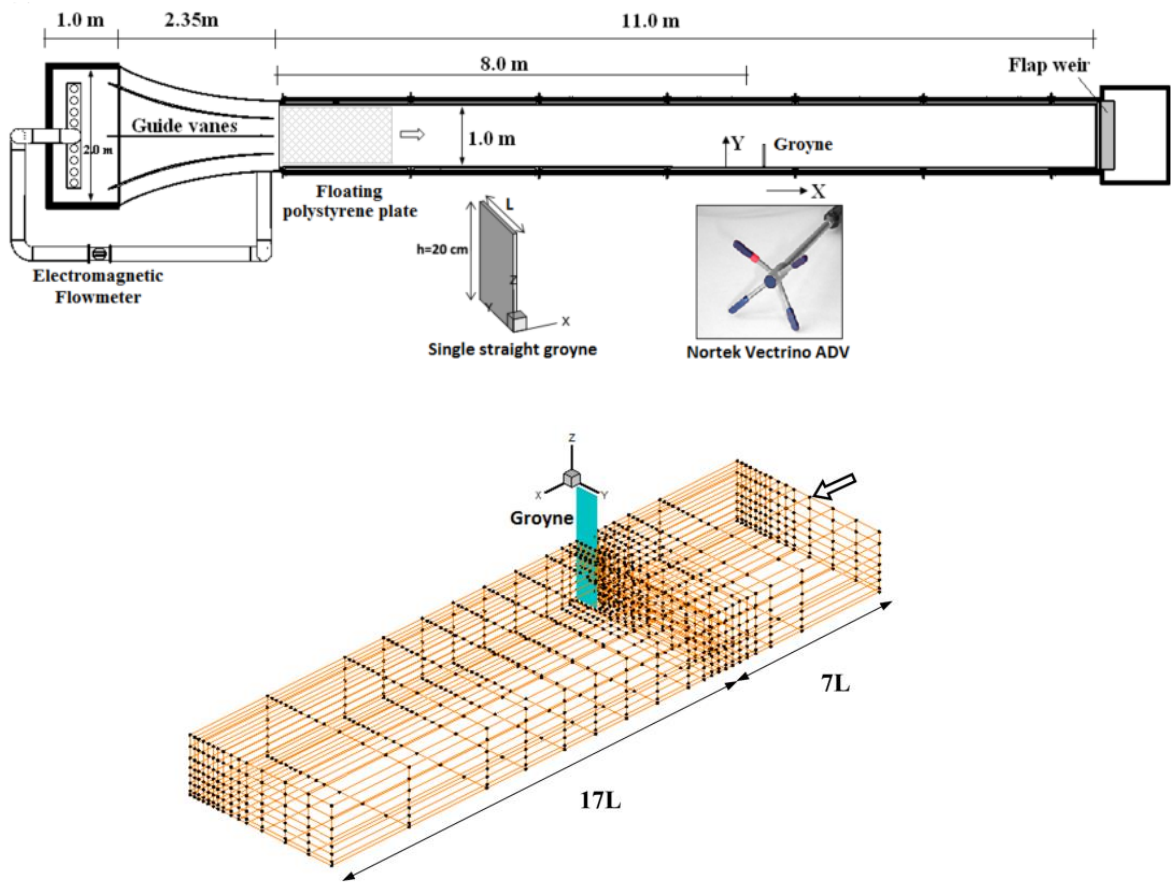


Figure 1. Laboratory flume and 3D measuring grid around a single straight groyne

The iRIC software suite was created in 2014 through a collaboration between Professor Shimizu from Hokkaido University in Japan and Dr. Nelson from the USGS Institute. The aim was to develop software for simulating river flow and morphodynamics. This extensive software includes various subprograms tailored to simulate river phenomena, such as the Nays CUBE subprogram, which was specifically designed for 3D simulation of river hydrodynamics and morphodynamics.

The fundamental equations consist of the time-averaged continuity and momentum equations, which are represented in the Cartesian coordinate system as equations 1 and 2:

$$\frac{\partial U_i}{\partial x_i} = 0 \tag{1}$$

$$\frac{\partial U_i}{\partial t} + \frac{\partial U_i U_j}{\partial x_j} = G_i - \frac{1}{\rho}\frac{\partial p}{\partial x_i} + \frac{\partial\left(-\overline{u_i u_j}\right)}{\partial x_j} + \nu\frac{\partial^2 U_j}{\partial x_j \partial x_j} \tag{2}$$

Where, $U_i$is the velocity component in the x_i Cartesian direction, ρrepresent the fluid density, $p$denotes the pressure and νcorresponds to the kinematic viscosity. On the right-hand side of the equation 2, $G_i$symbolizes the gravitational force per unit volume of the fluid. The term $-\overline{u_i u_j}$ is the Reynolds stress tensor, which is modeled in this software using the Non-linear k-ε turbulence model, as described by equation 3.

$$-\overline{u_i u_j} = \nu_t S_{ij} - \frac{2}{3}k\delta_{ij} - \frac{k}{\varepsilon}\nu_t\left[\alpha_1\left(S_{il}\Omega_{lj} + S_{jl}\Omega_{li}\right) + \alpha_2\left(S_{il}S_{lj} - \frac{1}{3}S_{km}S_{mk}S_{ij}\right)\right] + \alpha_3\left(\Omega_{il}\Omega_{lj} - \frac{1}{3}\Omega_{km}\Omega_{mk}\delta_{ij}\right)\Big] \quad (3)$$

Where, $\nu_t$denotes the eddy viscosity, k corresponds to turbulent kinetic energy and $\varepsilon$is the dissipation rate of the turbulent energy. The tensors $S_{ij}$and Ω_{ij} are the mean- rotation and mean-strain- rate tensors, respectively defined by:

$$S_{ij} = \frac{\partial U_i}{\partial x_j} + \frac{\partial U_j}{\partial x_i} \quad (4)$$

$$\Omega_{ij} = \frac{\partial U_i}{\partial x_j} - \frac{\partial U_j}{\partial x_i} \quad (5)$$

α_1, $\alpha_2$and $\alpha_3$are turbulence model parameters and they are determined based on relationships involving S and Ω, as outlined in equations 6-11.

$$\alpha_1 = -0.1325 f_M, \alpha_2 = 0.0675 f_M, \alpha_3 = -0.0675 f_M \quad (6)$$

$$f_M = (1 + m_{ds}S^2 + m_{d\Omega}\Omega^2)^{-1} \quad (7)$$

$$C_\mu = \frac{c_{\mu o}(1 + c_{ns}S^2 + c_{n\Omega}\Omega^2)}{D_\mu} \quad (8)$$

$$D_\mu = 1 + c_{ds}S^2 + c_{d\Omega}\Omega^2 + c_{ds\Omega}S\Omega + c_{ds1}S^4 + c_{d\Omega 1}\Omega^4 + c_{ds\Omega 1}S^2\Omega^2 \quad (9)$$

$$S = \frac{k}{\varepsilon}\sqrt{\frac{1}{2}S_{ij}S_{ij}} \quad (10)$$

$$\Omega = \frac{k}{\varepsilon}\sqrt{\frac{1}{2}\Omega_{ij}\Omega_{ij}} \quad (11)$$

The constant values for the above equations are provided in the software manual.

2.3. Soft Computing method

Artificial Neural Networks (ANNs), with their exceptional capability to discern patterns from complex and ambiguous data, can be utilized to uncover intricate methods that are challenging for humans and other computer techniques to comprehend. A trained neural network can be viewed as an expert in the information provided for analysis. The applications of this method in hydraulic engineering encompass predicting river floods, forecasting water quality parameters, and estimating the length of hydraulic jumps and friction coefficients in open smooth channels. The data in artificial neural networks is typically categorized into two groups: Training data, which is used to educate the network (comprising approximately 70 to 80 percent of the data), and Testing data, which serves as the primary benchmark for evaluating the proximity of predicted values to actual data (encompassing about 20 to 30 percent of the data). The steps involved in simulating artificial neural networks are as follows:

1. Collecting a sufficient set of inputs and outputs of the desired model (wherein data is generated by a numerical model, laboratory model, or real system measurements);
2. Selecting a suitable number of input-output sets as the training set, with the remainder designated as the test set. The artificial neural network model is then trained using the training set, involving the calculation of the model's parameters, i.e., weights and biases;
3. Entering the inputs of the training set into the designed artificial neural network with the parameters obtained from the previous step, and recording the calculated outputs;
4. Comparing the calculated outputs from the previous step with the real outputs, and recording the difference as the model's error;
5. Determining the calculated error for different ratios of training and test values;
6. Selecting an appropriate number of training sets by comparing the obtained values, and recording the final network parameters based on these values;
7. Continuing the algorithm by adjusting the network architecture until achieving a network with the lowest error.

During the network training process, the mean square error (MSE) between computed and observed values (as depicted in equation 12) serves as the fitness function, guiding the network training to minimize this error. In this equation, the results obtained from the artificial neural network (ANN) are denoted as "*Numerical*," while the laboratory results are represented as "*Observed*." Ultimately, a low MSE signifies high accuracy of this method.

$$MSE = \frac{\sum_{i=1}^{n}(Observed_i - Numerical_i)^2}{n} \tag{12}$$

In the above relation, n represents the number of data. The structure of artificial neural networks is presented in Figure 2, which may be single-layer or multi-layer.

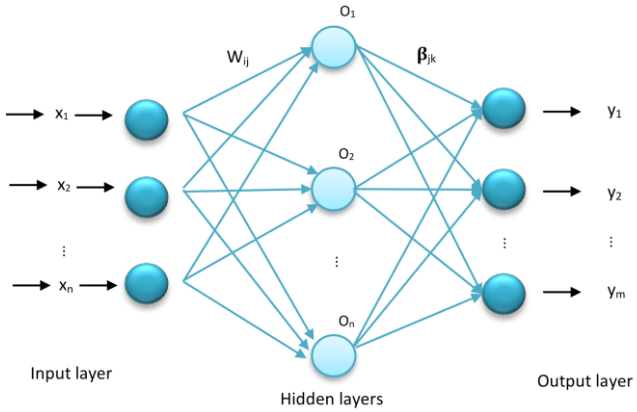


Figure 2. Structure of the MLP-ANN method.

3. Model Development

3.1. Numerical modeling in iRIC (NaysCUBE) software

A three-dimensional model was created to simulate a 11-meter-long and 1-meter-wide channel with a perpendicular groyne extending from the right channel wall into the main stream, measuring 15 cm in length and 1 cm in thickness. The groyne was treated as an obstruction. The domain was discretized using cartesian mesh. The mesh independency test, conducted using the grid convergence index (GCI) method suggested that the optimum number of grids are (450 × 50 × 15) in the x, y, and z directions, respectively [36].

A Manning coefficient of 0.01 was uniformly applied to the channel bed and side walls. At the western boundary of the computational domain (the inlet boundary), a constant discharge Q=60 $l.s^{-1}$ is imposed. The downstream boundary of the domain is defined as a constant water depth of 125 mm, which maintains the inlet water depth at 143 mm.

The model utilized the upwind numerical discretization method and employed the non-linear k-ε two-equation model for turbulence modeling. The depicted model can be seen in Figure 3, with points P_1 and P_2 serving as monitor points for overseeing the convergence of the numerical simulation.

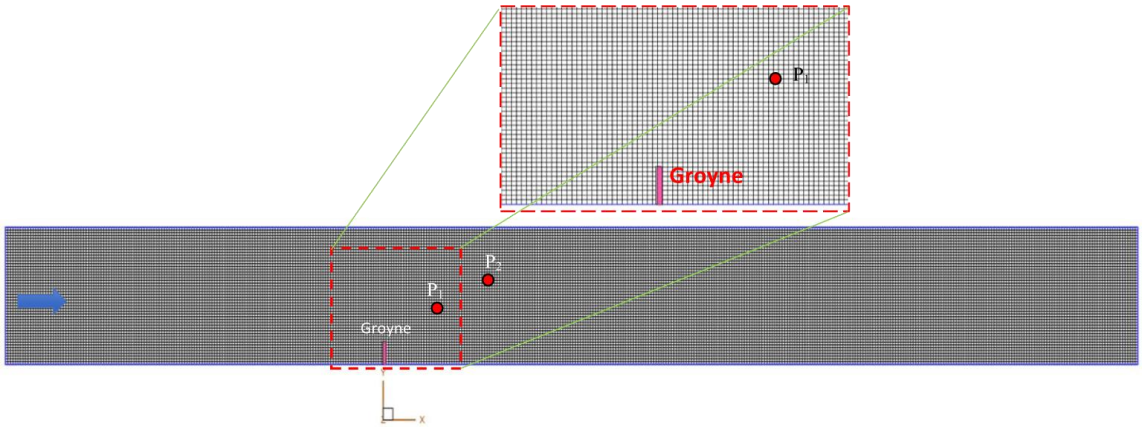


Figure 3. Computational domain in the CFD model (iRIC NaysCUBE model). Points P1 and P2 are monitor points.

3.1.1 Convergence control of numerical solution

The numerical model underwent analysis using a time step of 0.008 seconds over a duration of approximately 40 seconds. Figure 4 illustrates the temporal changes in velocity magnitude at two monitoring points, P1 and P2, situated near the channel bed and downstream of the groyne head. As shown in the figure, the solution has successfully reached complete convergence, with the velocity magnitude and other parameters stabilizing at constant values. The monitoring point locations are highlighted in Figure 3, with Point 1 positioned at X/L=1 and Y/L=2, and Point 2 at X/L=3 and Y/L=3.

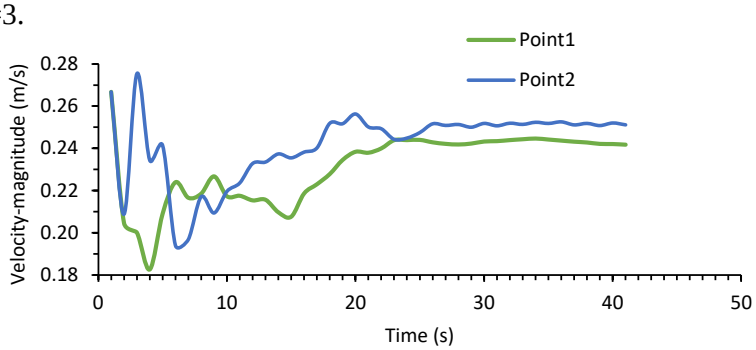


Figure 4. Numerical solution convergence for velocity-magnitude in points P1 and P2.

3.2. ANN modeling in MATLAB software

An artificial neural network was developed and trained using measured data within the MATLAB 2018b software. Following this, a testing phase was carried out using specific test numbers. The data division for testing and training was executed in the MATLAB code at a ratio of 20% for testing and 80% for training, with a random allocation process.

The input parameters in this setup included the Froude number (Fr=0.35), groyne length (L=120, 150, and 200mm), and spatial coordinates (X, Y, Z). The artificial neural network method considered the longitudinal, transverse, vertical components, and velocity magnitude (u, v, w, vel-mag) as the outputs. All input and output parameters were normalized by the groyne width (B) and input bulk velocity (Uin). Subsequently, the input parameters were dimensionless, represented as (X*=X/B, Y*=Y/B, Z*=Z/B, Fr, L/B), while the output parameters were normalized as (u*=u/Uin, v*=v/Uin, w*=w/Uin, vel-mag*=vel-mag/Uin).

For simulating the significant flow characteristics, the Multilayer Perceptron Method (MLP) was employed, featuring 24 hidden layers and 30 neurons in each layer.

4. Validation of the ANN and CFD Models

Figures 5 and 6 illustrate the comparison of the cross-sectional profiles of the three velocity components (u,v and w) and the velocity magnitude (vel-mag) in the planes close to the bed (Z=4mm) and close to the water surface (Z=81mm). A thorough examination of these figures distinctly shows the strong predictive accuracy of the Artificial Neural Network (ANN) approach for the velocity components on both planes.

The analysis of the longitudinal velocity component profile reveals a noticeable discrepancy between the simulated data from the Computational Fluid Dynamics (CFD) method and the actual measurements, particularly evident along the shear layer in both profiles compared to other regions. Specifically, the behavior of the Artificial Neural Network (ANN) method and the measured data shows fluctuations along the shear layer and at the flow separation boundary, in contrast to the consistent velocity increase from the channel's right wall towards the flow center observed in the CFD method velocity profiles.

The examination of the transverse velocity component in both profiles indicates a rise in this component near the groyne head. Assessing the velocity increase in this area is crucial for understanding local scour and groyne stability. Both forecasting approaches provide reasonably accurate results with lower values, but the precision of the Artificial Neural Network (ANN) method exceeds that of the Computational Fluid Dynamics (CFD) method. In figure 5-D, the velocity magnitude values obtained from simulations using both the ANN and CFD methods are compared with actual data near the bed. It is clear that the CFD method, which has limitations in predicting the longitudinal and transverse velocity components, also exhibits a diminished capability in this aspect compared to the ANN method.

4.1. Performance evaluation statistics

The assessment of the accuracy of the Artificial Neural Network (ANN) and Computational Fluid Dynamics (CFD) methods in predicting the flow field around a single straight groyne has been conducted utilizing statistical indices comprising five parameters: root mean squared error (RMSE), mean absolute error (MAE), absolute deviation percent (δ), standard error prediction percent (SEP), and correlation coefficient (R). The equations for these parameters are provided below:

$$RMSE = \sqrt{\frac{\sum_{i=1}^{N}(e_i - o_i)^2}{N}} \tag{13}$$

$$R = \frac{\sum_{i=1}^{n}(o_i - \bar{o})(e_i - \bar{e})}{\sqrt{\sum_{i=1}^{n}(o_i - \bar{o})^2 \sum_{i=1}^{n}(e_i - \bar{e})^2}} \tag{14}$$

$$MAE = \frac{1}{N}\sum_{i=1}^{N}|e_i - o_i| \tag{15}$$

$$\delta\% = \frac{\sum_{i=1}^{n}|(e_i - o_i)|}{\sum_{i=1}^{n} e_i} \times 100 \tag{16}$$

$$SEP\% = \frac{100}{\bar{o}} \times RMSE \tag{17}$$

In this equation, "e_i" represents the predicted data, "o_i" represents the measured data, $\bar{e}$ is the average of the predicted data, "$\bar{o}$" is the average of the measured data, and "N" is the total number of data points.

The lower values of the RMSE, MAE, δ, and SEP parameters, along with the higher values of the R parameter, indicate superior model performance. RMSE provides the standard deviation of the residuals, while MAE calculates the mean absolute residuals. These parameters offer the advantage of producing error values in the same unit as the model output, providing a reliable representation of the model's performance. Additionally, the δ and SEP methods yield dimensionless error values that are suitable for comparing cases with different scales. The R parameter indicates the linear correlation coefficient between two parameters, approaching 1 for accurate prediction and 0 for poor performance.

The quantitative assessment results of the u, v, w, and velocity-magnitude components by both methods are displayed in Table 2. Based on the data presented, the ANN method, characterized by lower RMSE values, exhibits superior predictive performance compared to the CFD method for parameters u, v, and velocity magnitude.

Table 2: Quantitative Results of Component Prediction u ،v ،w & vel-mag

Prediction Parameters	Prediction method	RMSE	MAE	δ%	SEP%	R-square
u	CFD	0.0999	0.0774	21.0200	27.1407	0.8332
	ANN	0.0664	0.0398	10.8208	18.0445	0.9152
v	CFD	0.0430	0.0337	46.0656	58.7075	0.8726
	ANN	0.0269	0.0189	25.7683	36.6755	0.9150
w	CFD	0.0152	0.0104	429.1606	630.7778	0.5985
	ANN	0.0194	0.0076	316.0246	804.3308	0.2474
vel-mag	CFD	0.0987	0.0746	18.7322	24.7845	0.8051
	ANN	0.0536	0.0390	9.7786	13.4531	0.9315

Figure 7 displays scatter plots of the parameters u, v, w, and vel-mag obtained from modeling using the ANN and CFD methods. In this representation, the measured data is depicted on the horizontal axis, while the predicted values by both methods are shown on the vertical axis. The plots reveal that the ANN method showcases a more uniformly distributed pattern of the mentioned parameters around the y=x line, indicating a heightened level of accuracy associated with this method.

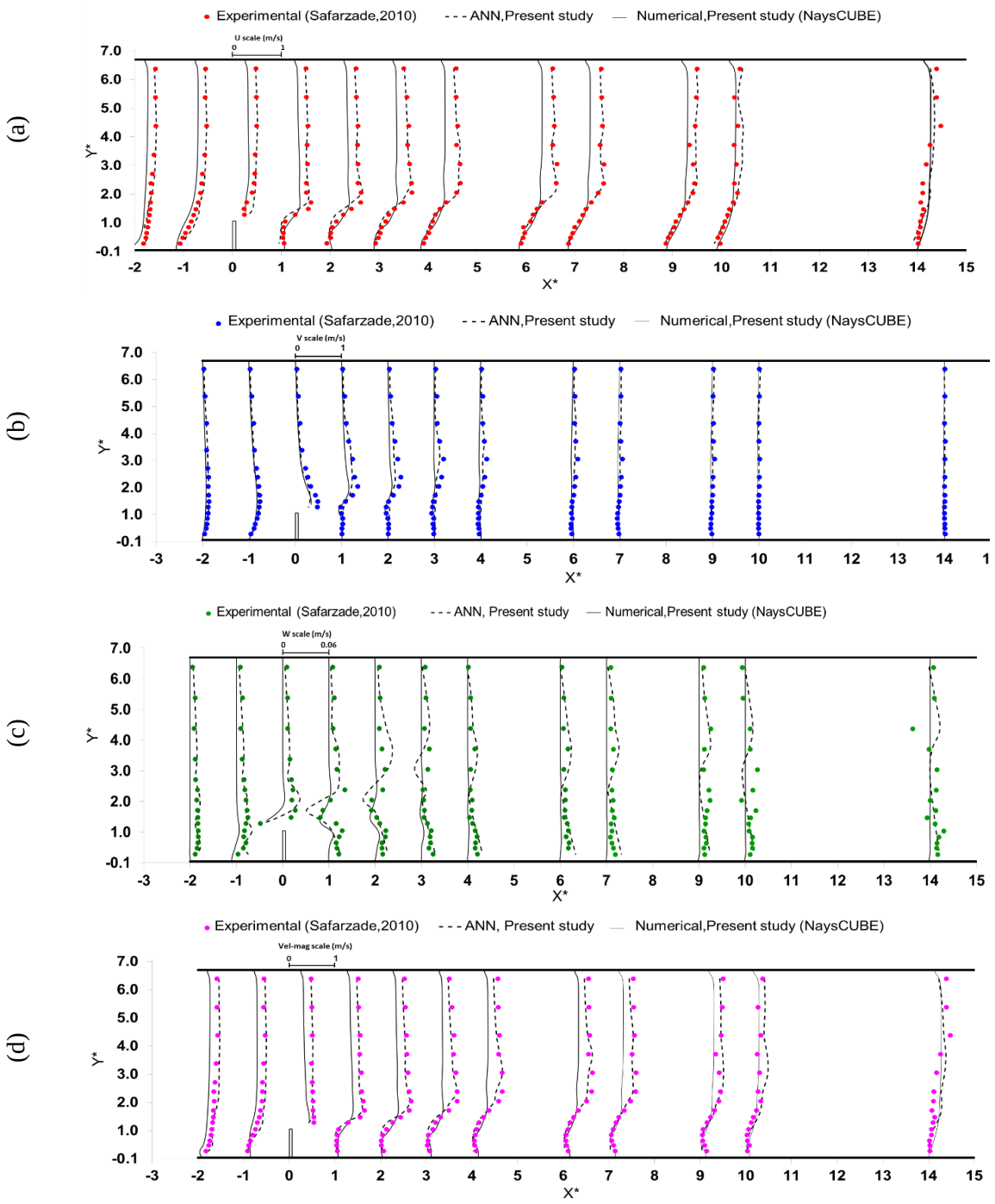


Figure 5. Comparative analysis of the experimental data, CFD modelling results, and ANN predictions in near-bed layer for different velocity components: (a) longitudinal velocity, (b) transverse velocity, (c) vertical velocity and (d) velocity magnitude.

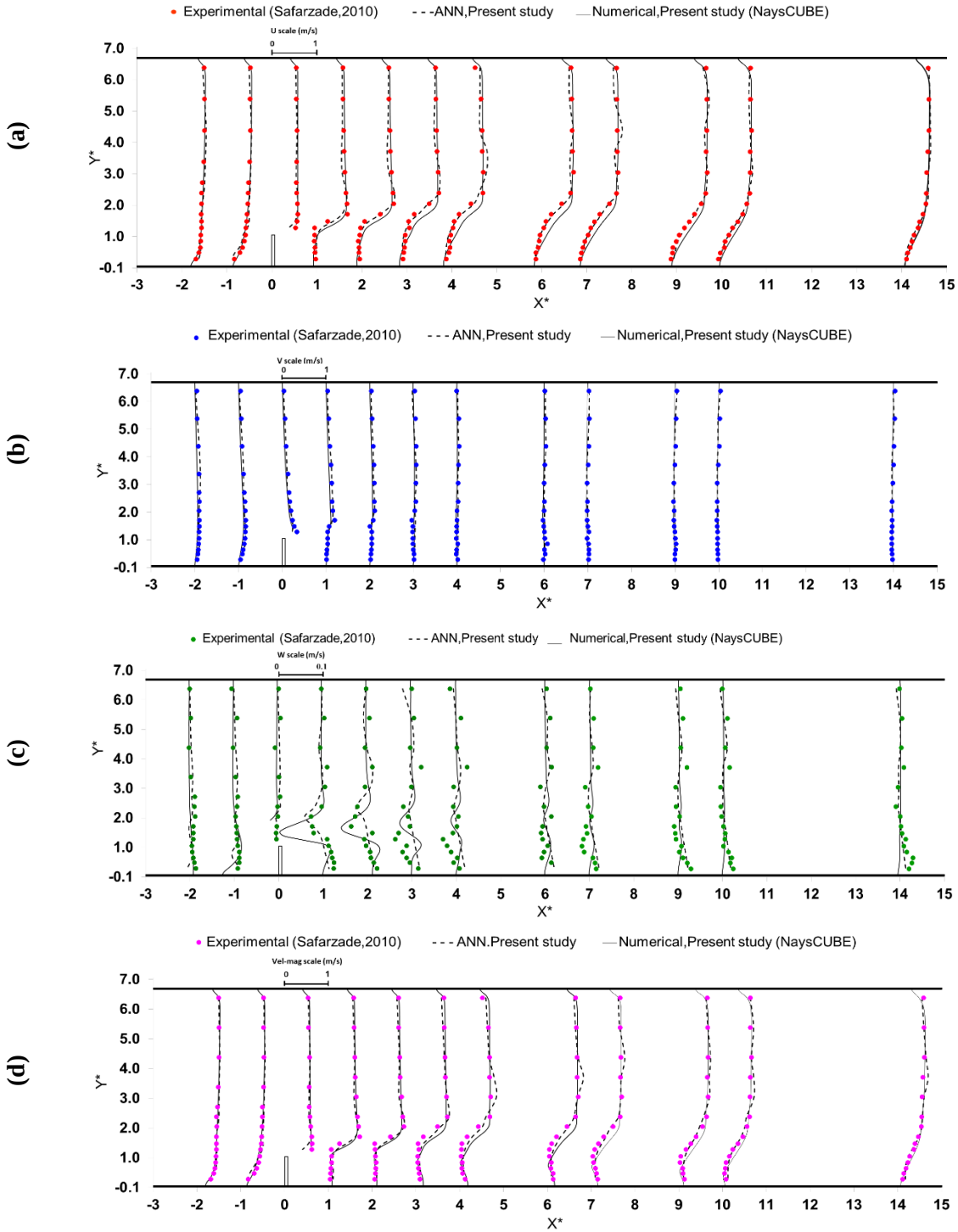


Figure 6. Comparative analysis of the experimental data, CFD modelling results, and ANN predictions in near-water surface layer for different velocity components: (a) longitudinal velocity, (b) transverse velocity, (c) vertical velocity and (d) velocity magnitude.

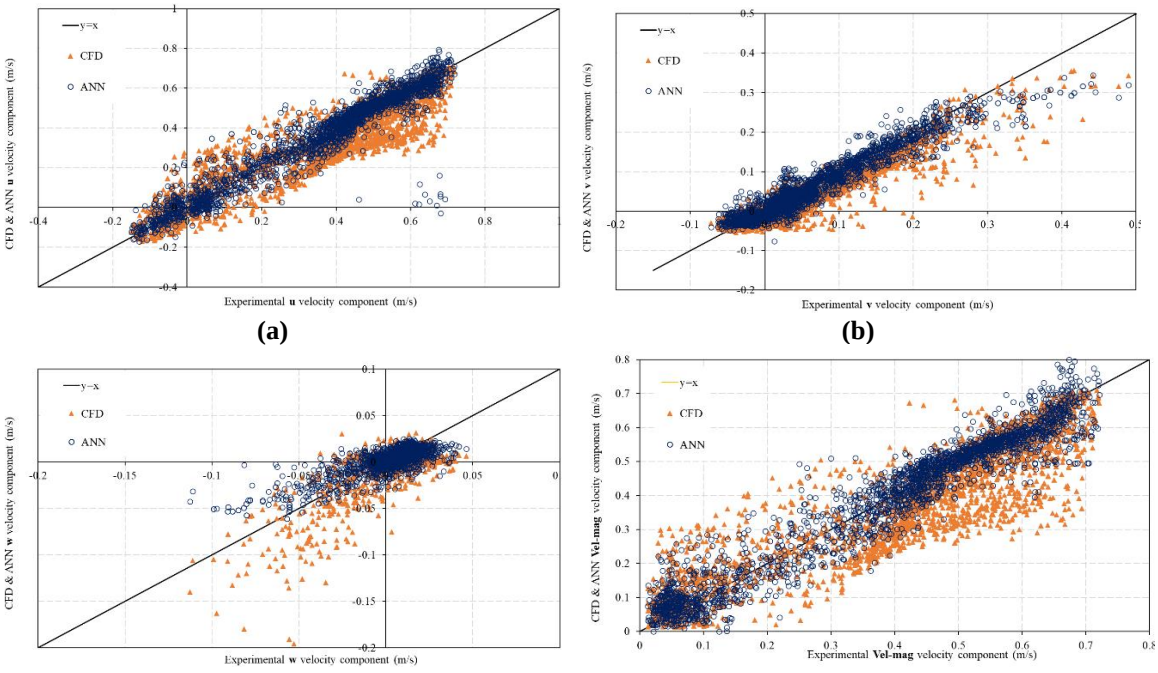


Figure 7 Comparison between the CFD and ANN study results with measured data in velocity scatter plots for different components: (a) u, (b) v, (c) w, and (d) velocity magnitude (vel-mag).

5. 2D and 3D flow features predicted by ANN and CFD methods

Figure 8 demonstrates the flow structure downstream of a single groyne, highlighting a discernible separation zone within the flow domain. While both the Artificial Neural Network (ANN) and Computational Fluid Dynamics (CFD) methodologies have offered predictions for the overall flow structure, the 3D flow pattern within the separation area, as anticipated by the ANN, closely resembles the actual experimental flow field. The streamlines depicted for the experimental flow and ANN indicate a downstream migration of the core circulation zone from the near-bed plane to the upper planes, whereas the vortex region centroids in the CFD simulation are approximately oriented vertically.

Figure 9 displays the 2D velocity vectors near the water surface. In both methods, towards the upper region of the field and distanced from the groyne structure, the vectors are notably parallel and aligned along the channel's sidewalls. As they approach the groyne, they gradually diverge and tilt towards the channel's central section. The ANN method accurately predicts the behavior of these velocity vectors, whereas the CFD method shows more deviation in the upper part of the groyne. In Figure 9a, it is evident that the length of the circulation zone is approximately 12 times the length of the groyne in the ANN prediction, while in the CFD prediction, this length reduces to around 10.2 times the groyne length, indicating a discrepancy between the measured data and CFD prediction.

In the CFD method, the center of the circulation zone is positioned closer to the groyne body than observed in the experimental results. On the other hand, the ANN method accurately forecasts the center's location. While both methods successfully predict the main flow phenomena within the field, the ANN method outperforms in modeling the precise location of these phenomena with higher accuracy.

To explore the 3D flow structure, secondary flows at different sections both upstream and downstream of the groyne are illustrated in Figure 10 (on the right side). When examining the figures in the upstream region of the groyne, primary flows exhibit a unidirectional transverse flow from the right wall of the channel to the opposite wall, a prominent pattern observed in both of the CFD and ANN methods. As the flow approaches the groyne section, the initial unidirectional transverse flows transition into rotational flows within the section, forming a clockwise secondary cell (A) in the separation zone at cross-section X/L=2. This flow pattern is clearly visible in Figure 10-b (on the right side) using the CFD method, while the ANN method also predicts this phenomenon, albeit with lower values. This flow progresses along the channel towards the water surface and eventually dissipates at cross-section X/L=14. In the CFD method, the rotational flow (A) extends to cross-section X/L=8, whereas the ANN method extends this flow up to cross-section X/L=14. Additionally, a significant upward flow emerges along the right channel wall, supported by both measured and ANN data. Remarkably, this flow characteristic was not predicted by the CFD method.

An additional rotational flow (B), characterized by a counterclockwise rotation distinct from the previously mentioned rotational flow, is observed in the relevant figure of the experimental results. As depicted in Figure 10, this type of flow has been accurately predicted by the ANN method, in contrast to the CFD method. The centers of these two rotational zones are spatially separated along the length of the field, a distinguishing feature that is clearly observable in the ANN method's predictions.

At cross-sections X/L=14 and 17, corner vortices emerge at the junction of the right channel wall and the bed, forming a rotational flow labeled as C in the experimental results. Surprisingly, this phenomenon was not anticipated by either the CFD or ANN method.

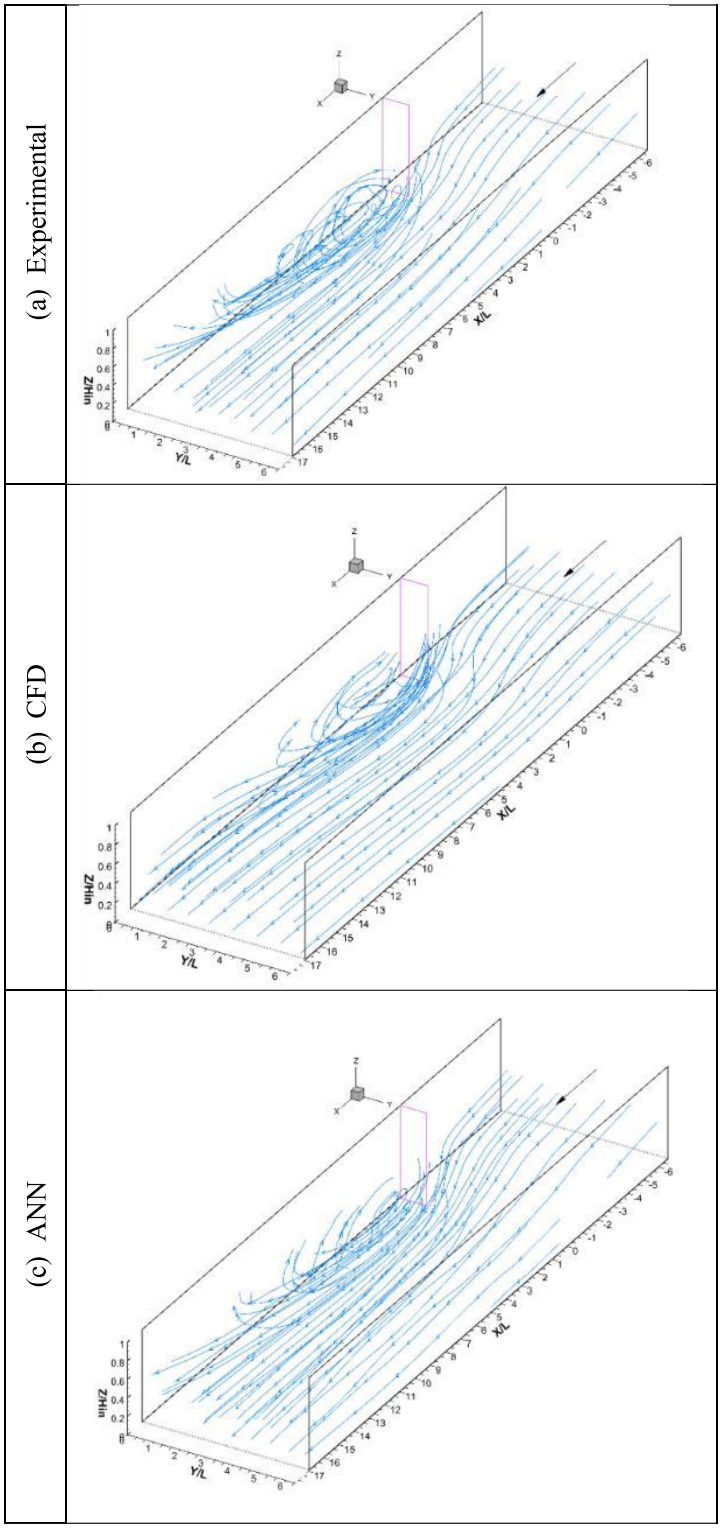


Figure 8. Visualization of 3D streamlines around a straight groyne showing: (a) Experimental results, (b) CFD simulation, and (c) ANN prediction.

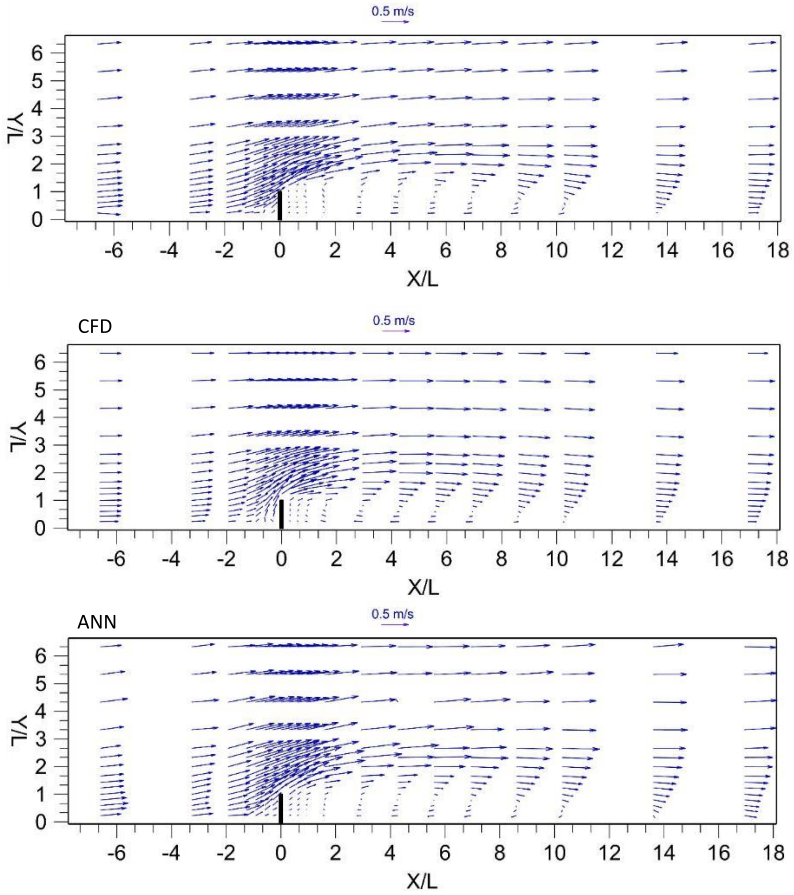


Figure 9. Representation of 2D Velocity Vectors in the plane near the water surface illustrating: (a) Experimental results, (b) CFD simulation, and (c) ANN prediction.

For a more accurate assessment of the flow field predictions made by the ANN and CFD methods, contour plots displaying the velocity magnitude distribution within different cross-sections in Figure 10 (left side) are included to facilitate an in-depth analysis.

A comparison of velocity contours between the measured data and results from both methods at cross-sections X/L=-2 and -4 indicates a consistent flow pattern with an approximate velocity of 0.42 m/s. Both the ANN and CFD methods demonstrate similarities to the experimental flow. Experimental results display an increase in velocity in the groyne section and the main flow channel, reaching around 0.55 m/s, a trend accurately captured by both methods. However, the CFD method shows slightly lower values. Beyond the groyne section, two distinct areas of intensified velocity emerge. One area corresponds to the flow core's velocity increase due to flow constriction, leading to a general velocity amplification, while the other area relates to localized velocity intensification downstream of the groyne and near the shear layer, displaying higher velocities than the previous high-velocity region. The CFD method fails to predict these two areas, although it anticipates the high-velocity region. Conversely, the ANN method does not differentiate between these two zones.

As we move downstream, the impact of the groyne gradually diminishes along the shear layer, and the heightened-velocity region gradually fades away. In the experimental results, beyond X/L=11, this region completely vanishes, giving way to a gradual velocity increase

towards the channel center up to the final section. This flow behavior has been precisely forecasted by the ANN method. The CFD method similarly illustrates this flow trend, albeit with slightly lower values.

Figure 11 displays the distribution of the vertical velocity component and secondary flow structures in cross-sections perpendicular to the horseshoe vortex's path. In Figure 11-a (experimental data), within the upstream area of the groyne head, the contours of the vertical component and velocity vectors reveal a juxtaposition of upward (positive flow) and downward vertical flows, indicating the presence of the horseshoe vortex with its peak intensity in this region. The clockwise and counterclockwise rotational zones (secondary flows) mentioned earlier are clearly visible in these sections, with their size expanding but their strength diminishing downstream, indicating the weakening of the horseshoe vortex along this trajectory. The delineated lines along the shear layer formation highlight the appearance of the horseshoe vortex in between. Both the CFD and ANN methods capture the downward vertical flow in the upstream groyne region, with varying magnitudes, the ANN method demonstrating higher accuracy. While both methods predict positive vertical component values, they do so at lower levels. The secondary flows around the groyne head are evident in both methods, but unlike the experimental findings, they wane along the trajectory.

In Figure 12 depicting streamlines at the XZ plane upstream of a single groyne (Y/L=0.3), a color contour plot of the w-velocity is included. The streamlines in the experimental figure exhibit characteristics of the near-bed Horseshoe Vortex (HSV) in the proximity of the upstream face of the groyne. The separation of the bed boundary layer and the rolling up of the incoming flow due to the reversed flow at the groyne's base are prominently highlighted. The 2D HSV forecasted by the CFD method aligns reasonably well with the observed HSV structure, but disparities exist in the location of formation and the magnitude of the HSV compared to the laboratory data. The ANN method also predicts this phenomenon with a lesser degree of approximation.

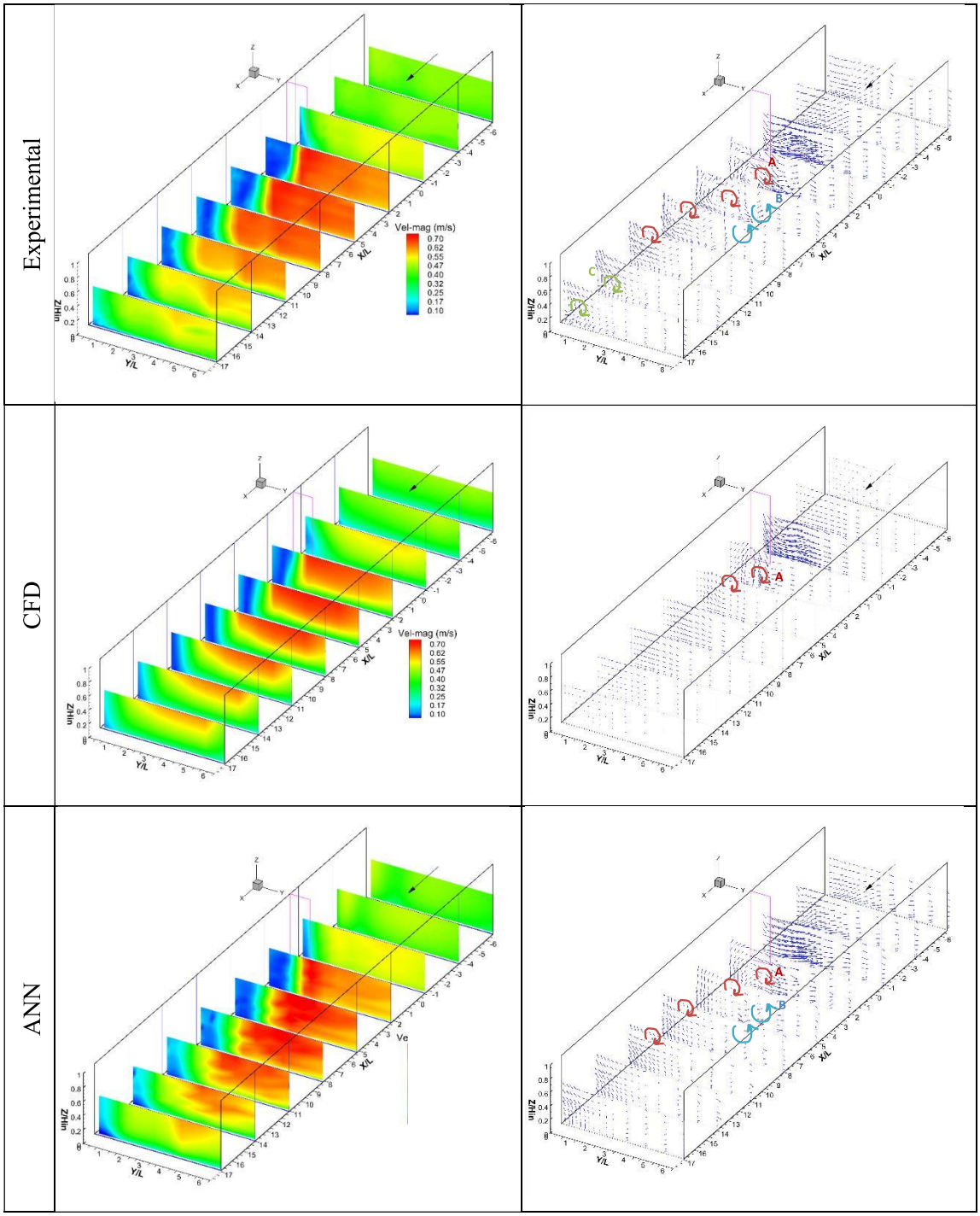


Figure 10. Comparison of the velocity magnitude and secondary flows in various cross sections around a straight groyne between experimental results, CFD simulation and ANN prediction.

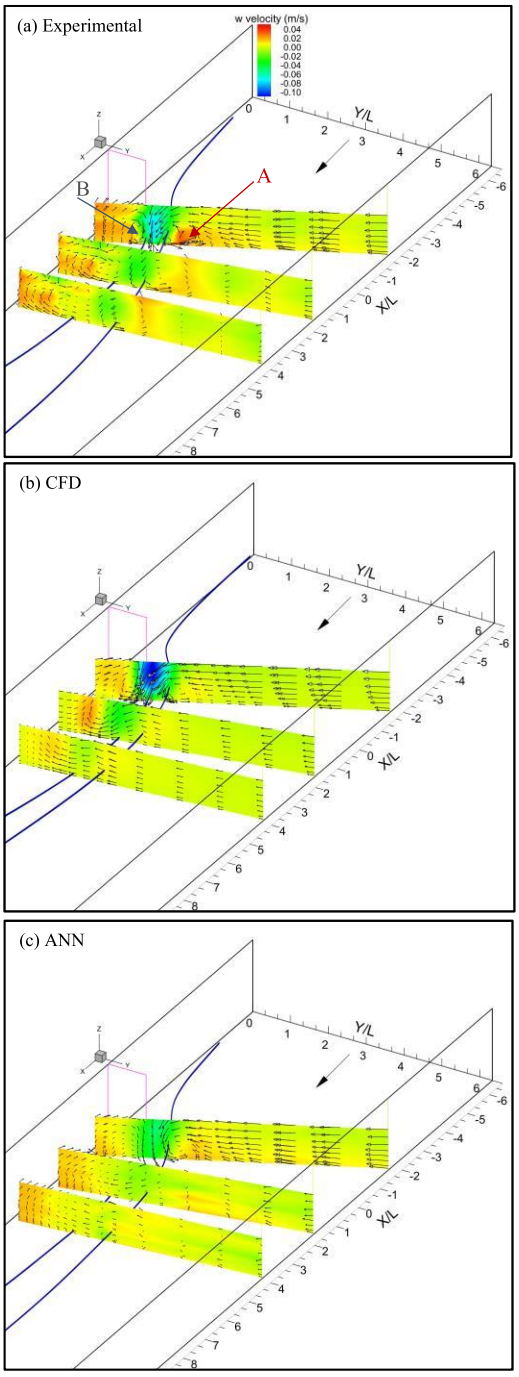


Figure 11. Comparison of the structure of the secondary flows in sections perpendicular to the horseshoe vortex path using: (a) experimental data, (b) CFD simulation, and (c) ANN prediction.

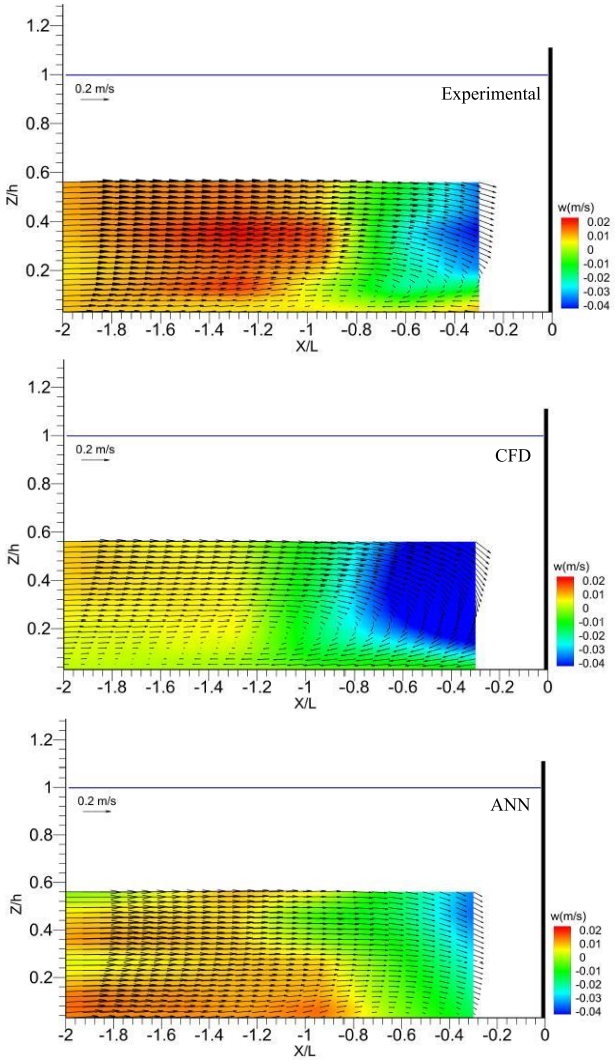


Figure 12. Comparison of the velocity vectors at Y/L=0.3 plane, upstream of the tested groyne between Experimental results, CFD simulation & ANN prediction (the contours depict the distribution of the w velocity component).

6. Conclusion

In this investigation, the 3D flow field around a single straight groyne was analyzed using Computational Fluid Dynamics (CFD) and Artificial Neural Network (ANN) methods. The ANN model incorporated dimensionless parameters X*, Y*, Z*, Froude number (Fr), and groyne length L* as inputs. The accuracy of the ANN model in predicting velocity component profiles and velocity magnitudes on near-bed and free surface planes was assessed against experimental data (Safarzadeh, 2010). The CFD analyses were conducted with the iRIC model using the nonlinear k-ε turbulence model to close the Reynolds-Averaged Navier-Stokes (RANS) equations.

The quantitative evaluation findings indicated that the ANN method excelled over the CFD method in forecasting the longitudinal (u), transverse (v), and velocity magnitude parameters,

demonstrating lower Root Mean Square Error (RMSE), Mean Absolute Error (MAE), and higher R-values. Conversely, the CFD method displayed notable discrepancies from the experimental data, especially in the near-bed zones.

The examination of transverse velocity profiles indicated that the ANN method successfully represented the changes in velocity components and magnitude across the shear layer and at the flow separation boundary. In contrast, the CFD method exhibited a consistent rise from the channel wall towards the main flow zone, deviating from the expected behavior observed in the ANN model.

Upon further analysis of streamlines and velocity vectors, it was observed that the CFD method underestimated the length of the recirculation zone, in contrast to the precise prediction made by the ANN method.

The analysis of 2D and 3D contour and velocity vector plots highlighted the ANN method's capability to reasonably predict important flow characteristics such as the horseshoe vortex around the groyne head in the lower layers, secondary flows in sections downstream of the groyne, and velocity amplification at the outer boundary of the recirculation zone. Conversely, the CFD method exhibited deficiencies in accurately representing these phenomena in certain instances.

In summary, the findings suggest that the ANN method offers a more reliable and precise forecast of the intricate 3D flow field around a single straight groyne when compared to the CFD method. This underscores the potential of data-driven approaches such as ANN in tackling complex fluid dynamics issues that present challenges for conventional numerical simulations. The outcomes of this research have the potential to enhance the comprehension and simulation of flow around river structures, with implications for river engineering and hydraulic design practices.

References

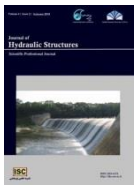
1. Ahmad, M. (1953). Experiments on design and behavior of spur-dikes. Proceeding of Minnesota International Hydraulics Convention, International Association of Hydraulic Research, Madrid, Spain.
2. Koken, M., & Constantinescu, G. (2008a). An investigation of the flow and scour mechanisms around isolated spur dikes in a shallow open channel: 1. Conditions corresponding to the initiation of the erosion and deposition process. Water Resources Research, pp: 44 (8).
3. Koken, M., & Constantinescu, G. (2008b). An investigation of the flow and scour mechanisms around isolated spur dikes in a shallow open channel: 2. Conditions corresponding to the final stages of the erosion and deposition process. Water Resources Research, pp: 44 (8).
4. Koken, M., & Constantinescu, G.(2009). An investigation of the dynamics of coherent structures in a turbulent channel flow with a vertical sidewall obstruction. Physics Of Fluids, pp: 21(8).
5. Duan, J.G. (2009). Mean flow and turbulence around a laboratory spur dike. Journal of Hydraulic Engineering, pp: 135(10): 803-811.
6. Duan, J.G., He, L., Fu, X., & Wang, Q. (2009). Mean flow and turbulence around experimental spur dike. Advances in Water Resources, pp: 32(12): 1717-1725.
7. Koken, M. (2011). Comparison of coherent structures around isolated spur dikes at various angles. Journal of Hydraulic Reaserch, pp: 49(6):736-743.

8. Safarzadeh, A., Neyshabouri, S.A.A., & Zarrati, A.R. (2016). Experimental investigation on 3D turbulent flow around straight and T-Shaped groynes in a flat bed channel. Journal of Hydraulic Engineering, pp: 142(8).
9. Safarzadeh, A., & Brevis, W.(2016). Assessment of 3D-RANS models for the simulation of topographically forced shallow flows. Journal of Hydrology and Hydromechanics, pp: 64(1): 83-90.
10. Jeon, J., Lee, J. Y., & Kang, S. (2018). Experimental investigation of three-dimensional flow structure and turbulent flow mechanisms around a nonsubmerged spur dike with a low length-to-depth ratio. Water Resources Research, pp: 54(5): 3530-3556.
11. Kan, G., Yao, C., Li, Q., Li, Z., Yu, Z., Liu, Z., Ding, L., He, X., Liang, K. (2015). Improving event-based rainfall-runoff simulation using an ensemble artificial neural network based hybrid data-driven model. Stochastic Environmental Research and Risk Assessment, 29(5):1345–1370.
12. Wu, J., Long, J., Liu, M. (2015) Evolving RBF neural networks for rainfall prediction using hybrid particle swarm optimization and genetic algorithm. Neurocomputing, 148:136–142.
13. Chaowanawatee, K., & Heednacram, A. (2012). Implementation of cuckoo search in RBF neural network for flood forecasting. Proceeding of the fourth international conference on computational intelligence, communication systems and networks, pp: 22-26.
14. Xie, JC.,Wang, TP., Zhang, JL., Shen, Y. (2010) Amethod of flood forecasting of chaotic radial basis function neural network. Proceedings of 2nd International Society of Automation, Wuhan, China.
15. Li, S., Zhao, N., Shi, Z., & Tang, F. (2010, June). Application of artificial neural network on water quality evaluation of Fuyang River in Handan city. Proceedings of International Conference on Mechanic Automation and Control Engineering, pp: 1829-1832.
16. Najah, A., El-Shafie, A., Karim, OA., El-Shafie, AH. (2013) Application of artificial neural networks for water quality prediction. Neural Computing and Application, 22(1):187–201.
17. Shen, XQ., He, TD. (2012)Water quality evaluation based on RBF neural network with parameters optimized by PSO algorithm. Proceedings of Sarvajanik College of Engineering &Technology, Wuhan University, China.
18. Bateni, SM., Borghei, SM., Jeng, DS. (2007) Neural network and neurofuzzy assessments for scour depth around bridge piers. Engineering Applications of Artificial Intelligence, 20(3):401–414.
19. Begum, SA., Fujail, AKM., Barbhuiya, AK. (2011) Radial basis function to predict scour depth around bridge abutment. Proceedings of 2nd National Conference on Emerging Trends and Applications in Computer Science, pp: 1-7.
20. Zaji, A.H., & Bonakdari, H.(2015). Application of artificial neural network and genetic programming models for estimating the longitudinal velocity field in open channel junctions. Flow Measurement and Instrumentation, Elsevier, pp: 41:81-89.
21. Abbaspour, A., Farsadizadeh, D., Ghorbani, MA. (2013) Estimation of hydraulic jump on corrugated bed using artificial neural networks and genetic programming. Journal of water scienc and engineering, 6(2):189–198.
22. Houichi, L., Dechemi, N., Heddam, S., Achour, B. (2013) An evaluation of ANN methods for estimating the lengths of hydraulic jumps in U-shaped channel. Journal of Hydroinformatics, 15(1):147–154.
23. Naseri, M., Othman, F. (2012) Determination of the length of hydraulic jumps using artificial neural networks. Advances in Engineerig Software, 48:27–31.

24. Yang, H. & Chang, F. (2005). Modelling combined open channel flow by artificial neural network. Hydrological Processes, pp: 19(18): 3747 – 3762.
25. Gholami, A., Bonakdari, H., Zaji, A., & Akhtari, A. (2015). Simulation of open channel bend characteristics using computational fluid dynamics and artificial neural networks. Engineering Applications of Computational Fluid Mechanics, pp: 9 (1): 355-369.
26. Ebtehaj, I. & Bonakdari, H. (2013). Evaluation of sediment transport in sewer using artificial neural network. Engineering Applications of Computational Fluid Mechanics, pp: 7(3): 382-392.
27. Sun, S., Yan, H., & Kouyi G. (2014). Artificial neural network modelling in simulation of complex flow at open channel junctions based on large data sets. Environmental Modelling & Software, pp: 62:178-187.
28. Safarzadeh, A., Zaji, A.H., & Bonakdari, H.(2017). Comparative assessment of the hybrid genetic algorithm–artificial neural network and genetic programming methods for the prediction of longitudinal velocity field around a single straight groyne. Applied Soft Computing, Elsevier, pp: 60: 213-228.
29. Safarzadeh, A., Zaji, A.H., & Bonakdari, H.(2018). 3D flow simulation of straight groynes using hybrid DE-based artificial intelligence methods. Springer Nature, pp: 23(11): 3757-3777.
30. Karki, S., Nakagawa, H., Kawaike, K., Hashimoto, M., & Hasegawa, Y. (2020). Assessing the effect of groynes orientation on near-bank flow and morphology in a natural meander bend using 2D numerical simulation. Proceedings of River Flow conference, Netherlands.
31. Wu, T., & Qin, J. (2020). Influence of flow and sediment transport processes on sedimentation in groyne fields. Journal of Coastal Research, 95, 304-309.
32. Pourshahbaz, H., Abbasi, S., Pandey, M., Pu, J. H., Taghvaei, P., & Tofangdar, N. (2020). Morphology and hydrodynamics numerical simulation around groynes. ISH Journal of Hydraulic Engineering, 28(1), 53–61.
33. Pandey, M., Jamei, M., Karbasi, M., Ahmadianfar, I., & Chu, X. (2021). Prediction of maximum scour depth near spur dikes in uniform bed sediment using stacked generalization ensemble tree-based frameworks. Journal of Irrigation and Drainage Engineering, 147 (11).
34. Ding, C., Li, C., Song, L., & Chen, S. (2023). Numerical investigation on flow characteristics in a mildly meandering channel with a series of groynes. Sustainability, 15(5).
35. Xie, P., Li, C., Lv, S., Zhang, F., Jing, H., Li, X., & Liu, D. (2023). Numerical simulation of 3D flow structure and turbulence characteristics near permeable spur dike in channels with varying sinuosities. Sustainability, 15(22).
36. Roache, P. J. (1994). Perspective: a method for uniform reporting of grid refinement studies. Journal of fluids engineering, pp: 116(3): 405-413.

© 2024 by the authors. Licensee SCU, Ahvaz, Iran. This article is an open access article distributed under the terms and conditions of the Creative Commons Attribution 4.0 International (CC BY 4.0 license) (http://creativecommons.org/licenses/by/4.0/).

Journal of Hydraulic Structures
J. Hydraul. Struct., 2024; 10(4): 26-45
DOI: 10.22055/jhs.2024.46813.1297



OPEN ACCESS

Adsorption characteristics of NH_2-UiO-66 for the removal of hematite inorganic dye from industrial wastewater: Isotherm, thermodynamic, and kinetic study

Abbas Mohammadi[1,2]
Mehdi Sedighi[2]

Abstract

Metal-organic frameworks (MOFs) have emerged as a class of highly promising materials for wastewater dye removal due to their unique properties. However, the existing body of research has primarily concentrated on the removal of organic dyes. To address this gap and contribute to advancements in water treatment technologies, this study investigates the efficacy of a zirconium-terephthalate-based MOF for the adsorptive removal of hematite, an inorganic dye, from aqueous environments. This investigation explored the influence of key parameters, including initial dye concentration, pH, adsorbent dosage, and adsorption temperature, on the adsorption capacity of NH_2-UiO-66 for hematite. The findings revealed that elevated temperatures and initial dye concentrations promoted hematite adsorption onto NH_2-UiO-66. Furthermore, the analysis of experimental data demonstrated concordance with the theoretical predictions of both the linearized Freundlich and Langmuir isotherm models. The study of kinetic models reveals that the pseudo-first-order model can adequately describe experimentally obtained data. The adsorption thermodynamic parameter ΔG_0 was found to be approximately -3.70, -3.94, and -4.19 $kJ.mol^{-1}$ at 298, 313, and 328 K, respectively. Furthermore, the ΔH_0 and ΔS_0 parameters were 5.15 $kJ.mol^{-1}$ and 54.3 $J.mol^{-1}$, respectively, indicating an endothermic adsorption mechanism. Further investigation found that the regeneration effectiveness is greater than 92% even after three adsorption cycles.

Keywords: Inorganic dye, hematite, adsorption, isotherm, metal–organic framework.

Received: 10 May 2024; Accepted: 10 July 2024

[1] Safety & Protection Reaserch Center (S.P.R.C.), University of Qom, Qom, Iran, Email: Mohammadi.a@qom.ac.ir **(Corresponding author)**
[2] Department of Chemical Engineering, University of Qom, Qom, Iran.

CC BY

1. Introduction

There has been a notable rise in the utilization of dyes across a wide range of industries in recent years. These industries include paper, petroleum, plastics, printing, cosmetics, textiles, leather, food, paint, rubber, pharmaceuticals, and dyestuffs. Residual dyes within industrial effluent present a substantial threat to human health and the environment. This risk stems from the inherent toxicity and carcinogenic properties of these dyes [1,2]. Dyes exhibit high resistance to degradation by heat, light, and oxidizing agents [3]. The presence of these pigmented pollutants not only detracts from the visual quality of water resources but also serves as a significant inhibitor of light penetration, thereby detrimentally impacting the photosynthetic processes of aquatic organisms [4]. As a result, one of today's most serious concerns is the treatment of dye-containing wastewater. Various physicochemical and biological methods, including adsorption [5-7], flocculation [8-10], electrolysis [11-13], coagulation [8,14,15], catalytic oxidation [16-18], ultra-filtration [19.20], and biodegradation [21,22], are employed for the removal of dyes. In the domain of water treatment, physical methods are increasingly favored over chemical and biological techniques due to their inherent economic benefits, operational simplicity, and minimal production of residual contaminants in the treated water [23,24]. Within the diverse spectrum of techniques employed for the remediation of wastewater harboring natural and synthetic dyes, adsorption has established itself as a frontrunner. This preeminence stems from its confluence of advantageous characteristics, including economic feasibility (manifested by low cost), remarkable efficacy in dye removal, broad applicability across a variety of dye types, minimal environmental footprint, and straightforward operational requirements [23,25].

Activated carbon, mesoporous silicates, zeolites, carbon nanotubes, diatomaceous earth, and resins are among the common adsorbents discussed in the literature. An effective adsorbent possesses several distinguishing features, including a high porosity with a substantial surface area, simplified preparation process, affordability, sturdy mechanical and thermal properties, impressive adsorption capabilities, and the capacity to regenerate over a broad spectrum of contaminants. Metal-organic frameworks (MOFs) emerge as a captivating class of novel materials demonstrating exceptional potential for dye removal applications. This efficacy can be ascribed to their remarkable stability and the vastness of their specific surface area [1]. By virtue of their facile synthesis, extensive surface areas, significant porosities, and tunable pore dimensions, these materials exhibit remarkable potential for diverse applications, encompassing adsorption, catalysis, detection, storage, and healthcare [26]. Much research has been conducted and published on employing MOFs for the removal of metals, anions, dyes, and various organics from polluted water [27,28]. Because of their outstanding water stability and excellent adsorption capabilities, zirconium (IV)-based MOFs have been reported to have adsorptive properties in these studies [23]. Since UiO-66, NH_2-UiO-66, N_2-UiO-66, and a number of other zirconium (Zr)-based MOF fulfill a wide range of the specific criteria, they have emerged as promising candidates for the treatment of water contaminated with dyes [1,3,24,29]. Chen et al. employed UiO-66 and NH_2-UiO-66 frameworks to assess their efficacy in adsorbing a range of hydrophilic dyes possessing both anionic and cationic functionalities [24]. Li et al. [30] explored the application of microwave-synthesized UiO-66 for the adsorptive removal of dyes. Their findings revealed a higher affinity of NH_2-UiO66 (aminated UiO-66) for cationic dyes (Rhodamine B, Neutral Red, and Methylene Blue) compared to anionic dyes (Acid Chrome Blue K and Methyl Orange). This suggests a potential influence of electrostatic interactions on the adsorption process. He et al. [3] reported the elimination of Rhodamine B by adsorption on UiO-66. They also looked into the regeneration of used adsorbents and demonstrated that the material may be reused for six sorption/desorption cycles. A later investigation focused on UiO-66's ability to adsorb, or bind, Acid Orange 7 (AO7)

dye [31]. Embaby et al. [23] utilized an adsorption technique to assess the effectiveness of UiO-66 in removing a variety of organic dyes. Their study encompassed a broad spectrum of dyes, including both anionic (Methyl Orange, Eosin, and Alizarin Red S) and cationic varieties (Fuchsin Basic, Neutral Red, Safranine T, and Methylene Blue). Tambat et al. [32] investigated the effects of solution pH and initial Safranin dye concentration on the NH_2-UiO-66's capacity for adsorbing the dye. In their recent work, the authors synthesized UiO-66 and N_2-UiO-66 MOFs and assessed their potential for the adsorptive capture of a range of organic pollutants, including basic blue, red 2B, methyl orange, and acid green dyes [29].

Mousavi et al. [33] elucidated the adsorption behavior of UiO-66 materials they synthesized. Cationic dye methylene blue (MB) and anionic dye methyl red (MR) were chosen as model organics. In their study, Fang et al. explored the efficacy of Zr-based MOFs in removing methylene blue (MB), a cationic dye. They employed both solvothermal and microwave irradiation techniques for the synthesis of these MOFs [1]. Qui et al. [34] explored the application of acid-assisted synthesis for the fabrication of UiO-66, a metal-organic framework (MOF), exhibiting a marked selectivity towards the adsorption of anionic dyes (e.g., methyl orange) compared to cationic dyes (e.g., methylene blue).

Most research studies have focused on UiO-66 or NH_2-UiO-66 combined with organic dyes. However, NH_2-UiO-66's application in removing inorganic dyes through adsorption has been relatively overlooked. This study introduces the solvothermal synthesis of NH_2-UiO-66 and evaluates its efficacy in removing hematite (α-Fe_2O_3) dye. Hematite, owing to its abundant natural availability, serves as a widely utilized red mineral dye and holds significant economic importance as an inorganic red pigment. An extensive evaluation of NH_2-UiO-66's adsorption capacity for dye removal was undertaken. This comprehensive investigation explored the influence of initial dye concentration, adsorption temperature, adsorbent dosage, and solution pH. To elucidate the underlying adsorption mechanism, various isotherm models (Freundlich, Langmuir, Temkin, and Dubinin-Radushkevich) were employed in both linear and non-linear forms, achieving optimal data fitting. Additionally, kinetic models like pseudo-first and pseudo-second order, power law (Elovich), and Fick's law (intraparticle diffusion) were employed to gain insights into the adsorption rate process. Moreover, the thermodynamic parameters related to the adsorption mechanism were examined.

2. Experimental procedure

2.1. Materials

The Sigma-Aldrich company supplied 99.99% pure zirconium tetrachloride compounds and 99% pure 2-amino terephthalic acid. Merck company provided dimethyl-formamide (DMF), sodium hydroxide with a purity of more than 97%, and HCl with a purity of 37%. The absolute C_2H_5OH was also prepared by Kimia Alkol Company. Ishtar Company provided hematite powder.

2.2. Methods

Metal-organic framework (MOF) syntheses were carried out in either 25 mL or 100 mL vials. A commercial ultrasonic bath (Yaxun YX3080) was employed for ultrasonic irradiation during the synthesis process. Following synthesis, the as-prepared MOFs were dried in a vacuum oven (Memmert VO-200) to remove any residual solvent. The weight of each material was precisely determined using an analytical balance capable of measuring to 0.1 mg. The reaction mixtures were centrifuged using a general-purpose centrifuge (model 37852). Powder X-ray diffraction (PXRD) analysis was conducted on a commercially available diffractometer (ARL Thermo-Xray) operated at standard operating conditions (20 kV and 20 mA). FTIR spectra were collected in

wavenumbers (cm^{-1}) using KBr pellets on a commercially available spectrometer (Thermo/Nicolet Magna-IR 550). Brunauer-Emmett-Teller (BET) surface area analysis was performed with a modern instrument (NOVA E-series). Additionally, UV/Vis absorbance measurements were obtained using a commercial UV/Vis spectrometer (GBC UV/VIS 911A). Adsorption experiments were conducted within a 200 mL cylindrical glass vessel equipped with a water jacket to ensure a constant temperature for the adsorption process. The solution was continuously agitated using a JOANLAB LS-40PRO shaker. To eliminate any residual particulates, the dye solution was subsequently filtered through Durapore 0.22 µm filters. Precise temperature control was achieved by employing a Lauda RE-104 circulator. A Radiometer PHM250 ion analyzer was utilized to accurately measure the solution's pH through a potentiometric technique.

2.3. Adsorbent synthesis procedure

The $ZrCl_4$-based adsorbent was synthesized via a solvothermal method [1, 35] following these steps. A 23 mL vial containing 65 mg of $ZrCl_4$ and 5 mL of DMF was sonicated for 12 min. Subsequently, 0.5 mL of concentrated HCl, acting as a reaction catalyst, was introduced, and the mixture underwent further sonication for 10 minutes. To promote ligand complexation, 72 mg of $H_2NC_6H_3$-1,4-$(CO_2H)_2$ (ligand) and an additional 15 mL of DMF (solvent) were introduced to the vial. The resulting mixture was sonicated for 20 minutes to achieve complete dissolution of all precursors. Subsequently, the sealed vial was subjected to thermal activation at 100 °C for 2-3 hours, facilitating the formation of the desired white catalyst particles. The solid product was isolated through repeated washing with $(CH_3)_2NC(O)H$ solvent and centrifugation (3000 rpm) to eliminate residual reaction media. The purified catalyst underwent further washing steps with absolute ethanol (C_2H_5OH) to replace the higher boiling point DMF solvent. This solvent exchange step promotes enhanced porosity and adsorption capacity within the final catalyst structure. Following adsorption, the solid phase was isolated once again through centrifugation at 3000 rpm. Subsequently, the recovered adsorbent was dried and its weight was determined under vacuum (30-40 mbar) at a temperature of 373 K. A detailed discussion on the optimization of NH_2-UiO-66 synthesis is provided in a previous publication by the authors [36].

2.4. Adsorption test procedure

A stock solution containing 500 parts per million of dye in deionized water (2000 mL) was synthesized. Samples were acquired by diluting the stock solution to the desired dye concentrations (40, 70, 100, and 130 ppm). The specified quantity of NH_2-UiO-66 adsorbent (at concentrations of 100, 300, and 500 ppm) was introduced into a 100 mL dye solution while maintaining continuous agitation on a shaker at 200 rpm. To ensure consistent temperature control during the adsorption process, a water circulation system was utilized. The experimental temperatures were set at 298 K, 313 K, and 325 K. The pH of the solution was meticulously adjusted using sodium hydroxide (NaOH) for alkaline conditions and hydrochloric acid (HCl) for acidic conditions, targeting specific values of 3, 7, and 10. Aliquots were withdrawn from the reaction mixture at predetermined time intervals for subsequent analysis. These samples were then filtered through a 0.22-micrometer membrane filter to remove the adsorbent particles. The absorbance of post-filtration samples was quantified using a UV-Vis spectrophotometer. Subsequently, dye concentration was ascertained by referencing a pre-constructed calibration curve. To guarantee data reliability, these measurements were replicated until consistent dye content was observed across a minimum of four consecutive samplings. Fig. 1 shows the reaction mixture at various stages of synthesis.



Figure. 1. From left to right: zirconium tetrachloride suspension before entering and after leaving the ultrasonic bath, reaction mixture 12 hours after entering the oven (step out), washed and dried adsorbent

3. Results and Discussion

3.1. Characterization of the synthesized adsorbent

The X-ray diffraction (XRD) pattern of the synthesized NH_2-UiO-66 is depicted in Fig. 2. This pattern indicates the crystalline nature of the adsorbent and aligns with similar descriptions found in existing references [37,38]. The IR spectra of this adsorbent are depicted in Fig. 3. The IR spectrum of the produced catalyst corresponds to the spectra identified in the previously published references [37,38].

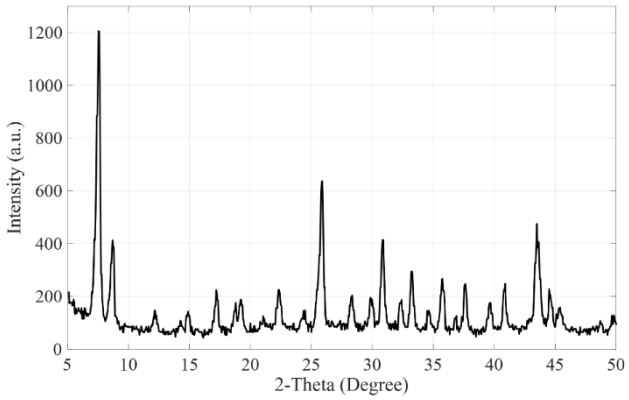


Figure. 2. Powder XRD pattern of synthesized NH_2-UiO-66

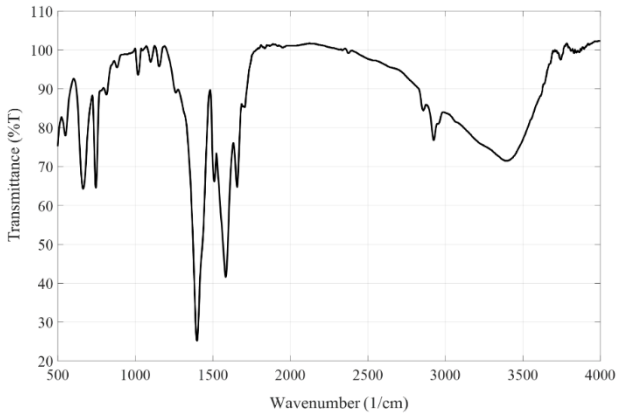


Figure. 3. The IR spectrum of synthesized NH_2-UiO-66

Tambat et al. found significant peaks at wavenumbers of 3452, 3348, 2988, 1564, and 1381 cm^{-1} [32]. Based on their research, the distinctive absorption spectra for NH_2-UiO-66 have been analyzed, and the absorption bands at 3449 cm^{-1} and 3352 cm^{-1} were determined as the result of stretching vibrations of the amine functional group, specifically the asymmetric and symmetric modes, respectively. Whereas, the absorption peak observed at 3002 cm^{-1} corresponds with the C-H stretching mode associated with the physisorbed N, N-dimethylformamide. However, the major absorption peaks for carboxylic acid functional groups at 1558 cm^{-1} and 1368 cm^{-1} are attributed to the symmetric and asymmetric stretching vibrations, respectively. In the present study, these peaks were detected at wavenumbers 3748, 3399, 2921, 1582 cm^{-1}, and 1401 cm^{-1}, aligning with the findings reported by Tambat [32]. Based on the BET analysis, the synthesized adsorbent exhibits an approximate specific surface area of 825 m^2/g, a total pore volume of 0.463 cm^3/g, and a mean pore diameter of 22.46 Å. Fang et al. [1] reported contrasting values for their solvothermally synthesized NH_2-UiO-66: a specific surface area of 509 m^2/g, a pore volume of 0.252 cm^3/g, and a mean pore diameter of 19.79 Å. These values differ slightly from those obtained in the present study.

3.2. Effect of initial dye concentration

To examine the effect of dye concentration on adsorption capacity, this research employed a range of concentration levels: 40 ppm, 70 ppm, 100 ppm, and 130 ppm. To isolate this effect, all other parameters were rigorously controlled. A constant adsorbent dosage of 300 ppm, an adsorption temperature of 298 K, and the natural solution pH were maintained across all experiments. Interestingly, the as-prepared hematite dye solutions (40-130 ppm) inherently possessed a natural pH. The findings pertaining to the correlation between adsorption capacity (Q_t) and contact time (t) are presented in Fig. 4. The following equation was utilized to calculate the adsorption capacity:

$$Q_t = (C_i - C_t)(V/M) \quad (1)$$

where C_i (ppm) and C_t (ppm) symbolize the initial and time-dependent dye concentrations, respectively. V (L) represents the solution volume, and M (g) denotes the mass of the employed adsorbent. The ability to adsorb increases with higher dye concentrations. In accordance with the findings of Fang et al. [1], the increase in the initial concentration of methylene blue dye results in an augmented adsorption capacity for NH_2-UiO-66. This phenomenon is interpreted as an intensification of the concentration gradient effect. This interpretation is bolstered by the findings of Tambat et al. [32] and Li et al. [30]. These studies observed consistent dye removal patterns for Safranin and Acid Chrome Blue K dyes, respectively, using both NH_2-UiO-66 and UiO-66. Based on this alignment with prior research, the present investigation focuses on the adsorption of Safranin onto NH_2-UiO-66. The increased adsorption capacity can be ascribed to a more pronounced concentration gradient, which promotes a more efficient mass transfer process between the adsorbent (NH_2-UiO-66) and the adsorbate (Safranin dye). As illustrated in the accompanying figure, the equilibrium adsorption capacity (Q_e) exhibits a positive correlation with increasing initial dye solution concentrations (40, 70, 100, and 130 ppm), reaching values of 121, 145, 186, and 241 $mg \cdot g^{-1}$, respectively. Equilibrium adsorption capacity (Q_e) demonstrates a near-linear dependence on the initial dye concentration, as

corroborated by a high linear regression correlation coefficient (R^2 = 0.981). This observation aligns with the previous work of Tambat et al. [32], which reported the effectiveness of NH_2-UiO-66 in removing Safranin dye from aqueous solution.

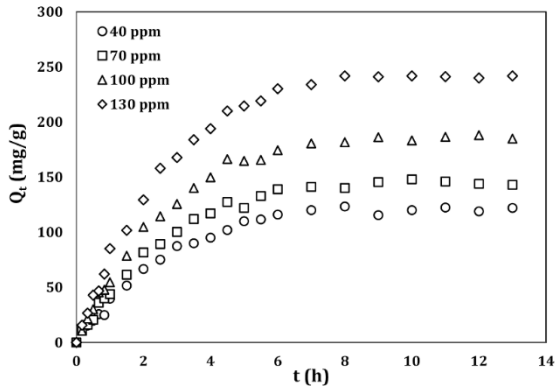


Figure. 4. Adsorption capacity variation with changes in Dye Concentration at T=298 K, MOF=300 ppm, pH=7

3.3. Effect of the amount of NH_2-UiO-66

Fig. 5 shows a plot of Q_t vs contact time for various adsorbent quantities. In this study, the amount of MOF was in the range of 100-500 ppm, with three levels (100, 300, and 500 ppm). Fig. 5 shows an inset of a sample solution before and after adsorption, which became practically colorless after 13 hours. A positive correlation was observed between the adsorbate quantity (Q_t) and the adsorbent mass, indicating a direct relationship between available adsorption sites and contaminant uptake. This aligns with the observations reported by Fang et al. [1] during the adsorption and removal of methylene blue (MB), a positively charged dye, using NH_2-UiO-66 as the adsorbent. Furthermore, employing a minimal adsorbent dosage (100 ppm) necessitated an extended equilibration time exceeding 22 hours. In contrast, a larger amount of adsorbent material (500 ppm) reached equilibrium within just 4 hours, highlighting rapid adsorption of the dye. This is owing to increased site availability and the enhanced possibility of dye collection from aqueous solution. The equilibrium adsorption capacity (Q_e) values exhibited a positive correlation with increasing NH_2-UiO-66 adsorbent concentrations (100, 300, and 500 ppm), reaching values of 131, 186, and 190 mg. g^{-1}, respectively. However, the observed increase in Q_e plateaued at higher adsorbent dosages (300 ppm), suggesting a diminishing return effect on adsorption capacity with further increases in NH_2-UiO-66 concentration. This can be attributed to the availability of more active binding sites on the adsorbent surface at the higher dosage. Meanwhile, because the solution under test contains a limited number of pigment particles, increasing the number of accessible active sites from 300 to 500 ppm will no longer result in a significant rise in Q_e value. As a result, the upper limit of this variable has been set at 500 ppm.

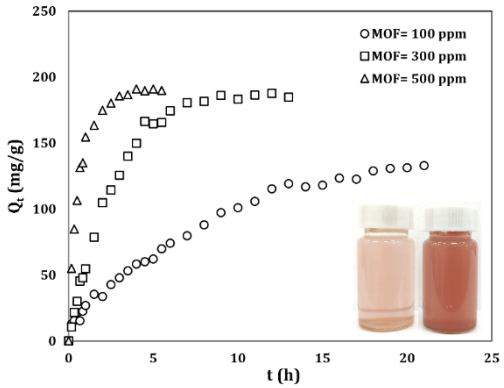


Figure. 5. The effect of NH_2-UiO-66 amount on adsorption capacity (T=298 K, C_i= 100 ppm, and pH=7). The inset: a sample solution before and after adsorption, which became nearly colorless after 13 hours.

3.4. Effect of adsorption temperature

Fig. 6 illustrates a pronounced dependence of the equilibrium adsorption capacity (Q_t) for hematite adsorption onto NH_2-UiO-66 on the employed temperature. The data reveal a clear and consistent increase in Q_t with increasing temperature, from 298 K to 313 K and further to 328 K. This observation aligns with the findings reported by He et al. [3] for the adsorption of Rhodamine B dye onto UiO-66. This alignment suggests a potentially analogous underlying mechanism governing the temperature-dependent adsorption behavior in the present system. As shown in Fig. 6, the equilibrium capacities at 298, 313, and 328 K are 186, 250, and 290 $mg.g^{-1}$, respectively. These results point to an endothermic adsorption process. Higher temperatures improve dye molecule transfer into adsorbent particle surfaces by enhancing dye molecule diffusion across the external boundary layer and decreasing solution viscosity. At lower temperatures (298 K), it took more than 9 hours for the Q_t value to reach equilibrium, while at higher temperatures (328 K), the Q_t value reached equilibrium in about 3 hours. This indicates that dye molecule diffusion and adsorption are faster at higher temperatures.

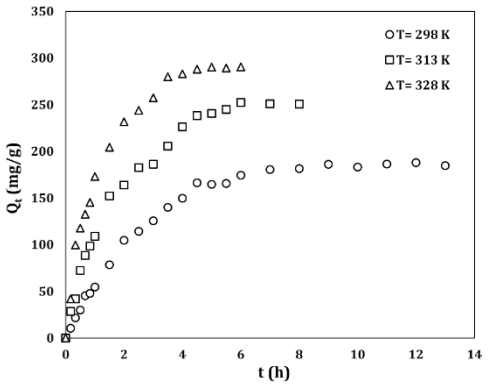


Figure. 6. The effect of temperature effect on adsorption capacity (C_i= 100 ppm, MOF=300 ppm, and pH=7).

3.5. Effect of solution pH

In adsorption processes, the pH of the system is a critical parameter as it alters the zeta potential (surface electric charge) of the adsorbent material. This study systematically investigated the effect of pH on the adsorption process over the range of 3 to 10, with three discrete levels (3, 7, and 10) examined. Fig. 7 depicts the relationship between the equilibrium adsorption capacity (Q_t) and the contact time at these varying pH conditions. The observed trends closely mirror those identified previously in Fig. 4 (initial dye concentration) and Fig. 6 (adsorption temperature), suggesting a potential underlying influence of pH on the adsorption mechanism. The corresponding equilibrium adsorption capacities (Q_e) at the three pH levels were 47, 186, and 79 mg. g^{-1}, respectively, with the maximum adsorption occurring at the neutral pH of 7. The results presented herein emphatically demonstrate the critical role of pH in regulating the adsorption performance of the employed adsorbent material.

The observed maximum equilibrium adsorption capacity (Q_e) at neutral pH is due to fluctuations in the surface charge of NH_2-UiO-66, as shown by its zeta potential (ZP) over the pH range studied. Tambat et al. found that the ZP of NH_2-UiO-66 is negative at pH = 10 (-25 mV), generally steady at pH = 7 (-24 mV), and positive at pH = 3 (8 mV), with a point of zero charge (PZC) at pH = 3.5 [32]. The surface charge properties of NH_2-UiO-66, as defined by its ZP, have been shown to vary with pH. At pH values exceeding 3.5, the adsorbent exhibits a negative charge, while it becomes positively charged at lower pH (below 3.5). Therefore, a comprehensive investigation of the adsorbent's surface charge, as measured by zeta potential, is crucial for elucidating the adsorption behavior of hematite pigments onto NH_2-UiO-66 across a broad pH range. It is noteworthy that existing data on this subject demonstrates significant inconsistencies. Forbes and Franks found that the ZP of hematite at 298 K and pH values of 10, 7, and 3 were -10, +20, and more than +55 mV, respectively [39]. Abaka-Wood et al. reported that the ZP value of hematite at pH values of 10, 7, and 3 were -8, zero, and +19 mV, respectively [40]. Yang et al. reported that the zeta potential of hematite at pH values of 10, 7, and 3 were -32, -20, and +5 mV, respectively [41]. Fan et al. [42] reported these values as -8, zero, and +20 mV, which are similar to the values reported by Abaka-Wood et al. [40]. Shrimali et al. reported that the ZP values of hematite at pH values of 10, 7, and 3 were less than -60, -16, and +40 mV, respectively [43]. The high dispersion of available data may be due to the variety of hematite dyes and the difference in the amount and type of impurities associated with this pigment. Hematite is a natural mineral pigment that is obtained primarily from natural sources, which is the primary reason for the high variability in the data.

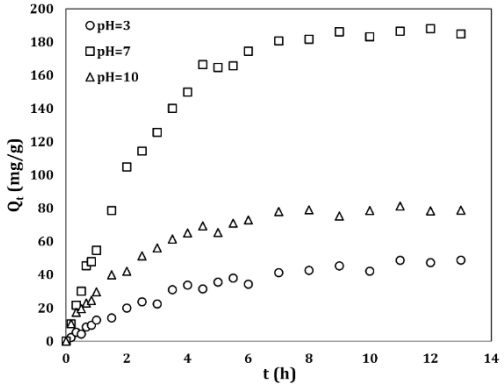


Figure. 7. The effect of solution pH on adsorption capacity (C_i= 100 ppm, MOF=300 ppm, and T=298 K).

The findings in Fig. 7 are consistent with the zeta potential values reported by Forbes and Franks [39]. Tambat et al. also reported the ZP of the adsorbent at pH values of 10, 7, and 3 as -25, -24, and +8, respectively [32]. According to Forbes and Franks [39], this indicates that at pH=10 (-25 and -10 mV) and pH=3 (+8 and > +55), the adsorbent and pigment have the same surface charge. However, at pH=7, the surface charges of the adsorbent and pigment have opposite signs (+20 and -24), which leads to a more efficient adsorption process than at the previous two pHs (as shown in Fig. 7). The optimal fulfillment of this separation process's operational, economic, and environmental considerations is indicated by the absence of extremely acidic and alkaline operating conditions, as well as the presence of extreme adsorption capacity around neutral pH.

3.6. Effect of adsorbent regeneration

In accordance with the aforementioned criteria for an ideal adsorbent, its reusability was investigated. This involved evaluating the regeneration and material recycling of the used adsorbent over four sorption-desorption cycles. To achieve this, the post-sorption material was isolated using a Dura-pore 0.22 µm filter, followed by a washing step and drying at 100 °C under a vacuum pressure of 30-40 mbar. Following meticulous regeneration using a 0.01 N sodium hydroxide solution, as described by Tambat et al. [32, 44], the NH_2-UiO-66 MOF was desiccated under reduced pressure at 100 °C within an electric oven. Subsequent adsorption cycles employed the regenerated MOF. As depicted in Fig. 8, the NH_2-UiO-66 exhibited exceptional regeneration efficiency, consistently exceeding 92% across multiple cycles. This observation signifies the remarkable reusability of the NH_2-UiO-66 MOF, maintaining a consistent adsorption capacity for at least three regeneration cycles.

3.7. Adsorption isotherms

Experimental adsorption equilibrium data were analyzed using four prominent adsorption isotherm models. The suitability of these models was evaluated comparatively through the calculation of their corresponding correlation coefficient (R^2) values. Table 1 presents the non-linear and linearized forms of the employed isotherm equations, as derived from references [45] and [46]. Notably, within these equations, Q_m represents the theoretical maximum adsorption capacity ($mg \cdot g^{-1}$), while C_o and C_e designate the initial and equilibrium hematite concentrations ($mg \cdot L^{-1}$), respectively.

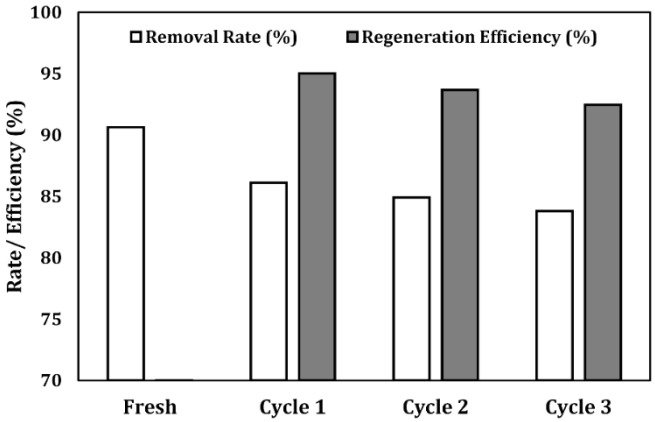


Figure. 8. The removal rate and regeneration efficiency of hematite on NH_2-UiO-66 at different adsorption cycles (C_i= 40 ppm, MOF=300 ppm, pH= 7, and T=298 K).

Table 1. Analysis of the non-linear and linearized equations for various adsorption isotherm models [45,46]

Isotherm model	Linear equation	Non-linear equation	Separation factor (favorability of the adsorption)
Langmuir	$\frac{C_e}{Q_e} = \frac{1}{K_L Q_m} + \frac{C_e}{Q_m}$	$Q_e = \frac{K_L Q_m C_e}{(1 + K_L C_e)}$	$R_L = \frac{1}{(1 + K_L C_0)}$
Freundlich	$Ln(Q_e) = \frac{1}{n} Ln(C_e) + Ln(K_F)$	$Q_e = K_F C_e^{1/n}$	$1/n$
Temkin	$Q_e = \frac{RT}{K_T} Ln(C_e) + \frac{RT}{K_T} Ln(A_T)$	$Q_e = \frac{RT}{K_T} Ln(A_T C_e)$	---
Dubinin-Radushkevich	$Ln(Q_e) = Ln(Q_s) - K\varepsilon^2$ where $\varepsilon = RTLn\left(1 + \frac{1}{C_e}\right)$		---

Within the Langmuir isotherm framework, the Langmuir constant (K_L, L mg^{-1}), is employed to quantify the rate of adsorption. The dimensionless separation factor (R_L) serves to evaluate the efficacy of the adsorption procedure. A favorable adsorption outcome is indicated by a value of R_L within the range of 0 to 1. In contrast, R_L values that surpass 1 signify an unfavorable adsorption process, whereas a value of zero denotes an irreversible adsorption condition [29]. Within the Freundlich isotherm equation, K_F and n represent adsorption capacity and process favorability, respectively. The value of n^{-1} serves as an indicator of the isotherm type. Specifically, $n^{-1} = 0$ signifies irreversible adsorption, $0 < n^{-1} < 1$ indicates favorable adsorption conditions, and $n^{-1} > 1$ suggests unfavorable adsorption [29]. Within the Temkin isotherm model, the parameter A_T represents the equilibrium binding constant. K_T represents the constant correlated with fluctuations in adsorption energy. In contrast, the Dubinin-Radushkevich model introduces K as the adsorption energy constant, and ε as the Polanyi potential [45]. Table 2 presents a summary of the fitting R^2 values and their corresponding isotherm constants. A graphical depiction of these results is provided in Fig. 9. The Langmuir isotherm model postulates a monolayer adsorption process on a homogeneous surface with a finite number of non-interacting sites. This model signifies the formation of a single layer of adsorbates. In this study, the linear Langmuir isotherm yielded the highest R^2 value of 0.88 compared to other evaluated isotherm models, indicating its superior capacity to represent the experimental data. Furthermore, the separation factor (R_L) values calculated for initial dye concentrations (40, 70, 100, and 130 ppm) ranged from 0.208 to 0.075, indicating favorable adsorption across the concentration range. Consequently, the Langmuir model is inferred to be the most appropriate representation of the adsorption process, with the data following a linear Langmuir isotherm. Conversely, the non-linear Langmuir isotherm yielded a considerably lower R^2 value (0.55), signifying a poor fit for the current data set. However, the R_L values (0.025 - 0.078) obtained for the non-linear Langmuir model still indicate a favorable adsorption isotherm. The Freundlich isotherm, on the other hand, provides a well-established framework for analyzing adsorption processes on heterogeneous surfaces where multi-layer coverage can occur. This phenomenon is attributed to the inherent energetic variability of active sites and interactions between adsorbed molecules, as corroborated by reference [23]. The applicability of the Freundlich isotherm in this study was evaluated through linear and non-linear regression analyses, yielding R-squared values of 0.77 and 0.75, respectively. The results of the experimental data indicate a relatively satisfactory correspondence between the modeled outputs

and the empirically observed values. Furthermore, the estimates of the separation factor values for both the linear and non-linear forms of the isotherm were situated within the range of 0-1 (interval of 0.213 and 0.260), denoting advantageous adsorption conditions.

The Temkin isotherm, explored by [32], incorporates the influence of indirect interactions between adsorbate molecules on the adsorption isotherm. However, the correlation coefficients (R^2) of 0.69, presented in Table 2 for both linear and non-linear forms of this model, suggest a moderate fit at best with the experimental data. Similarly, the Dubinin-Radushkevich isotherm, which accounts for inherent sorbent properties and energy transfer during adsorption, exhibits an inadequate fit to the data. This is reflected by its corresponding correlation coefficient of 0.54.

Table 2. The calculated constants of the studied isotherm

Model		Constants			
Langmuir	Linear	Q_m (mg/g)	250.0	R_L	0.208 for C_0= 40 ppm 0.130 for C_0= 70 ppm 0.095 for C_0= 100 ppm 0.075 for C_0= 130 ppm
		K_L (L/mg)	0.095		
		R^2	0.88		
	Non-linear	Q_m (mg/g)	210.3	R_L	0.078 for C_0= 40 ppm 0.046 for C_0= 70 ppm 0.033 for C_0= 100 ppm 0.025 for C_0= 130 ppm
		K_L(L/mg)	0.296		
		R^2	0.55		
Freundlich	Linear	K_F (mg/g)	86.392		
		n	4.701	n^{-1}	0.213
		R^2	0.77		
	Non-linear	K_F (mg/g)	74.330		
		n	3.849	n^{-1}	0.260
		R^2	0.75		
Temkin (T=298 K)	Linear	K_T (L/mg)			70.208
		A_T			6.041
		R^2			0.69
	Non-linear	K_T (L/mg)			70.210
		A_T			6.042
		R^2			0.69
Dubinin-Radushkevich		K			1.303E-6
		Q_s (mg/g)			188.1
		R^2			0.54

Evaluation of the model fitting for the experimental equilibrium adsorption data of hematite onto NH_2-UiO-66 revealed that the linear Langmuir, linear Freundlich, and non-linear Freundlich models exhibited a superior fit compared to other models, as evidenced by their comparatively higher R^2 values. However, amongst these three, the linear Langmuir model emerged as the most favorable choice. This observation aligns with prior research, such as the work of He et al. on the adsorption of Rhodamine B dye onto UiO-66 [3]. Selecting an appropriate isotherm model is crucial for characterizing the adsorption equilibrium of this Zr-incorporated metal-organic framework (MOF). As evidenced by the presented regression coefficients, both the Langmuir and Freundlich models demonstrate efficacy in depicting the adsorption process on this MOF substrate. This aligns with findings from Embaby et al. [23], where anionic dyes displayed Langmuir isotherm behavior during adsorption onto UiO-66. Conversely, Tambat et al. [32] and Fang et al. [1] observed that the adsorption of cationic dyes onto NH_2-UiO-66 materials aligns

more closely with the Freundlich isotherm. It is also noteworthy that Molavi et al. investigated the adsorption of methyl orange and methylene blue dyes onto prepared UiO-66 [35]. The applicability of the Freundlich adsorption isotherm for both anionic and cationic dye adsorption mechanisms suggests a minimal interaction between adsorbate molecules. This, coupled with the observed adsorption behavior on NH_2-UiO-66 as depicted in the preceding data, lends credence to the hypothesis of monolayer adsorption. Furthermore, the suitability of the Langmuir adsorption model implies a homogeneity of sorption sites, signifying that the occupation of neighboring sites does not influence the individual adsorbate's binding affinity.

3.8. Adsorption kinetics

To elucidate the fundamental mechanism governing hematite pigment adsorption and the interactions occurring at the solid-liquid interface, a kinetic analysis was conducted. This investigation serves to identify the rate-determining step of the adsorption process. It is well recognized that various factors can influence adsorption mechanisms, such as mass transfer limitations at the interface, interfacial chemical reactions, and intra-particle diffusion within the adsorbent. To clarify the governing kinetic mechanism of the adsorption process, the experimental data were analyzed by fitting with four kinetic models. Specifically, the pseudo-first-order, pseudo-second-order, Elovich, and intraparticle diffusion models were employed, and their corresponding mathematical expressions are presented as detailed below [29]:

$$Ln(Q_e - Q_t) = Ln(Q_e) - k_1 t \quad (2)$$

$$\frac{t}{Q_t} = \frac{1}{k_2 Q_e^2} + \frac{t}{Q_e} \quad (3)$$

$$Q_t = \frac{1}{\beta} Ln(\alpha\beta) + \frac{1}{\beta} Ln(t) \quad (4)$$

$$Q_t = k_3 + k_4 t^{\frac{1}{2}} \quad (5)$$

Kinetic models are characterized by rate constants, k_1 (h^{-1}) and k_2 ($g \cdot mg^{-1} \cdot h^{-1}$), respectively. The Elovich equation incorporates additional parameters, α ($mg \cdot g^{-1} \cdot h^{-1}$) and β ($g \cdot mg^{-1}$), representing the initial adsorption rate and desorption constant, respectively. Furthermore, k_3 ($mg \cdot g^{-1} \cdot h^{-0.5}$) and k_4 ($mg \cdot g^{-1} \cdot h^{-0.5}$) account for the influence of boundary layer thickness on the intra-particle diffusion rate and boundary layer resistance, respectively. Fig. 10 presents the linearized forms of the investigated kinetic models, corresponding to equations (2) to (5). The R^2 values and all model parameter values are additionally provided in Table 3.

Kinetic modeling of the adsorption process revealed that pseudo-order n models (encompassing both first and second-order) provided the most suitable fit for the empirical data. However, the pseudo-second-order model exhibited a superior performance, evident from its calculated equilibrium adsorption capacity (Q_e^{Cal}) closely aligning with the experimentally determined Q_e^{Exp}. Conversely, the intraparticle diffusion model displayed the lowest coefficient of determination ($R^2 = 0.91$), signifying its inadequacy. Internal diffusion models propose that the rate-determining step in adsorption can be attributed to mass transfer limitations within the adsorbent particle, often characterized by a low intraparticle diffusion coefficient. As demonstrated in Section 3.1, the synthesized NH_2-

UiO-66 exhibits a significant mean pore diameter (22.46 Å), surpassing the size of any employed dye molecule as reported in reference [29].

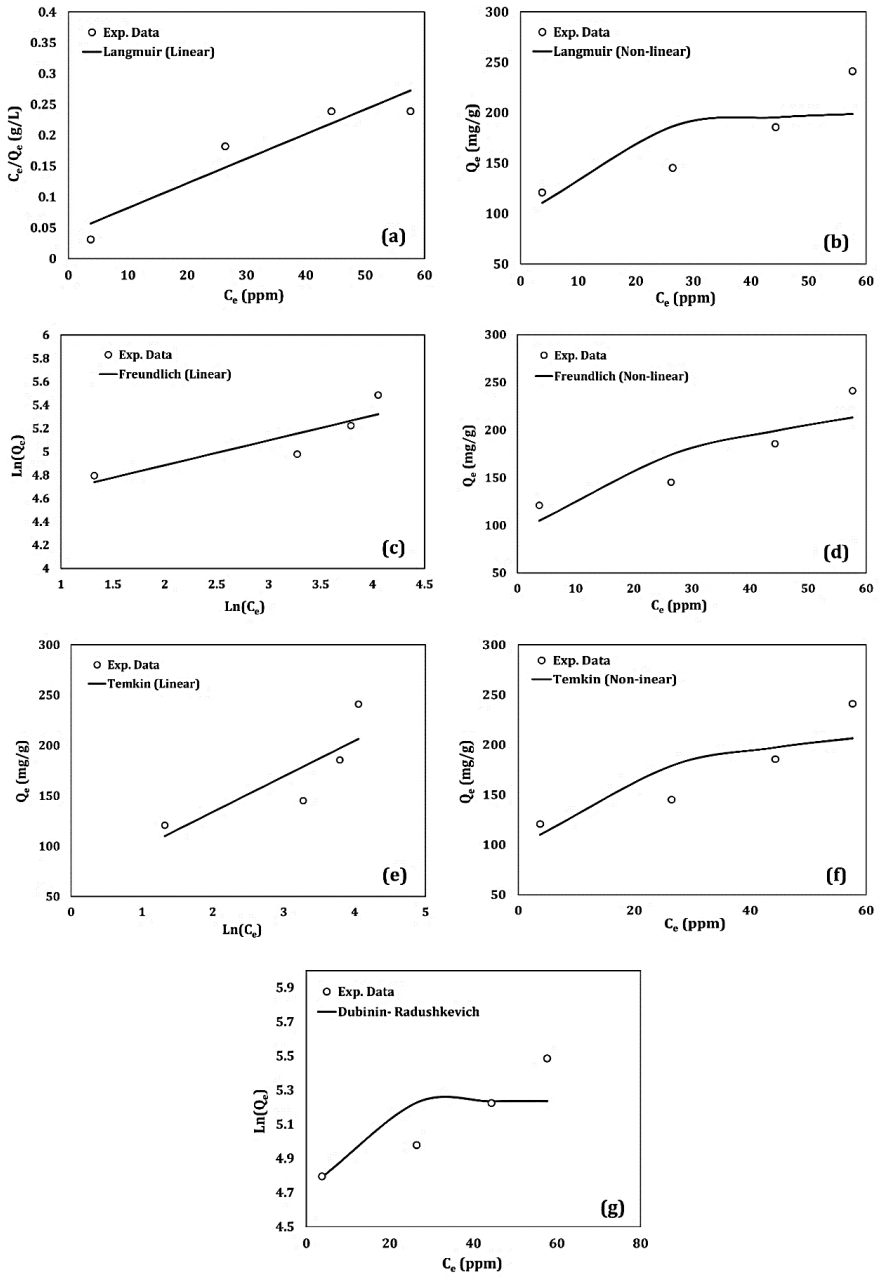


Figure. 9. The presentation of regression graphs for hematite adsorption on NH_2-UiO-66: linear fittings (a, c, e) and non-linear fittings (b, d, f, g).

This translates to unhindered diffusion of dye molecules throughout the adsorbent's pores, effectively eliminating this phenomenon as the rate-limiting factor. This

observation aligns perfectly with the observed poor fit (R^2 = 0.91) of the intraparticle diffusion model when applied to the experimental data.

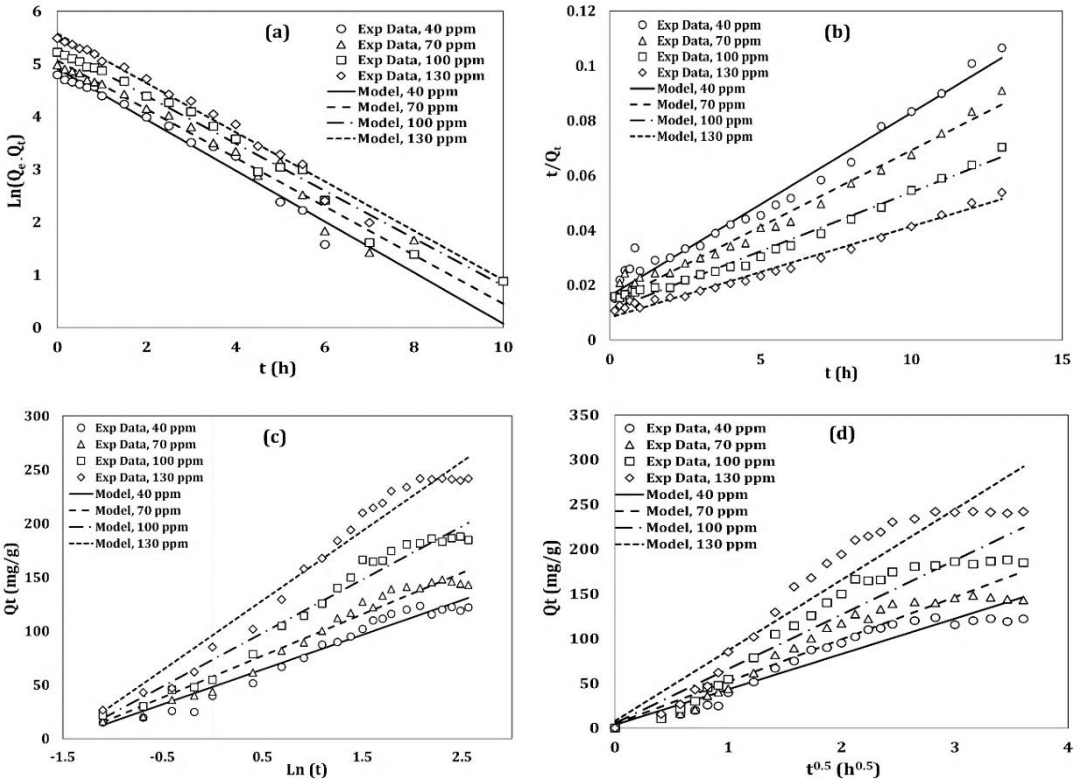


Figure. 10. The plot of (a) Pseudo first-order, (b) Pseudo second-order, (c) Elovich, and (d) Intra-particle diffusion kinetic models.

An R^2 value of 0.96 obtained for the Elovich model suggests a relatively weak correlation, implying that this model may not be the most suitable for describing the adsorption behavior of hematite onto NH_2-UiO-66. The Elovich equation is typically employed in adsorption kinetics to characterize chemical adsorption mechanisms. Consequently, the findings of this study favor a physical rather than a chemical adsorption process for hematite on NH_2-UiO-66.

Table 3. The kinetic constants of hematite adsorption on NH_2-

Items	Q_e^{Exp}	Q_e^{Cal}	k_1 (h^{-1})	k_2($g.mg^{-1}.h^{-1}$)	α ($mg.g^{-1}.h^{-1}$)	β($g.mg^{-1}$)	k_3($mg.g^{-1}.h^{-0.5}$)	k_4 ($mg.g^{-1}.h^{-0.5}$)	R^2	Ave. R^2
Pseudo first-order model										
C_0=40 ppm	121	136	0.4833	---	---	---	---	---	0.97	
C_0=70 ppm	145	158	0.4613	---	---	---	---	---	0.97	0.98
C_0=100	186	199	0.4499	---	---	---	---	---	0.98	
C_0=130	241	263	0.4669	---	---	---	---	---	0.98	
Pseudo second-order model										
C_0=40 ppm	121	150	---	0.0028	---	---	---	---	0.96	
C_0=70 ppm	145	180	---	0.0023	---	---	---	---	0.97	0.97
C_0=100	186	232	---	0.0017	---	---	---	---	0.97	
C_0=130	241	301	---	0.0014	---	---	---	---	0.97	
Elovich model										
C_0=40	121	---	---	---	143	0.0310	---	---	0.95	
C_0=70 ppm	145	---	---	---	171	0.0259	---	---	0.96	0.96
C_0=100	186	---	---	---	217	0.0201	---	---	0.97	
C_0=130	241	---	---	---	285	0.0155	---	---	0.96	
Intraparticle diffusion model										
C_0=40 ppm	121	---	---	---	---	---	3.64	39.54	0.91	
C_0=70 ppm	145	---	---	---	---	---	4.69	47.22	0.91	0.91
C_0=100	186	---	---	---	---	---	5.34	60.69	0.92	
C_0=130	241	---	---	---	---	---	7.73	78.89	0.91	

3.9. Thermodynamic study

The thermodynamic behavior of this system was studied using the following equations:

$$Ln(K_F) = \frac{\Delta S_0}{R} - \frac{\Delta H_0}{RT} \quad (6)$$

$$\Delta G_0 = -RTLn(K_F) \quad (7)$$

K_F denotes the Freundlich constant ($mg.g^{-1}$) and T denotes temperature (K). Table 4 shows the thermodynamic parameters for the tested temperatures. Negative ΔG_0 results illustrate the process's viability and the adsorption's spontaneous behavior at the temperatures examined [3]. Thermodynamic analysis reinforces the observations presented in Fig. 6. The decreasing ΔG_0 with increasing temperature signifies a more favorable adsorption process at higher temperatures. This aligns well with the endothermic nature of hematite adsorption onto NH_2-UiO-66, as indicated by the positive ΔH_0 value (5.149 kJ. mol^{-1}). Furthermore, this ΔH_0 value falls within the range reported by Kara et al. [47] and He et al. [3] for physical adsorption (less than 40 $kJ.mol^{-1}$). In conjunction with the results obtained from kinetic modeling experiments, the aforementioned thermodynamic data provides compelling evidence that the adsorption of hematite onto NH_2-UiO-66 occurs via a physisorption mechanism.

Table 4. The determination of thermodynamic properties for the sorption of hematite on NH_2-UiO-66 surface.

T (K)	K_F (mg/g)	ΔG_0 (J/mol)	ΔH_0 (J/mol)	ΔS_0 (J/mol.K)
298	86.39	-3703.7		
313	94.26	-3940.5	5148.9	54.3
328	104.52	-4190.7		

4. Conclusion

Metal-organic frameworks (MOFs) have emerged as a prominent class of materials for wastewater dye remediation due to their exceptional properties. Their potential applications in this area have been elucidated due to their unique characteristics. However, the existing literature predominantly focuses on the removal of organic dyes. This study reports the solvothermal synthesis of NH_2-UiO-66 and investigates the impact of four operational parameters on its capacity to adsorb hematite, an inorganic pigment. These parameters include dye concentration, adsorption temperature, adsorbent dosage, and solution pH. The experimental results demonstrate the effectiveness of NH_2-UiO-66 in hematite removal. The adsorption equilibrium was effectively modeled by both the linear Freundlich and Langmuir isotherms, with the latter exhibiting a superior fit. The pseudo-first-order model yielded an equilibrium adsorption capacity that closely mirrored the experimental values, suggesting a dominance of this kinetic mechanism. Furthermore, a positive correlation was observed between adsorption capacity and both temperature and initial dye concentration, suggesting a physisorption mechanism. This observation was complemented by the study's quantification of equilibrium constants, adsorption capacities, and thermodynamic parameters. Notably, the regeneration efficiency remained remarkably high (> 92%) even after three adsorption cycles, indicating excellent reusability of the NH_2-UiO-66 adsorbent with minimal performance degradation.

References

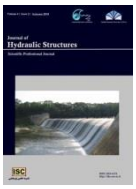
1. Fang Y, Zhang L, Zhao Q, Wang X, Jia X, (2019). Application of acid-promoted UiO-66-NH_2 MOFs in the treatment of wastewater containing methylene blue. Chemical Papers, pp: 73:1401-1411.
2. Zeng L, Xiao L, Long Y, Shi X, (2018). Trichloroacetic acid-modulated synthesis of polyoxometalate@UiO-66 for selective adsorption of cationic dyes. J. Colloid Interface Sci., pp: 516:274–283.
3. He Q, Chen Q, Lü M, Liu X, (2014). Adsorption behavior of rhodamine B on UiO-66. Chin. J. Chem. Eng., pp: 22:1285–1290.
4. Roopaei H, Zohdi AR, Abbasi Z, Bazrafkan M, (2014). Preparation of new photocatalyst for removal of alizarin red-s from aqueous solution. Indian Journal of Science and Technology, pp: 7:1882–1887.
5. Gneedy AH, Dryaz AR, Said MSh, AlMohamadi HA, Ahmed SA, Elsayed R, Soliman NK, (2022). Application of marine algae separate and in combination with natural zeolite in dye adsorption from wastewater: a review, Egyptian Journal of Chemistry, pp: 65:589-616.
6. Sağlam S, Türk FN, Arslanoğlu H, (2023). Use and applications of metal-organic frameworks (MOF) in dye adsorption: review. Journal of Environmental Chemical Engineering, pp: 11: 110568.
7. Lan D, Zhu H, Zhang J, Li Sh, Chen Q, Wang Ch, Wu T, Xu M, (2022). Adsorptive removal of organic dyes via porous materials for wastewater treatment in recent decades: a review on species, mechanisms and perspectives. Chemosphere, pp: 293:133464.
8. De Sousa SR, Rengel HD, Voigt FD, Machado RAF, De Fátima MR, Marangoni C, (2023) Treatment of real textile wastewater by coagulation/flocculation integrated with direct contact membrane distillation. Separation Science and Technology, pp: 58:2394-2410.
9. Wang H, Song J, Yan M, Li J, Yang J, Huang M, Zhang R, (2023). Waste lignin-based cationic flocculants treating dyeing wastewater: fabrication, performance, and mechanism. Science of The Total Environment, pp: 874:162383.
10. Kolya H, Kang CW, (2023). Bio-based polymeric flocculants and adsorbents for wastewater treatment. Sustainability, pp: 15:1-36.
11. Asath Murphy MS, Jovitha Jane D, Sahaya LS, Robin RS, Palanichamy J, Kalivel P, (2023). Electrochemical treatment of textile wastewater using copper electrodes. J Environ Sci Health A Tox Hazard Subst Environ Eng, pp: 58:971-980.
12. Chen Zh, Feng M, Wang Y, Ma Q, Yin Q, (2023) Construction of a novel magnetic levitation iron–carbon micro-electrolysis treatment system for dye wastewater and its anti-passivation strategy. Environ. Sci.: Water Res. Technol., pp: 9:2076-2088.
13. Xie J, Zou X, Chang Y, Xie J, Liu H, Cui MH, Zhang TC, Chen C, (2023). The microbial synergy and response mechanisms of hydrolysis-acidification combined microbial electrolysis cell system with stainless-steel cathode for textile-dyeing wastewater treatment. Sci Total Environ., pp:10:158912.
14. Mim S, Hashem MA, Payel S, (2023). Coagulation-adsorption-oxidation for removing dyes from tannery wastewater. Environ Monit Assess., pp:195: article number 695.
15. Sudirgo MM, Surya RA, Kristianto H, Prasetyo S, Sugih AK, (2023). Application of xanthan gum as coagulant-aid for decolorization of synthetic congo red wastewater. Heliyon, pp: 9: e15011.

16. Yu H, Liu Y, Cong Sh, Xia Sh, Zou D, (2023). Review of Mo-based materials in heterogeneous catalytic oxidation for wastewater purification. Separation and Purification Technology, pp: 312:123345.
17. Shokoohi R, Godini K, Latifi Z, (2023). Catalytic Oxidation of reactive blue 222 dye using peroxymonosulfate activated by Mn_3O_4: parameter optimization using response surface methodology. Inorganic Chemistry Communications, pp: 149:1104.
18. Eskikaya O, Isik Z, Arslantas C, Yabalak E, Balakrishnan D, Dizge N, Rao KS, (2023). Preparation of hydrochar bio-based catalyst for fenton process in dye-containing wastewater treatment. Environmental Research, pp: 216:114357.
19. Yu H, Cai D, Li Sh, Gao C, Xue L, (2023). Tight UF membranes with ultrahigh water flux prepared by in-situ growing ZIF particles in NIPS process for greatly enhanced dye removal efficiency. Journal of Membrane Science, pp: 666:121136.
20. Zhu K, Mohammed S, Tang H, Xie Z, Fang S, Liu S, (2023). ZIF-67/SA@PVDF ultrafiltration membrane with simultaneous adsorption and catalytic oxidation for dyes. Sustainability, pp: 15:2879.
21. Thoa LThK, Thao TThPh, Nguyen-Thi M, Duc Chung N, Ooi ChW, Park SM, Lan TTh, Quang HT, Khoo KSh, Show PL, Duc Huy N, (2023) Microbial biodegradation of recalcitrant synthetic dyes from textile-enriched wastewater by fusarium oxysporum, Chemosphere, pp: 325:138392.
22. Selvan BK, Pandiyan R, Vaishnavi M, Das S, Thirunavoukkarasu M, (2023). Ameliorative biodegradation of hazardous textile industrial wastewater dyes by potential microalgal sp. Biomass Conv. Bioref., pp:13:13481–13492.
23. Embaby MS, Elwany SD, Setyaningsih W, Saber MR, (2018). The adsorptive properties of UiO-66 towards organic dyes: a record adsorption capacity for the anionic dye alizarin red s. Chin. J. Chem. Eng., pp: 26:731-739.
24. Chen Q, He Q, Lv M, Xu Y, Yang H, Liu X, Wei F, (2015). Selective adsorption of cationic dyes by UiO-66-NH2. Applied Surface Science, pp: 327:77-85.
25. Couillard D, (1994). The use of peat in wastewater treatment. Water Research, pp: 28:1261-1274.
26. Bu X.H., Zaworotko M.J., Zhang Zh., Metal-Organic Framework from Design to Applications, first ed., Springer, Nature Switzerland, 2020.
27. Lin H, Jie B, Ye J, Zhai Y, Luo Zh, Shao G, Chen R, Zhang X, Yang Y, (2023). Recent advance of macroscopic metal-organic frameworks for water treatment: a review. Surfaces and Interfaces, pp: 36:102564.
28. Kaur H, Devi N, Siwal SS, Alsanie WF, Thakur MK, (2023). Metal–organic framework-based materials for wastewater treatment: superior adsorbent materials for the removal of hazardous pollutants. ACS Omega, pp: 8:9004–9030.
29. Tambat SN, Ahirrao DJ, Pandit AB, Jha N, Sontakke ShM, (2020). Hydrothermally synthesized N2-UiO-66 for enhanced and selective adsorption of cationic dyes. Environmental Technology & Innovation, pp:19:101021.
30. Li Y, Liu Y, Gao W, Zhang L, Liu W, Jingjing L, Wang Z, Deng YJ, (2014). Microwave-assisted synthesis of UiO-66 and its adsorption performance towards dyes. Cryst. Eng. Comm., pp: 16:7037–7042.
31. Zhang KD, Tsai FC, Ma N, Xia Y, Liu HL, Zhan XQ, Yu XY, Zeng XZ, Jiang T, Shi D, Chang CJ, (2017). Adsorption behavior of high stable Zr-based MOFs for the removal of acid organic dye from water. Materials, pp:10:205.

32. Tambat SN, Sane PK, Suresh S, Varadan ON, Pandit AB, Sontakke ShM, (2018). Hydrothermal synthesis of NH_2-UiO-66 and its application for adsorptive removal of dye. Advanced Powder Technology, pp: 29:2626-2632.
33. Mousavi AV, Ahmadipouya S, Shokrgozar A, Molavi H, Rezakazemi M, Ahmadijokani F, Arjmand M, (2021). Adsorption performance of UiO-66 towards organic dyes: effect of activation conditions. Journal of Molecular Liquids, pp: 321:114487.
34. Qiu J, Feng Y, Zhang X, Jia M, Yao J, (2017). Acid-promoted synthesis of UiO-66 for highly selective adsorption of anionic dyes: adsorption performance and mechanisms. J. Colloid Interface Sci., pp: 499:151-158.
35. Molavi H, Hakimian A, Shojaei A, Raeiszadeh M, (2018). Selective dye adsorption by highly water stable metal–organic framework: long term stability analysis in aqueous media. Appl. Surf. Sci., pp: 445:424-436.
36. Mohammadi A, Sedighi M, Afsari M, (2022). Optimization of the synthesis of UiO-66-NH_2 catalyst and its application for removing organophosphorus pesticides from wastewater. J. Hydraul. Struct., pp: 8:1-16.
37. Yang J, Dai Y, Zhu X, Wang Z, Li Y, Zhuang Q, Shi J, Gu J, (2015). Metal–organic frameworks with inherent recognition sites for selective phosphate sensing through their coordination-induced fluorescence enhancement effect. J. Mater. Chem. A, pp: 3:7445-7452.
38. Guo Zh, Xiao Ch, Maligal-Ganesh RV, Zhou L, Goh TW, Li X, Tesfagaber D, Thiel A, Huang W, (2014). Pt-nanoclusters confined within metal−organic framework cavities for chemoselective cinnamaldehyde hydrogenation. ACS Catal., pp: 4:1340−1348.
39. Forbes, E., Franks, G. V. (2013). Selective separation of hematite from quartz by flotation using a temperature responsive polymer. Proceeding of the Iron Ore Conference, Perth, Australia.
40. Abaka-Wood BG, Addai-Mensah J, Skinner W, (2017). A study of flotation characteristics of monazite, hematite, and quartz using anionic collectors. International Journal of Mineral Processing, pp: 158:55-62.
41. Yang Zh, Han Y, Teng Q, Zhang G, Liu Sh, (2023) Aggregation process of fine hematite particles suspension using xanthan gum in the presence of Fe (III). Arabian Journal of Chemistry, pp: 16:104539.
42. Fan G, Wang L, Cao Y, Li Ch, (2020). Collecting agent–mineral interactions in the reverse flotation of iron ore: a brief review. Minerals, pp: 10:681.
43. Shrimali K, Jin J, Vaziri Hassas B, Wang X, Miller JD, (2016). The surface state of hematite and its wetting characteristics. J. Colloid Interface Sci., pp: 477:16–24.
44. Ishikawa K, Yoshioka T, Sato T, Okuwaki A, (1997). Solubility of hematite in LiOH, NaOH and KOH solutions. Hydrometallurgy, pp: 45:129-135.
45. Priyantha N, Lim LBL, Dahri MKh, Tennakoon DTB, (2013). Dragon fruit skin as a potential low-cost biosorbent for the removal of manganese (II) ions. Journal of Applied Sciences in Environmental Sanitation, pp: 8:179-188.
46. Dada AO, (2012). Langmuir, Freundlich, Temkin and Dubinin–Radushkevich isotherms studies of equilibrium sorption of Zn^{2+} unto phosphoric acid modified rice husk. IOSR Journal of Applied Chemistry, pp: 3:38-45.
47. Kara M, Yuzer H, Sabah E, Celik MS, (2007). Adsorption of cobalt from aqueous solutions onto sepiolite. Water Res., pp: 37:224–232.

© 2024 by the authors. Licensee SCU, Ahvaz, Iran. This article is an open access article distributed under the terms and conditions of the Creative Commons Attribution 4.0 International (CC BY 4.0 license) (http://creativecommons.org/licenses/by/4.0/).

Journal of Hydraulic Structures
J. Hydraul. Struct., 2024; 10(4):46-60
DOI: 10.22055/jhs.2024.47182.1302



OPEN ACCESS

Experimental study of river morphology downstream of the inclined and vertical grade control structures

Seyed Mohamad Mahdi Shariati [1]
Mehdi Hamidi [*1]

Abstract

Grade control structure (GCS) can be used to reduce erosion in river beds. They decrease the river bed scour by changing the flow regime and reducing its velocity. It is required to maintain the stability of these structures against the scour hole that generates downstream of them, so investigating the scour hole characteristics downstream of the GCS is inevitable. In the present research, the equilibrium scour holes downstream of GCS were investigated under three discharges (q=0.00467, 0.00583, 0.00700 m^3/s.m) and two different sedimentation conditions (d_{50}=0.082, 1.6 mm). The results show that in the constant GCS geometry and finer sediment, the maximum scour depth (d_s) and maximum scour hole length (l_s) increase. In the same sedimentary conditions and different geometry, when the slope of the GCS downstream face varied from 90° to 60°, d_s increases, but l_s decreases. Also, the hydraulic jump forms on the scour hole at high flow intensity, which has an essential influence on the geometry of the equilibrium scour hole. Comparison of d_s/H_c between the present study and Ben Meftah and Mossa (2020) has R_2=0.891 and RE=10.66%, which reveals acceptable compatibility between the present study results and previous ones.

Keywords: Experimental model, Grade control structure, Maximum scour depth, River engineering, Sediment transport.

Received: 18 June 2024; Accepted: 30 July 2024

1. Introduction

One problem of hydraulic structures and river engineering is the erosion of the sedimentary beds and sidewalls of rivers or irrigation channels, caused by the interaction of water flow and sediment [1]. Among the countermeasures to reduce this phenomenon, using bed stabilization structures are common, which are divided into different types. One of the most important of these structures is the inclined and vertical grade control structures (GCS). The performance of these structures is according to the conservation mass law; the water depth behind these structures increases, and as a result, the water flow velocity decreases. It is understandable that the higher the flow velocity, the more intensive scour occurs. In fact, by changing the flow regime, the erosion in the sedimentary bed can be reduced to some extent.

[*] E-mail: hamidi@nit.ac.ir **(Corresponding Author)**
[1] Faculty of Civil Engineering, Babol Noshirvani University of Technology, Babol, Mazandaran, Iran.

CC BY

The installation of GCS has become an ideal choice for river engineers to reduce sediment bed erosion because these structures are eco-friendly structures that help river restoration and improve aquatic life [2-4]. The expansion of the scour hole downstream of GCS may cause damage to it [5]. Therefore, studying the development of scour downstream of GCS for their management and safety is necessary. Despite using numerical methods to predict the longitudinal profile of the scour hole around hydraulic structures, experimental techniques, and objective observations still provide researchers with more reliable results. In the following, some of the most important results of the previous experimental studies have been investigated.

In 1991, Bormann and Julien studied the GCS with the different downstream face slopes experimentally. They observed that the maximum scour depth (d_s) downstream of the vertical GCS is dependent on the flow velocity [6]. In 1998, Mossa studied the longitudinal patterns of the scour hole formed downstream of GCS and realized that some of the results obtained (maximum scour depth) were not consistent with the previous technical literature formulas [7]. Therefore, he performed a proper dimensional analysis for better results [7]. Lenzi et al. (2003) performed a comprehensive field and experimental study on the depth of downstream scour holes of seventy-three GCS of the bed sill type in 6 mountainous rivers in the Italian Alps [8]. Their research indicated that the differences in sediment particles in terms of size and lithology have a minor influence on defining the size of the scour hole. The maximum measured scour depth was well calculated by a semi-empirical relation proposed by the experimental data, which showed an average relative error of 0.13 [8]. Marion et al. (2004) evaluated the distance of bed sills from each other and sediment granularity [9]. They found a new relationship for high-gradient flows, i.e., a slope greater than 0.4, and sediment size, which is significantly effective. They focused on the dimensions of the scour hole, which is included in their prediction formula [9]. In 2004, D'Agostino and Ferro investigated the scour hole downstream of a weir [10]. The results of their experiments indicated that the ratio of flow head to weir height can describe the measurements of the scour depth in, both large and small scales. The parameters of the longitudinal scour profiles were calculated more accurately than the scour depth. They seemed to be more affected by the coarse particles of the sedimentary bed [10]. Pagliara and Palermo (2013) investigated the scour hole downstream of rock grade control structures and stepped gabion weirs and concluded that these structures have a significant effect on the flow regime and river morphology [11]. As a result, this flow regime in developing scour holes is effective, and hydraulic jump affects sediment transport significantly [11]. Pagliara and Kurdistani (2014) investigated W and V weirs [12]. They found that the foremost effective parameters for predicting the maximum scour depth and length include the densimetric Froude number, the weir height, and the water drop height. It was observed that the d_s downstream of the W-shaped weir is greater than that of the V-shaped weir [12]. Shafai-Bejestan et al. (2016) evaluated the effects of upward water seepage on d_s [5]. They concluded that, in general, upward seepage reduces the downward velocity close to the bed, which reduces d_s [5]. Rajaee et al. (2018) studied the trapezoidal and rectangular labyrinth weirs [13]. They found that labyrinth weirs have a significant influence on decreasing d_s downstream of GCS, and the scour depth downstream was reduced by 19% in the trapezoidal weir and 10% in the rectangular weir compared to the linear weir [13]. Di Nardi et al. (2021) studied the ability to predict the scour evolution model based on the PTT method using a large data set related to GCS [14]. They figured out that PTT is a valid method for estimating scour development irrespective of the structural configuration and hydraulic conditions. It is unnecessary to provide limited hydraulic conditions to perform the experiments as in the previous studies [14]. The piano key weir (PKW) is a GCS with more hydraulic efficiency, compared to the labyrinth weir [15-16]. Lantz et al. (2022) evaluated the

evolution of scour downstream of the piano key weir [17]. They concluded that the hydraulic conditions, especially in the tailwater, have a significant effect on the equilibrium scour process, which ultimately leads to the scour depth more than the weir height. Khalili and Hamidi (2023) investigated the submerged hydraulic jump formed on the floor downstream of the sluice gate [18]. They observed that the average velocity at the end of the sediment bed is about 18% lower than at the beginning. Scouring occurs in submerged vertical jets downstream of some grade-control structures [19]. Guguloth et al. (2024) predicted scour hole depths for static and dynamic conditions as a result of submerged circular vertical jets with AI models and received accurate results [20].

Some studies show that secondary currents also play an essential role in developing scour holes in GCS. Ben Meftah et al. (2021) in an experimental study indicated that d_s downstream of GCS is formed closer to the sidewalls of the channel and is far from the channel's centerline [21].

It can be concluded by reviewing technical literature that the sedimentary conditions, the flow hydraulic conditions, and the geometry of GCS are the main factors on the longitudinal profile of the scour hole downstream of GCS. Although experimental studies have been performed on the scour downstream of vertical and inclined GCS, most of them are on GCS with an angle of 45° or less. Therefore, this study compared the longitudinal profiles of the scour hole downstream of GCS with 90° and 60°. Also, the effects of geometric changes in GCS and sediment granularity on the longitudinal profile of the scour hole were investigated, and the maximum depth (d_s) and length (l_s) of the scour hole were compared. Two laboratory models of vertical and inclined GCS have been used in the tests. The present study focused on the profile of scour hole development downstream of GCS in different sedimentary and geometry conditions in the same tailwater depth. Dimensional analysis has been provided by using the available equations from previous studies, and the experimental setup was presented based on it and previous data.

2. Materials and methods

2.1. Dimensional analysis

To obtain correct and reliable results each test requires appropriate dimensional analysis according to the scale of the experimental model. According to Noormohammadi et al. [22], the most critical parameters affecting the scour downstream of inclined GCS are the hydraulic conditions, the geometric conditions of the structure, the characteristics of the sedimentary bed, and the time of the scour process.

The physical model in the present study was similar to the study of Ben Meftah and Mossa (2020) [23]. Thus, for this research separate dimensional analyses were not applied and similar effective parameters were used. According to their study, due to the high-velocity gradient between the water inlet and the scour hole, a drag force is generated. If it is greater than the weight of the bed sediment particles, it leads to sediment transport and particle movement. The scouring process reaches an equilibrium condition when the non-cohesive sediment bed particles are not separated from the scour hole and are not transported downstream. In clear water conditions, an equilibrium condition in the scour process occurs when the geometry of the longitudinal profile of the scour hole downstream of the GCS does not change with time under steady flow conditions. Due to the turbulence in the flow, there is a possibility of changes in the final condition of the longitudinal scour patterns downstream of GCS. Based on Mason and Arumugam (1985) [24], these changes are minor and the theory of d_s is acceptable and consistent for the engineering design consideration. Ben Meftah and Mossa (2020) [23] presented Eq. (1) for the influential variables of the scour phenomenon.

$$d_s, l_s = f(d_{50}, H_c, H_t, g, q, Z_d, \lambda, \nu, \rho_s, \rho_w) \quad (1)$$

In Eq. (1), d_s is the maximum scour depth, l_s is the maximum length of the scour hole, d_{50} is the median sediment particle size, H_c is the depth of the water inlet jet or the flow critical depth, H_t is the tailwater depth, g is the acceleration of the earth's gravity, q is the flow discharge per unit width, Z_d is the level difference between the GCS crest and the primary sedimentary bed, λ is the angle between the downstream face of GCS and channel floor, v is the kinematic viscosity of water, ρ_s is the density of sediment particles and ρ_w is the water density. The Eq. (1) can be substituted with dimensionless Eq. (2).

$$\frac{d_s}{H_c}, \frac{l_s}{H_c} = f\left(\frac{d_{50}}{H_c}, \frac{Z_d}{H_c}, \frac{H_t}{H_c}, \frac{1}{Fr_c^2}, \frac{1}{Re}, \lambda, \frac{\rho_s - \rho_w}{\rho_w}\right) \quad (2)$$

In Eq. (2), Fr_c and Re represent Froude's number on the end of the GCS crest and Reynolds number, respectively. In turbulent flow, the influence of Re on the scouring process can be neglected, so the final relation is written as follows.

$$\frac{d_s}{H_c}, \frac{l_s}{H_c} = f\left(\frac{Z_d}{H_c}, \frac{H_t}{H_c}, \lambda, \frac{q}{H_c\sqrt{(\Delta - 1)g.d_{50}}} = \mathrm{Fr_d}\right) \quad (3)$$

In Eq. (3), Fr_d presents the densimetric Froude number, which is written as $\frac{q}{H_c\sqrt{(\Delta-1)g.d_{50}}}$ and term Δ shows $\frac{\rho_s}{\rho_w}$.

Despite the studies that have been carried out on scouring and bed erosion downstream of GCS and available equations that have been obtained, predicting the geometry of the longitudinal profile scour hole in equilibrium conditions is still challenging. In different ranges of hydraulic conditions, different geometries of GCS, and sedimentary conditions, there are several equations, each limited to the dimensional analysis and characteristics of its laboratory conditions. According to Ben Meftah and Mossa (2020) [23], most available equations for GCS were derived from Mason and Arumugam (1985) equation [24], as Eq. (4).

$$d_s + H_t = K\frac{q^a.H^b.H_t^c}{g^e.{d_{50}}^f} \quad (4)$$

H is the gap between the water head level and the tailwater depth, $K = 6.42 - 3.10H^{0.01}$, $a = 0.60 - \frac{H}{300}$, $b = 0.15 - \frac{H}{200}$, c=0.15, e= 0.30 and f=0.10 with assuming d_{50}=0.250.

Among the equations for predicting the maximum scour depth, which includes an extensive range of laboratory data according to the dimensional analysis, is the relation presented by D'Agostino and Ferro (2004) [10]. Despite the many relations offered after that, it is still one of the most valid relations as Eq. (5).

$$\frac{d_s}{Z_d} = 0.54\left(\frac{H_t}{H}\right)^{-0.126}(A_{50})^{0.544}\left(\frac{d_{90}}{d_{50}}\right)^{-0.856}\left(\frac{b_s}{B}\right)^{-0.751}\left(\frac{b_s}{Z_d}\right)^{0.593} \quad (5)$$

where $A_{50} = \frac{Q}{b_s.Z_d.\sqrt{g.d50(\Delta-1)}}$, Q is the flow discharge, B is the channel width, b_s is the width of GCS that may differ from the channel width, and d_{90} is the diameter that 90% of the particles are smaller than it.

One of the newest equations presented to predict d_s and l_s downstream of GCS can be referred to in Eq. (6) and Eq. (7) from Ben Moftah and Mossa (2020) [23]. These equations are presented using a new approach with dimensional analysis.

$$\frac{d_s}{H_c} = 0.24\left(1+\frac{Z_d}{H_c}\right)^{0.92}\left(\frac{H_t}{H_c}\right)^{0.24}\left(\frac{\lambda}{\pi}\right)^{-0.34}(\mathrm{Fr_d})^{0.38} \quad (6)$$

$$\frac{l_s}{d_s} = 2.16\left(\frac{0.22(1+\frac{Z_d}{H_c})^{0.76}(\frac{H_t}{H_c})^{0.68}\left(\frac{\lambda}{\pi}\right)^{-0.16}(\mathrm{Fr_d})^{0.82}(H_c)}{d_s}\right) \quad (7)$$

2.1. Experimental setup

Experimental tests were conducted in a flume with a length of 4 meters, a width of 0.6 meters, and a height of 0.2 meters at the hydraulic lab of Babol Noshirvani University of Technology. This flume was calibrated and used for physical sediment transport in previous studies [25-32]. It includes a channel, upstream and downstream water tank, pump, point gauge, and a gate at the end of the channel to adjust the flow depth (Fig. 1). The flow discharge is controlled by a magnetic flow meter that can supply water up to 0.0083 m^3/s. When the pump turns on, the water flows from the upstream tank into the channel and the downstream tank, and then it transfers to the upstream tank through the pipes installed under the channel. This cyclic procedure continues until the pump is on. The point gauge with a resolution of 0.1 mm was used to achieve the flow depths and scour profiles which moved in longitudinal and transverse directions on a metal carriage.

The experimental model of GCS is made of PVC installed at a distance of 0.75 meters from the channel's beginning. GCS includes a sloped surface 0.4 meters long with an angle of 20.5 and a rectangular cube 0.5 meters long, 0.15 meters high, and the width equal to the channel width, with two varied slopes of 90° and 60° at the downstream face. Ben Meftah and Mossa (2020) [23] suggested that to ensure the development of the flow, the GCS experimental model should be installed at a distance of one meter from the beginning of the channel. To provide more suitable development of the flow, and reduce its turbulence, a grid screen was used before the water flow inlet in a channel to calm it down. In tests, the water passed through the grid screen, and after 0.75 m reached the GCS, the flow overflowed on the sedimentary bed, and the scour process started.

The downstream face of GCS was filled with two different sand materials with a height of 11.6 centimeters, which continues to the end of the channel with a constant height. Experiments have been conducted on two sand beds with an average diameter of d_{50}=0.8 and d_{50}=1.6 mm, and ρ_s=2650 kg/m^3. To keep these soils safe against washing, at the end of the erodible bed, the end sill is at a height equal to the height of the sedimentary bed. Figure 1 shows the experimental model in the laboratory and a schematic view.

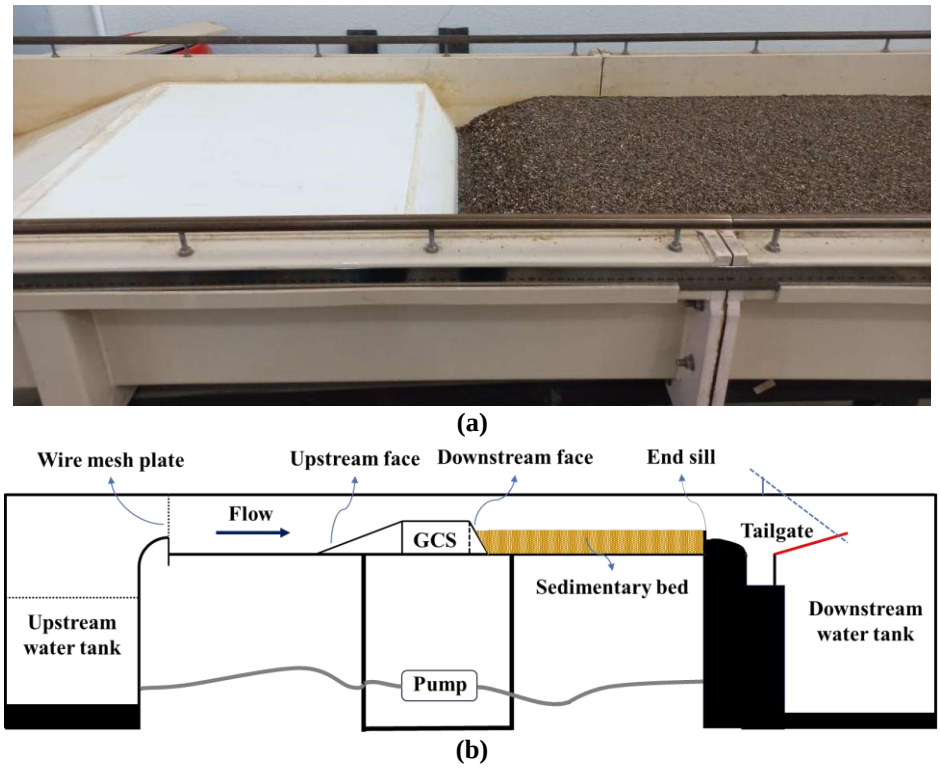


Figure 1. Experimental model in (a) Laboratory (b) Schematic view

The measured values during each test for the scour hole formed downstream of GCS include the maximum equilibrium depth (d_s), the maximum equilibrium length (l_s), the longitudinal profiles of the equilibrium scour hole, critical flow depth (H_c), and tailwater depth (H_t). After finding the location of d_s along the channel's centerline in the longitudinal direction, along the location of d_s, scour depth was measured in the transverse direction of the channel, was to obtain the maximum depth of the final equilibrium scour hole (d_s). Table 1 presents the adjusted values of each test. Experiments were divided into two models based on the grain size of the soil. The first category (model A) consists of soil with d_{50}=0.82 mm, and the second (model B) uses soil with d_{50}=1.6 mm.

Table 1. Experimental setup of each test

Model	Test	q (m^2/s)	λ (°)	H_t (m)	H_c (m)	d_{50} (mm)
A	A1	0.00467	90	0.018	0.0073	0.82
	A2	0.00583	90	0.020	0.0089	0.82
	A3	0.00700	90	0.023	0.0102	0.82
	A4	0.00467	60	0.018	0.0074	0.82
B	B1	0.00467	90	0.018	0.0077	1.60
	B2	0.00583	90	0.020	0.0105	1.60
	B3	0.00700	90	0.023	0.0091	1.60
	B4	0.00467	60	0.018	0.0070	1.60
	B5	0.00583	60	0.020	0.0081	1.60
	B6	0.00700	60	0.023	0.0092	1.60

3. Results and discussion

3.1. Experimental results

To avoid undesirable initial scour in all tests, in the beginning, each test was started with the lowest flow discharge of 0.0013 m^3/s. After the flow passed over the GCS flowed on the sedimentary bed, and reached the end sill, the flow was adjusted to the desired flow discharge. In all tests, the maximum depth of the scour hole downstream of GCS and its maximum length were measured and shown in Table 2.

Table 2. Maximum scour depth and length of each test

Model	Test	Fr_d	d_s (m)	l_s (m)
A	A1	5.55	0.0924	0.290
	A2	5.69	0.1096	0.335
	A3	5.96	0.0740	0.455
	A4	5.47	0.0998	0.270
B	B1	3.77	0.0477	0.205
	B2	3.98	0.0666	0.245
	B3	4.14	0.0369	0.355
	B4	4.14	0.0750	0.190
	B5	4.48	0.0822	0.230
	B6	4.73	0.0898	0.240

One of the most critical issues in the discussion of scour in the laboratory is determining the equilibrium time of the scour process. The equilibrium scour time is when the geometry of the scour hole does not vary after that. In other words, the sediment bed particles are not separated from the scour hole by the water flow. A crucial factor in determining the equilibrium scour time is the type of soil granulation. It is clear that the larger the laboratory scale and the coarser soil granularity, the more time is needed to reach the equilibrium scour hole. In 2018, Wang et al. [33] investigated the bed morphology downstream of GCS with a larger laboratory scale and coarser soil granularity than this research. They considered the equilibrium scour time in their studies to be 120 minutes, and according to their observations, during this time, the scour hole reached an equilibrium state. The equilibrium scour time in Rajaei et al. [13] in 2018 was about 270 minutes. At three times, 5, 30, and 270 minutes, the values of changes in the geometry of the longitudinal scour profile downstream of the GCS were investigated. The ratio of equilibrium time in their research is as follows: $\frac{t}{t_e}$= 0.013 for 5 minutes, $\frac{t}{t_e}$= 0.083 for 60 minutes, and $\frac{t}{t_e}$= 0.75 for 270 minutes. Where t represents time and t_e represents equilibrium time. According to Breusers and Raudkivi [34], sometimes the scour time is so long that it may never be achieved. Of course, sometimes the scour time is so short that it can be less than 60 minutes. For example, Pagliara and Palermo [11] observed that only in 40 minutes, the scour hole reaches its equilibrium state.

There were a lot of disagreements regarding the equilibrium scour time, then a 360-minute test was performed at first. In the first 10 minutes, it was found that the scour hole developed quickly. Then, the expansion rate of the scour hole starts to reduce. At 90 minutes after the start of the scour process, the geometry of the scour hole was very close to its equilibrium state. After about 240 minutes, the sediment bed particles were hardly separated from the water flow from the scour hole and even returned to the hole due to hydraulic jump and backward flow. As a result, 240 minutes was chosen as the final and equilibrium scour time for all experiments.

3.2. Longitudinal profile of scour hole downstream of GCS

The proper process of forming the geometry of the scour hole is fundamental in obtaining d_s and l_s. Several studies, such as Bormann and Julien (1991) [6], Mossa (1998) [7], and Ben Meftah and Mossa (2020) [23], previously showed that the most significant effect on the final geometry of the longitudinal profile of the scour hole depends on the scour process time, flow intensity, depth of tailwater, particle Froude number, type of soil granularity, water drop, flow depth of flow on the end of the GCS crest and the slope of the downstream face of GCS. For example, one of the equations that shows the relationship between these parameters is Eq. (6) and Eq. (7). In most of the experiments of this research, the longitudinal profile of the equilibrium scour hole was spoon-shaped. Figure 2 presents the longitudinal patterns of the scour hole in the equilibrium state for tests A1, A2, B1, and B2.

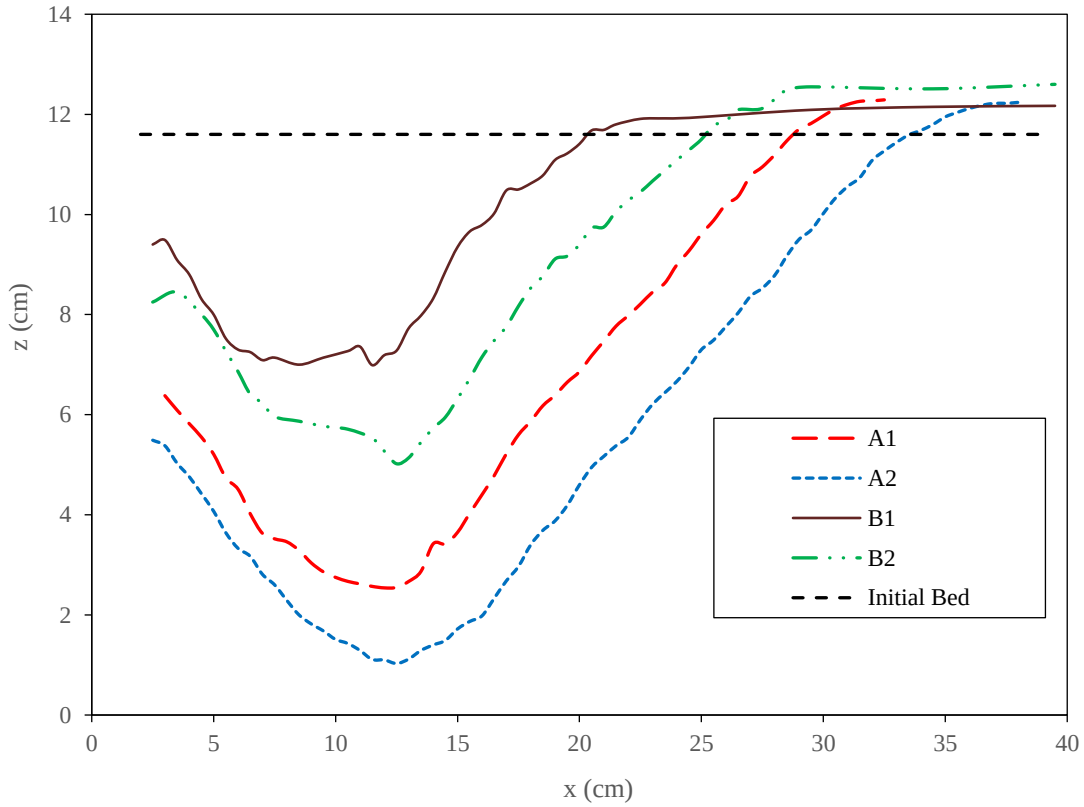


Figure 2. Longitudinal profile of the scour hole in tests A1, A2, B1, and B2

3.3. Influence of sediment size on d_s and l_s

Experimental observations indicated that under the constant flow discharge and geometry of GCS and different soil granularity, the maximum length and depth of the scour hole decreased by increasing the sediment size. As shown in Table 2, increasing the flow discharge in both types of soil, increases l_s. Figure 3 compares d_s and l_s downstream of the vertical GCS in different sediment sizes.

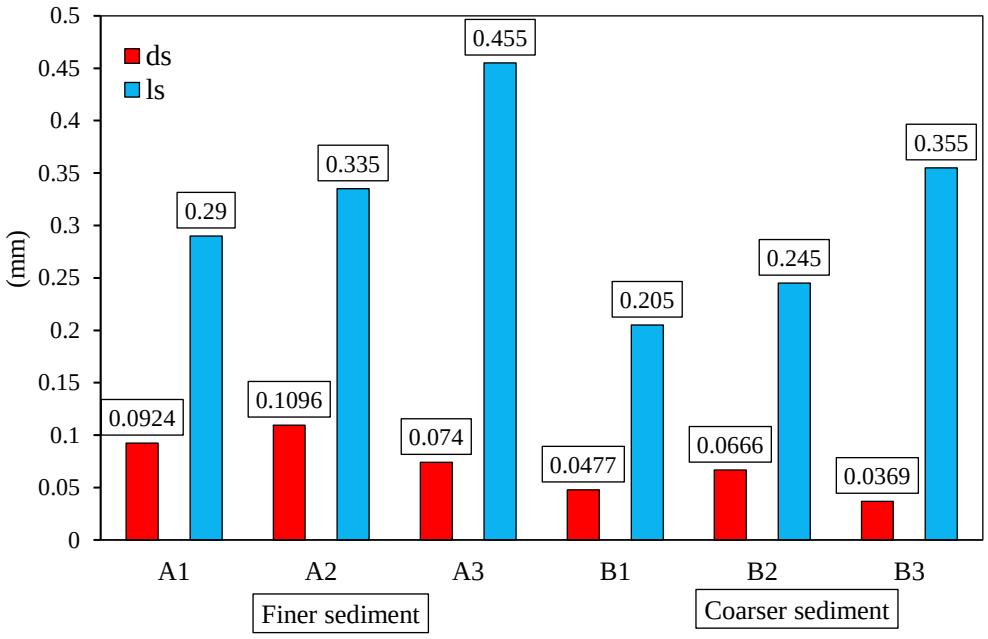


Figure 3. Comparison of d_s and l_s downstream of the vertical GCS with different sediment sizes

Although in tests A3 and B3, q=0.007 m^2/s (more than in other tests), d_s in test A3 is lower than A1 and A2, as well as d_s in test B3 was lower than in tests B2 and B3. This result occurs because in this case, the Froude number is higher than one, which leads to the formation of hydraulic jump and return flow. The hydraulic jump is often formed on the scour hole near the bed sediment. Already, Chanson [35] has mentioned this issue. This phenomenon, a type of reverse flow, leads to the return of sediment particles into the scour hole. Figure 4 shows the hydraulic jump formed downstream of GCS with the vertical face on the scour hole.

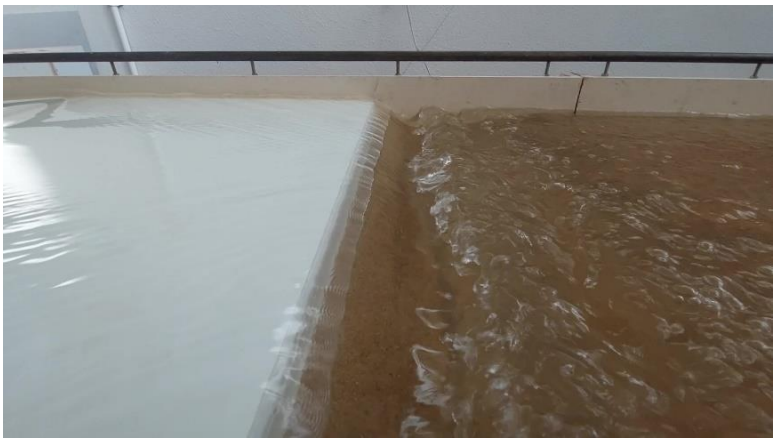


Figure 4. Hydraulic jump formed downstream of GCS

As mentioned in the technical literature, increasing the flow velocity leads to more erosion of the sedimentary bed. In all tests, it was observed that the increase in the flow discharge increased l_s. The accuracy of this conclusion has already been declared in the study of Ben Meftah and Mossa (2020) [23].

3.4. Influence of the slope of GCS downstream face on d_s and l_s

The comparison between vertical and inclined GCS has already been studied, such as Bormann and Julien (1991) [6] and Ben Meftah and Mossa (2020) [23]. These studies indicated that under the same hydraulic conditions, d_s and l_s changed with the variations of the slope of the downstream face of GCS. As the slope decreases from 90° in different hydraulic conditions, d_s, and l_s increase or decrease. In this research, in the sedimentary bed with d_{50}=1.6 mm, under constant hydraulic conditions, d_s downstream of GCS with an angle of 60° is more than 90°, in comparison l_s downstream of GCS with the face of 60° became less than 90°. Figure 5 indicates d_s and l_s downstream of the vertical and inclined GCS in the constant sediment sizes.

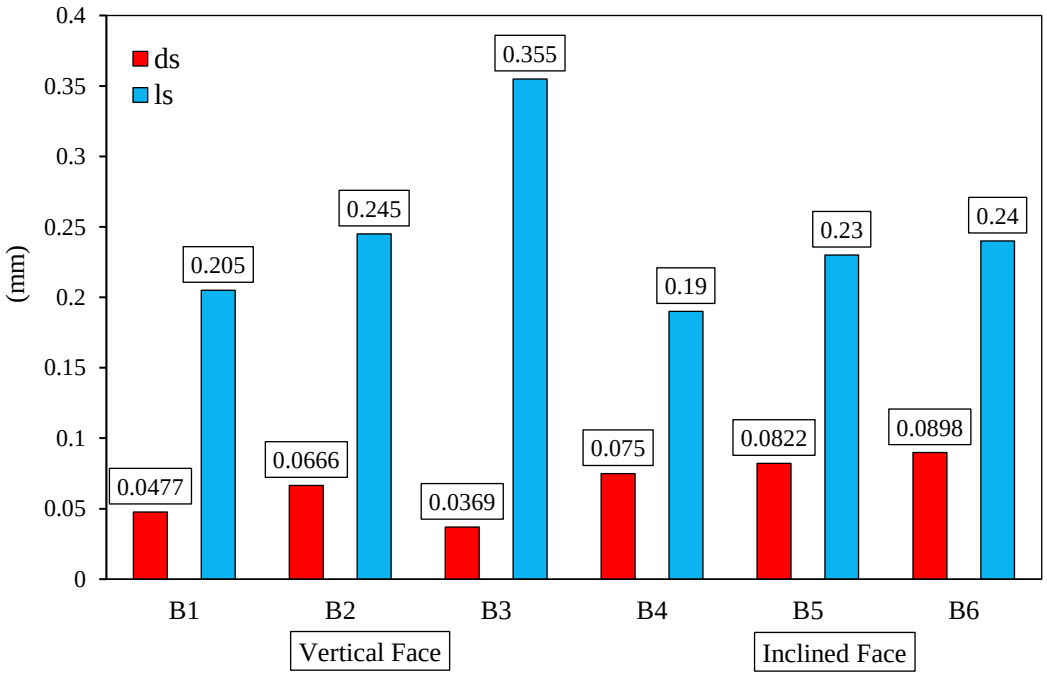


Figure 5. Comparison of d_s and l_s downstream of the inclined and vertical GCS with the constant sediment sizes

Test A4 was performed under q=0.004667 m^2/s, λ=60° and d_{50}=0.82 mm. Although this test was conducted in the same sedimentary conditions and different geometrical conditions from test A1, in terms of the geometry of GCS it was similar to test B1 and different in terms of sediment sizes. For this reason, the data obtained from test A4 are compared and analyzed with tests A1 and B1, respectively. Investigations showed that although d_s in test A4 was greater than in test A1, l_s was reduced. It can be concluded that under the same sedimentary condition, by decreasing the slope of the GCS downstream face from 90° to 60°, d_s increases, and l_s decreases. Also, in similar geometrical conditions, i.e. downstream face of 60° degrees and different sedimentary conditions, as expected, the coarser sediment, d_s, and l_s decreases.

3.5. Discussion

Accurate prediction of the d_s is always one of the biggest problems in river engineering. In the meantime, researchers presented a series of predictive experimental equations previously mentioned in the technical literature. The data collected from d_s in the present study is displayed in a dimensionless form in Table 3.

Table 3. The dimensionless values of d_s/H_c based on Fr_d changes

Model	Test	Fr_d	d_s/H_c
A	A1	5.55	12.66
	A2	5.69	12.31
	A3	5.96	7.25
	A4	5.47	13.49
B	B1	3.77	6.19
	B2	3.98	7.32
	B3	4.14	3.51
	B4	4.14	10.71
	B5	4.48	10.15
	B6	4.73	9.76

In Figure 6, d_s/H_c was compared between the present study and Ben Meftah and Mossa (2020) [23]. Statistical index calculations revealed a correlation coefficient (R^2=0.891) and relative error (RE%=10.66%). These values present acceptable differences between the present study results and previous data.

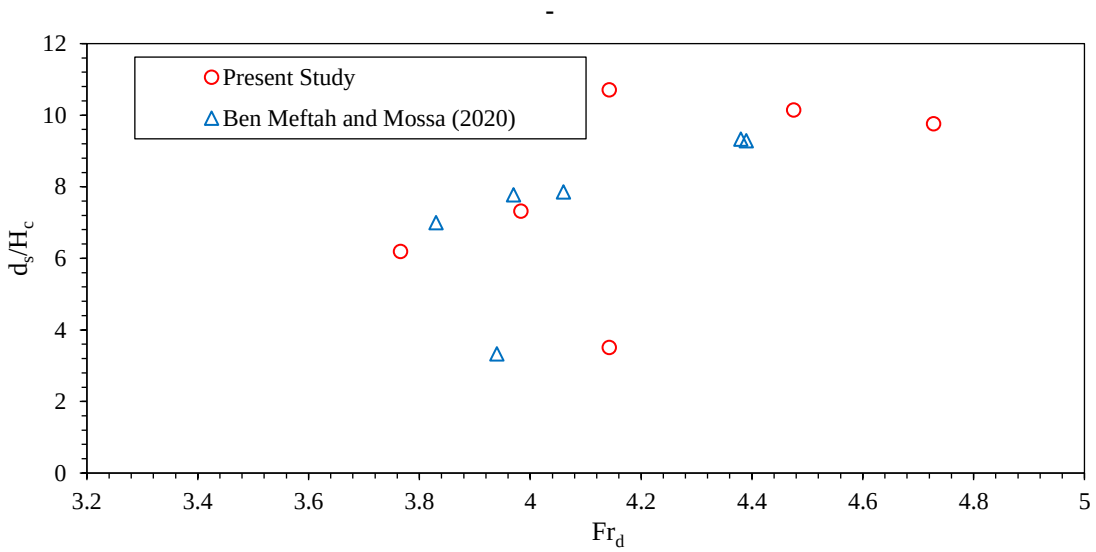


Figure 6. Comparison of d_s/H_c between the present study and Ben Meftah and Mossa (2020)

In the same geometric conditions of the experimental model, it was observed that for finer sediments, the maximum length and depth of the scour hole increases compared to the coarser sediment condition. This is obvious because, in finer sediment conditions, sediment particles could be moved up more easily. The settling velocity of sediment is a function of particle diameter. In larger particles, the rate of sedimentation will increase. Chanson [35] mentioned that bed-load transport occurs when the bed shear stress is larger than a critical value.

In the constant sedimentary conditions and different GCS geometries, it was observed for GCS with the downstream vertical face, d_s decreases, and by changing the slope from 90° to 60°, d_s increases. In reverse, l_s in GCS with a slope of 60° reduced compared to GCS with a slope of 90°. It can be concluded that in the vertical slope, the longitudinal profile of the scour hole is stretched along the longitudinal axis, and its depth is reduced. Results of tests A3 and B3 indicated that despite the highest discharge, the maximum scour depth became less. This result was obtained due to the formation of anti-dune downstream of GCS in these cases.

4. Conclusion

Grade control structures (GCS) are countermeasures to reduce river erosion. Since scouring downstream of these structures leads to their failure and damage, it is necessary to study scouring downstream of GCS. This research investigated the downstream morphology of GCS with inclined and vertical downstream faces in the river under different hydraulic and sedimentary beds, and the effect of each effective parameter was evaluated. It was shown that in the same GCS geometry and finer-grained sedimentary conditions, the values of scouring were larger than in coarser-grained conditions. This is obvious because, in finer-grained conditions, it is more possible for particles to be suspended and moved with water flow. A comparison was made in the same sediment conditions and different geometries, and the results showed that when the downstream face of GCS is vertical, d_s is less than when it is inclined. While the maximum scour lengths obtained in vertical faces were more than in inclined conditions. It was also concluded that the hydraulic jump significantly influences the final geometry of the equilibrium scour hole due to the returning flow it creates. Although the flow discharges were highest in some tests, the maximum scour depth was lower, and an antidune was formed downstream of GCS because the Froude number became higher than 1. It was concluded that in the same sediment conditions, by reducing the slope of the downstream face of GCS from 90° to 60°, d_s increases, and l_s decreases. Also, in the same geometry and different sediments, in coarser-grained conditions, the values of scour decreases. The results of this study could be used as a small-scale experimental model to distinguish the geometry of GCS on scour parameters, but flow characteristics in scour holes were not investigated. It is recommended to conduct other studies to evaluate the influence of the secondary current on the location of the maximum depth of the scour hole. Also, the effect of the roughness of GCS on the scour hole profiles and flow characteristics can be investigated.

Acknowledgements

The authors appreciate Mr. Ali Mahdian Khalili, the executive officer and senior researcher of the hydraulic lab at Babol Noshirvani University of Technology, for his worthy help in performing this research.

References

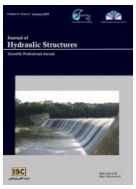
1. Mahdian Khalili A, Hamidi M, (2023). Time evolution effect on the scour characteristics downstream of the sluice gate with the submerged hydraulic jump in a laboratory model. Journal of Hydraulic Structures 9(2), pp: 32-47. https://doi.org/10.22055/JHS.2023.43499.1249.
2. Sattar AM, Plesiński K, Radecki-Pawlik A, Gharabaghi B. (2018). Scour depth model for grade-control structures. Journal of Hydroinformatics 20(1), pp: 117-133. https://doi.org/10.2166/hydro.2017.149
3. Korpak J, Lenar-Matyas A, Radecki-Pawlik A, Plesiński K, (2021). Erosion irregularities resulting from series of grade control structures: The Mszanka River, Western Carpathians. Science of The Total Environment 799, 149469. https://doi.org/10.1016/j.scitotenv.2021.149469
4. Khalili AM, Hamidi M, Dadamahalleh PA, (2023). Introducing Countermeasures for Reducing Bed Scour of Mountainous Rivers, 1st International Conference on Sustainable Mountain, 11&12 December 2023, University of Mohaghegh Ardabili.
5. Shafai-Bejestan M, Nabavi SMR, Dey S, (2016). Scour downstream of grade control structures under the influence of upward seepage. Acta Geophysica, 64, pp: 694-710. https://doi.org/10.1515/acgeo-2016-0024
6. Bormann NE, Julien PY, (1991). Scour downstream of grade-control structures. Journal of Hydraulic Engineering 117(5), pp: 579-594. https://doi.org/10.1061/(ASCE)0733-9429(1991)117:5(579)
7. Mossa M, (1998). Experimental study on the scour downstream of grade-control structures. Proc., 26th Convegno di Idraulica e Costruzioni Idrauliche, pp: 581-594.
8. Lenzi MA, Marion A, Comiti F, (2003). Local scouring at grade-control structures in alluvial mountain rivers. Water Resources Research 39(7). https://doi.org/10.1029/2002WR001815
9. Marion A, Lenzi MA, Comiti F, (2004). Effect of sill spacing and sediment size grading on scouring at grade-control structures. Earth Surface Processes and Landforms: The Journal of the British Geomorphological Research Group, 29(8), pp: 983-993. https://doi.org/10.1002/esp.1081
10. D'Agostino V, Ferro V, (2004). Scour on alluvial bed downstream of grade-control structures. Journal of Hydraulic Engineering 130(1), pp: 24-37. https://doi.org/10.1061/(ASCE)0733-9429(2004)130:1(24)
11. Pagliara, S., & Palermo, M. (2013). Rock grade control structures and stepped gabion weirs: Scour analysis and flow features. Acta Geophysica 61, pp: 126-150. https://doi.org/10.2478/s11600-012-0066-0
12. Pagliara S, Kurdistani SM, (2014). Scour characteristics downstream of grade-control structures. River flow 2014, pp: 2093-2098.
13. Rajaei A, Esmaeili Varaki M, Shafei Sabet B, (2020). Experimental investigation on local scour at the downstream of grade control structures with labyrinth planform. ISH Journal of Hydraulic Engineering 26(4), pp: 457-467. https://doi.org/10.1080/09715010.2018.1502627
14. Di Nardi J, Palermo M, Bombardelli FA, Pagliara S, (2021). The phenomenological theory of turbulence and the scour evolution downstream of grade-control structures under steady discharges. Water 13(17), 2359. https://doi.org/10.3390/w13172359
15. Sohrabzadeh H, Ghodsian M, (2022). Experimental study of the effect of sidewall slope over the triangular PK weir. Journal of Hydraulics, 17(4), 17-30. https://doi.org/10.30482/JHYD.2022.326177.1581

16. Sohrabzadeh Anzani H, Ghodsian M, (2024). Experimental study of flow over piano key weirs with different plan shapes. ISH Journal of Hydraulic Engineering 30(2), 185-195. https://doi.org/10.1080/09715010.2024.2302808
17. Lantz WD, Crookston BM, Palermo M, (2022). Evolution of local scour downstream of Type A PK weir in non-cohesive sediments. Journal of Hydrology and Hydromechanics 70(1), pp: 103-113. https://doi.org/10.2478/johh-2021-0035
18. Khalili AM, Hamidi M, (2023). Experimental investigation of submerged hydraulic jump downstream of sluice gate in erodible channel. Proc. of the 13th International Congress on Civil Engineering, Tehran.
19. Guguloth S, Pandey M, (2023). Accuracy evaluation of scour depth equations under the submerged vertical jet. AQUA—Water Infrastructure, Ecosystems and Society 72(4), pp: 557-575. https://doi.org/10.2166/aqua.2023.015
20. Guguloth S, Pandey M, Pal, (2024). Application of Hybrid AI Models for Accurate Prediction of Scour Depths under Submerged Circular Vertical Jet. Journal of Hydrologic Engineering 29(3), 04024010. https://doi.org/10.1061/JHYEFF.HEENG-6149
21. Ben Meftah M, De Padova D, De Serio F, Mossa M, (2021). Secondary currents with scour hole at grade control structures. Water 13(3), 319. https://doi.org/10.3390/w13030319
22. Noormohammadi G, Esmaeili Varaki M, Radice A, Shafiee Sabet B, (2018). Experimental Investigation on Local Scour at Downstream of the Inclined Grade Control Structure. Irrigation and Drainage Structures Engineering Research 19(72), pp: 51-68. https://doi.org/10.22092/idser.2017.114767.1239
23. Ben Meftah M, Mossa M, (2020). New approach to predicting local scour downstream of grade-control structure. Journal of Hydraulic Engineering 146(2), 04019058. https://doi.org/10.1061/(ASCE)HY.1943-7900.0001649
24. Mason PJ, Arumugam K, (1985). Free jet scour below dams and flip buckets. Journal of Hydraulic Engineering 111(2), pp: 220-235. https://doi.org/10.1061/(ASCE)0733-9429(1985)111:2(220)
25. Koohsari A, Hamidi M, (2021). Experimental study of the effect of mining materials downstream of bridge pier on scour profile with optimizing distance approach. Journal of Water and Soil Conservations, 28(3), pp: 1-26. https://doi.org/10.22069/JWSC.2022.19400.3490.
26. Akbari Dadamahalleh P, Hamidi M, Mahdian Khalili A, (2022). Experimental Prediction of the Bed Profile with the Full-submerged and Semi-submerged Debris Accumulation Upstream of the Cylindrical Bridge Pier. Journal of Water and Soil Conservation, 29(4), pp: 95-114. https://doi.org/10.22069/JWSC.2023.20642.3582.
27. Mahdian Khalili A, Hamidi M, Akbari Dadamahalleh P, (2023). Scour Morphology around the Bridge Pier with Upstream Rectangular Debris. 22nd Iranian Conference on Hydraulics, 8-9 November 2023, University of Maragheh.
28. Hamidi M, Sadeqlu M, Khalili AM, (2024). Investigating the design and arrangement of dual submerged vanes as mitigation countermeasure of bridge pier scour depth using a numerical approach. Ocean Engineering 299, 117270. https://doi.org/10.1016/j.oceaneng.2024.117270
29. Mahdian Khalili A, Akbari Dadamahalleh P, Hamidi M, (2024). Experimental evaluation of dune formation downstream of pier scour hole with upstream debris accumulation. Journal of Hydraulic Structures 10(1), pp: 13-28. https://doi.org/10.22055/JHS.2024.45772.1281
30. Dadamahalleh PA, Hamidi M, Khalili AM (2024) Bed sill effect on bridge pier scour with debris obstruction: an experimental investigation. Innovative Infrastructure Solutions 9(5),

pp: 142. https://doi.org/10.1007/s41062-024-01447-z
31. Khalili AM, Hamidi M, Dadamahalleh, PA (2024). Experimental study of the effect of rectangular debris blockage on the scour hole development around a cylindrical bridge pier. Water Practice & Technology 19(5), pp: 1878-1892. https://doi.org/10.2166/wpt.2024.092
32. Hamidi M, Koohsari A, Khalili AM (2024). Numerical investigation of mining pit effects on maximum scour depth around bridge pier with different shape. Modeling Earth Systems and Environment, 1-15. https://doi.org/10.1007/s40808-024-02057-5
33. Wang JM, Yang XG, Zhou HW, Lin X, Jiang R, Lv EQ, (2018). Bed Morphology around various solid and flexible grade control structures in an unstable gravel-bed river. Water 10(7), 822. https://doi.org/10.3390/w10070822
34. Breusers NHC, Raudkivi AJ, (1991). Hydraulic structure design manual: scouring. IAHR design manual, 2.
35. Chanson H, (2004). Hydraulics of open channel flow. Elsevier.

© 2024 by the authors. Licensee SCU, Ahvaz, Iran. This article is an open access article distributed under the terms and conditions of the Creative Commons Attribution 4.0 International (CC BY 4.0 license) (http://creativecommons.org/licenses/by/4.0/).

Journal of Hydraulic Structures
J. Hydraul. Struct., 2024; 10(4):61-81
DOI: 10.22055/jhs.2024.44298.1260



OPEN ACCESS

A Prediction of Manning's n_r in Compound Channels with Converged and Diverged Floodplains using GMDH Model

Sajad Bijanvand [1]
Mirali Mohammadi [2]
Abbas Parsaie [3]

Abstract

In the study of natural waterways, the use of formulas such as Manning's equation is prevalent for analyzing flow structure characteristics. Typically, floodplains exhibit greater roughness compared to the main river channel, which results in higher flow velocities within the main channel. This difference in velocity can lead to increased sedimentation potential within the floodplains. Therefore, accurately determining Manning's roughness coefficient for compound channels, particularly during flood events, is of significant interest to researchers. This study aims to model the Manning roughness coefficient in compound channels with both converging and diverging floodplains using advanced soft computing techniques. These techniques include a multi-layer artificial neural network (MLPNN), Group Method of Data Handling (GMDH), and the Neuro-Fuzzy Group Method of Data Handling (NF-GMDH). For the analysis, a dataset from 196 laboratory experiments was used, which was divided into training and testing subsets. Input variables included parameters such as longitudinal slope (S_o), relative hydraulic radius (R_r), relative depth (D_r), relative dimension of flow aspects (δ^*), and the convergent or divergent angle (θ) of the floodplain. The relative Manning roughness coefficient (n_r) was the output variable of interest. The results of the study showed that all the models performed well, with the MLPNN model achieving the highest accuracy, characterized by R^2 = 0.99, *RMSE* = 0.001, *SI* = 0.0015, and *DDR* = 0.0233 during the testing phase. Further analysis of the soft computing models indicated that the most critical parameters influencing the results were S_o, R_r, D_r, δ^*, and θ. These findings highlight the effectiveness of soft computing techniques in accurately modeling the Manning roughness coefficient in complex channel conditions and provide valuable insights for future research and practical applications in the management of flood events and waterway analysis.

Keywords: Compound Channel, Non-Prismatic Floodplain, relative Manning's roughness, NF-GMDH.
Received: 15 July 2023; Accepted: 12 August 2024

[1] Department of Civil Engineering, Faculty of Engineering, Imam Ali University, Tehran, Iran.
[2] Department of Civil Eng., Faculty of Engineering, Urmia University, Urmia, Iran. Email: m.mohammadi@urmia.ac.ir **(Corresponding author)**
[3] Department of Hydraulic Structures, Faculty of Water and Environmental Engineering, Shahid Chamran University of Ahvaz, Ahvaz, Iran.

Notation

n_r	Relative Manning's Roughness Coefficient
GMDH	Group Method of Data Handling
NF-GMDH	Neuro-Fuzzy Group Method of Data Handling
MLPNN	Multilayer Perceptron Neural Networks
D_r	relative flow depth
R_r	relative hydraulic radius
δ^*	relative dimension of the flow aspects
θ	angle of divergence and convergence of the section
S_o	longitudinal slope
R^2	Coefficient of Determination
DDR	Developed Discrepancy Ratio
RMSE	Root mean square error

1. Introduction

1.1. Background and Significance of Compound Channel Analysis

One of the central topics in hydraulic engineering has consistently been the analysis of river flow characteristics. As rivers traverse various terrains, including flat plains and mountainous regions, their cross-sectional profiles undergo significant changes [1]. Typically, rivers experience unsteady flow conditions. Furthermore, floods contribute to irregular and non-uniform flow patterns. These challenges are compounded by the meandering nature of rivers, particularly in plains where numerous bends are present. In contemporary river hydraulic modeling, the compound channel approach is employed, considering both the floodplain and the main channel [2]. Notably, the floodplain generally exhibits a lower flow velocity compared to the main channel, resulting in sediment deposition that increases the roughness of the floodplain relative to the main channel [3]. The most common metric for describing river discharge is the water level flowing through the river. A key component of river flow studies is the accurate prediction of discharge. During flooding events, rivers may overflow their banks, causing damage to areas beyond the floodplain. Precise discharge capacity calculations are essential for the construction, management, and maintenance of open channels, as well as for flood prediction efforts [2]. Consequently, techniques for accurately determining the discharge capacity of channels are vital for effective flood control. Accurate discharge predictions for open channels necessitate reliable roughness coefficient estimates. The Manning, Chezy, and Darcy-Weisbach equations are traditionally used to estimate discharge in uniform flow conditions within simple, non-prismatic compound channels. These methods were originally developed for basic channels to ascertain the roughness coefficient of the bed material [4]. However, in non-prismatic channels, bed roughness, geometric configurations, and hydraulic properties significantly influence the roughness coefficients. Therefore, a model to predict roughness coefficients is derived by incorporating these variables [2].

In open channel flow, Manning's formula is the most widely used approach due to its simplicity and practicality. Manning's formula, however, must be used with appropriate caution when applied to non-uniform compound channels. To accurately represent the boundary's real or effective variation, as Yen [5] proposed for simple uniform flows, Manning's n is considered a roughness factor that quantifies the roughness in terms of a geometric measure. The calculation of the roughness coefficient in compound channels is complicated by various hydraulic factors. Numerous techniques exist for determining a channel's roughness coefficient, including using

tables, photographs, and mathematical formulas. While traditional methods may provide satisfactory results for simple channels, they often fail for more complex sections, particularly non-prismatic compound channels. As a result, there is a growing preference for soft computing methods to calculate Manning's coefficient due to their ability to handle complex hydraulic conditions [6].

1.2. Advances in Soft Computing Techniques

Researchers are increasingly turning to soft computing methods to model and estimate hydraulic flow parameters, especially in compound open channels with non-prismatic floodplains, because of the limited accuracy of numerical models and conventional techniques [7–11]. The complexity of non-prismatic channels requires sophisticated models to predict flow characteristics accurately. In compound channels with prismatic floodplains, various advanced methods have been employed to predict flow discharge. These include artificial neural networks [2], which simulate the flow dynamics based on learning from data, and fuzzy adaptive neural network models [12,13], which incorporate fuzzy logic to handle uncertainties in the flow parameters. Additionally, multivariate adaptive regression splines (MARS) [14] provide a flexible modeling approach that captures nonlinear relationships in the data, and gene expression programming [15], a type of evolutionary algorithm, has been used to develop predictive models based on natural selection principles. The MARS model, in particular, has been effectively utilized to predict discharge in meandering open channels [16], demonstrating its capability to manage complex flow patterns.

1.3. Gap in Research and Study Objective

Despite these advancements, there is a noticeable gap in research regarding the estimation of Manning's roughness coefficient in non-prismatic compound channels with converging and diverging floodplains using soft computing methods. The unique hydraulic characteristics of these channels, including variations in cross-sectional geometry and flow patterns, pose significant challenges for traditional modeling approaches. Therefore, this study focuses on developing advanced soft computing models, specifically Group Method of Data Handling (GMDH), Neuro-Fuzzy GMDH (NF-GMDH), and Multi-Layer Perceptron Neural Networks (MLPNN), to estimate the relative Manning's roughness coefficient (nr) in such channels. These models are designed to capture the complex interactions between hydraulic and geometric parameters, providing more accurate and reliable estimates of roughness coefficients. The GMDH algorithm is a self-organizing method that constructs models by iteratively selecting the best combination of input variables, making it well-suited for handling complex datasets. The NF-GMDH model combines the strengths of fuzzy logic and GMDH, enabling it to manage uncertainty and imprecision in the data while constructing accurate predictive models. MLPNN, a type of artificial neural network, consists of multiple layers of interconnected neurons that learn to represent the underlying patterns in the data through training. By leveraging these advanced soft computing techniques, the study aims to address the limitations of traditional methods and provide a robust framework for predicting Manning's roughness coefficient in non-prismatic compound channels. The development and validation of these models involve comprehensive data collection and analysis, ensuring that the models are capable of generalizing across different hydraulic conditions and channel configurations. This research not only contributes to the field of hydraulic engineering by enhancing the accuracy of flow predictions but also supports flood management and channel design by providing reliable tools for estimating channel roughness under complex flow conditions.

1.4. Contribution to the Field

This study introduces the application of advanced soft computing models, including GMDH, NF-GMDH, and MLPNN, for predicting Manning's roughness coefficient in complex compound channels with converging and diverging floodplains. While previous research has primarily focused on simpler or prismatic channels, this work addresses the challenges presented by non-prismatic geometries. By leveraging these advanced models, the accuracy and reliability of roughness coefficient predictions in such channels can be significantly enhanced. This research contributes to the field by providing a novel methodological framework that can be utilized for improved flood management and channel design, thus advancing the current understanding and capabilities in hydraulic engineering.

2. Materials and Methods

The dataset employed for estimating the nr using soft computing models comprises 196 experimental data sets that focus on converging and diverging compound channels. These data sets have been gathered from several published papers, specifically those authored by Bousmar [17], Bousmar et al. [18], Rezaei [19], Yonesi et al. [20], and Naik and Khatua [21]. This collection of data, which is summarized in Table (1), was compiled by Das et al. The discussion in this section covers several key aspects: it outlines the significant parameters, details both the input and output variables, and provides a comprehensive overview of the soft computing models that have been utilized. Furthermore, it delves into the modeling strategies that were employed as well as the criteria used for evaluation. An illustrative view of the non-prismatic compound channel with various converging geometries is provided in Figure (1).

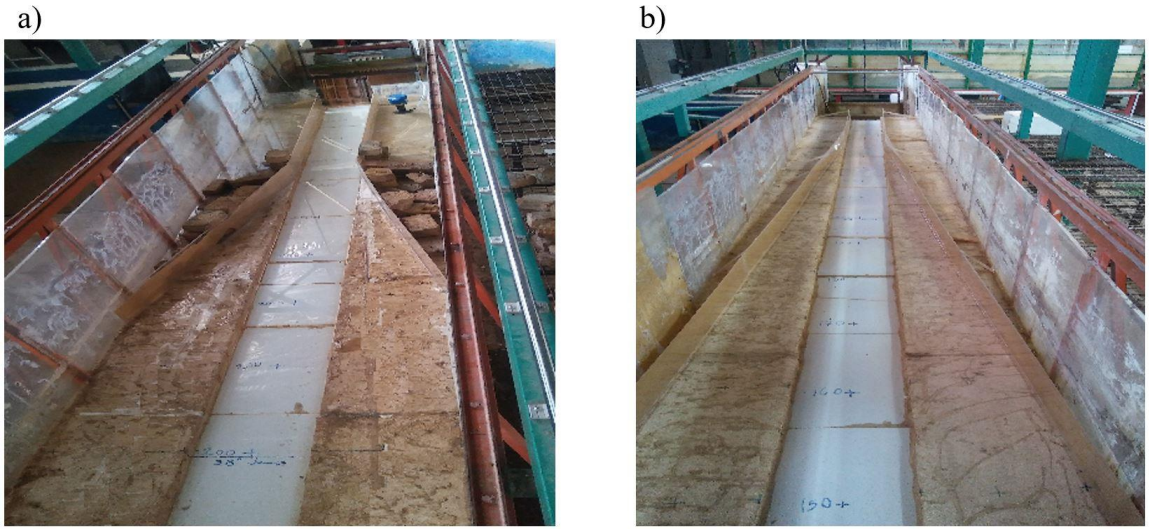


Figure 1. A view of the compound channel with non-prismatic floodplains a) θ =11.3° and b) θ = 3.8° [22]

The Manning roughness coefficient in this study is determined through the analysis of five critical input parameters:

1. **Longitudinal slope (S_o)**: This represents the gradient of the channel along its length.
2. **Relative Hydraulic radius (R_r)**: This is the ratio of the hydraulic radius to a reference value.
3. **Relative flow depth (D_r)**: This denotes the ratio of the flow depth to a reference depth.
4. **Relative dimension of the flow aspects (δ^*)**: This parameter reflects the proportion of certain flow characteristics relative to a reference dimension.
5. **Convergence or divergence angle (θ)**: This measures the angle of the floodplain, with a positive sign indicating a convergence angle and a negative sign indicating a divergence angle.

By analyzing these parameters, the research aims to accurately determine the Manning roughness coefficient, which is crucial for understanding and modeling flow behavior in compound channels.

Through the careful analysis of these parameters, this research endeavors to precisely determine the Manning roughness coefficient. This coefficient is essential for comprehending and accurately modeling the flow behavior in compound channels. The research focuses on the relative Manning roughness coefficient of the flow, denoted as n_r, which was selected as the primary output variable. This coefficient n_r is defined as the ratio of the Manning roughness coefficient in the main channel (n_{mc}) to the Manning roughness coefficient in the floodplain (n_{fp}). Mathematically, this relationship is expressed as $n_r = \frac{n_{mc}}{n_{fp}}$. The aforementioned parameters can be encapsulated within a functional relationship, which is articulated in Eq. (1).

$$n_r = f\left(S_0, R_r, D_r, \delta^*, \theta\right) \tag{1}$$

Table 1 provides a comprehensive summary of the statistical analysis conducted on the various parameters that were employed to determine the relative Manning roughness coefficient within compound channels. These channels are characterized by floodplains that either converge or diverge. The analysis meticulously examines each parameter's influence and how they collectively contribute to the accurate calculation of the roughness coefficient, offering a detailed insight into the hydraulic behavior of such complex channel systems.

Table 1- Range of collected data set and Statistical analysis of parameters involved in determining n_r

Source	*Range*	S_0*10^{-3}	R_r	D_r	δ^*	θ	n_r
Rezaei [15]	max	2.003	4.590	0.522	6.540	-3.81	0.830
	min		0.869	0.114	0.905		0.070
	st div		1.219	0.143	1.940		0.278
	avg		2.505	0.305	4.313		0.591
	median		2.610	0.348	5.150		0.719
Bousmar [13]	max	0.9	4.400	0.538	6.360	-11.3 -3.81	0.837
	min		0.591	0.101	0.808		0.059
	st div		1.185	0.161	1.831		0.295
	avg		2.248	0.345	3.980		0.605
	median		2.392	0.416	4.585		0.747
Bousmar et al [14]	max	0.9	4.200	0.539	6.290	5.71 3.81	0.832
	min		0.561	0.102	0.819		0.052
	st div		1.187	0.152	1.926		0.289
	avg		2.361	0.321	4.166		0.592
	median		2.663	0.347	4.931		0.722
Yonesi et al [16]	max	0.88	35.090	0.364	1.900	11.31 3.81	0.806
	min		1.910	0.103	0.229		0.143
	st div		10.046	0.096	0.622		0.236
	avg		10.192	0.224	1.373		0.482
	median		6.600	0.252	1.656		0.552
Naik & Khatua [17]	max	1.1	7.260	0.325	4.450	-13.38 -5	0.716
	min		0.850	0.059	0.293		0.047
	st div		1.849	0.094	1.489		0.248
	avg		3.604	0.199	3.138		0.519
	median		3.595	0.227	3.795		0.634

2.1. Soft Computing Techniques

2.1.1. Group Method of Data Handling (GMDH)

The GMDH (Group Method of Data Handling) model, originally developed by Ivakhnenko [23] in the 1960s, has since been widely applied and refined in various fields, including hydraulic engineering. This model's ability to construct self-organizing networks makes it particularly suitable for handling complex datasets. The GMDH model is a sophisticated type of neural network that includes an input layer consisting of various variables and parameters, several intermediate layers, and an output layer. This model improves the precision of forecasting physical phenomena by incorporating optimization methods and approximation techniques into its framework. The connections between a system's input and output parameters in this neural network can be described through Volterra function series, which are similar to the discretized polynomial proposed by Kolmogorov-Gabor, as illustrated in the subsequent equation.

$$y = a_0 + \sum_{i=1}^{m} a_i x_i + \sum_{i=1}^{m}\sum_{j=1}^{m} a_{ijk} x_i x_j + \sum_{i=1}^{m}\sum_{j=1}^{m}\sum_{k=1}^{m} a_{ijk} x_i x_j x_k + \cdots \quad (2)$$

where x_0, x_1, x_2, …, x_m is input vectors, and a_0, a_1, a_2, …, a_m is the vector of weight coefficients. In the GMDH structure, every neuron requires at least two inputs. The relationship between the variables influencing both input and output in each neuron is represented by a stimulus function, which can be linear or non-linear. The fundamental structure of the GMDH model is represented by the following formula involving quadratic polynomials with two input variables [24].

$$y = w_0 + w_1 x_1 + w_2 x_2 + w_3 x_1^2 + w_4 x_2^2 + w_5 x_1 x_2 \quad (3)$$

Where in $w_0, w_1, \cdots, w_5$ coefficients are polynomials. To construct the GMDH network, begin by considering binary combinations of the input parameters. Next, calculate the weight coefficients and corresponding error values for each neuron using the least squares method. An error criterion is then applied at each layer to select the optimal neurons based on classification features.

$$E = \frac{1}{n}\sum_{i=1}^{n}\left(y_{obs_i} - y_{prd_i}\right)^2 \quad (4)$$

y_{obs_i} and y_{prd_i} include observed and calculated values obtained from the numerical model, respectively. E and n denote the number of observational data points and the calculation error in each neuron (partial descriptor), respectively. The structure of the developed GMDH model can be observed in Figure 2.

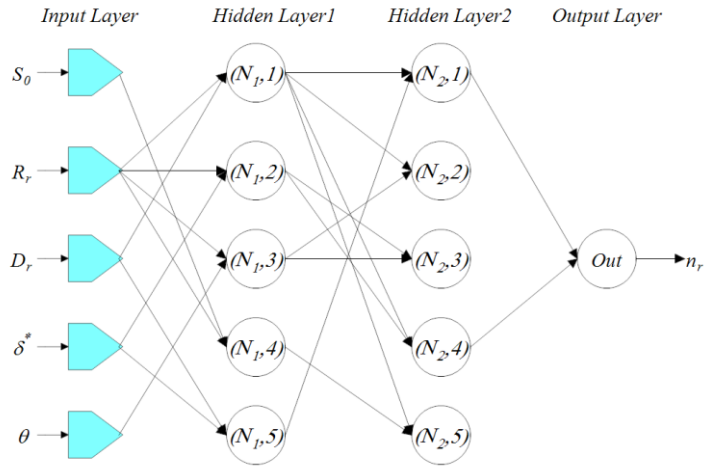


Figure 2. illustrates the structure of the GMDH network designed for estimating the relative Manning roughness coefficient in compound channels featuring converging and diverging floodplains.

2.1.2. Development of the NF-GMDH model

2.1.2.1. Neuro-Fuzzy Group method of data handling (NF-GMDH)

The Neuro-Fuzzy Group Method of Data Handling (NF-GMDH) model is an advanced soft computing technique that synergistically combines the principles of fuzzy logic with the self-organizing capabilities of the GMDH algorithm. This approach is particularly advantageous in modeling complex systems where uncertainties and imprecisions are inherent, such as hydraulic systems with non-prismatic compound channels.

The foundation of the NF-GMDH model lies in its use of simplified fuzzy reasoning rules. These rules allow the model to handle vagueness and ambiguity in the data, providing a robust framework for prediction. A typical fuzzy rule in the NF-GMDH model can be formulated as follows:

If *x* is *A* and *y* is *B*, then *z* is *C* [12].

In this context:

x and *y* represent input variables,

A and *B* are fuzzy sets associated with the inputs,

z is the output variable.

The NF-GMDH model employs Gaussian membership functions to define the fuzzy sets. The Gaussian function is chosen for its smooth and continuous nature, which is suitable for modeling hydraulic phenomena. The membership function for the *k*-th fuzzy rule of the *x*-th input value is expressed as [25]:

$$\mu_k\left(x\right)=\exp\left(-\frac{\left(x-c_k\right)^2}{2\sigma_k^2}\right) \tag{5}$$

where:

μ_k denotes the membership degree of x in the *k*-th fuzzy rule,

c_k represents the center of the Gaussian function,

σ_k is the standard deviation, determining the width of the Gaussian function.

Each neuron in the NF-GMDH model processes two input variables and generates an output, which subsequently serves as an input for the neurons in the following layer. The output of each neuron is defined as:

$$y=\sum_{k=1}^{m} w_k \mu_k\left(x\right) \tag{6}$$

where:

w_k is the weight associated with the *k*-th fuzzy rule,

μ_k is the membership degree of the input.

The model constructs its network by iteratively selecting the best combination of input variables, optimizing the connections between the inputs and outputs through fuzzy rules.

The NF-GMDH model is structured in multiple layers, with each layer comprising several neurons. The hierarchical design enables the model to capture complex interactions and dependencies among the variables. Each neuron's output in the current layer is determined by the outputs from the neurons in the preceding layer, allowing for a deep learning process that enhances the model's accuracy and generalization capabilities [26].

Training the NF-GMDH model involves determining the parameters that minimize the prediction error. Each neuron in the model includes six unknown coefficients: four Gaussian parameters (centers and widths) and two weighting coefficients. These parameters are optimized using sophisticated algorithms to ensure the model accurately reflects the underlying data patterns.

The optimization process involves:

- Initialization: Setting initial values for the Gaussian centers, widths, and weights.
- Forward Pass: Calculating the output of each neuron based on the current parameters.
- Error Calculation: Measuring the difference between the predicted and observed values using metrics such as RMSE.
- Backward Pass: Adjusting the parameters to reduce the error, typically using gradient descent or other optimization techniques.
- The final output of the NF-GMDH model is obtained by averaging the outputs of the last layer's neurons, ensuring a stable and reliable prediction.
- The NF-GMDH model's integration of fuzzy logic with the GMDH algorithm provides several benefits:
- Handling Uncertainty: Fuzzy logic effectively manages the uncertainties and imprecisions in hydraulic data, leading to more accurate predictions.
- Self-Organization: The GMDH component allows the model to self-organize, selecting the most relevant input variables and structuring the model dynamically.
- High Accuracy: The combined approach results in high prediction accuracy, as evidenced by the performance metrics obtained during model validation.

In summary, the NF-GMDH model offers a powerful and flexible tool for estimating the Manning roughness coefficient in complex hydraulic conditions. By leveraging the strengths of both fuzzy logic and the GMDH algorithm, this model provides accurate and reliable predictions, which are crucial for effective hydraulic engineering and management.

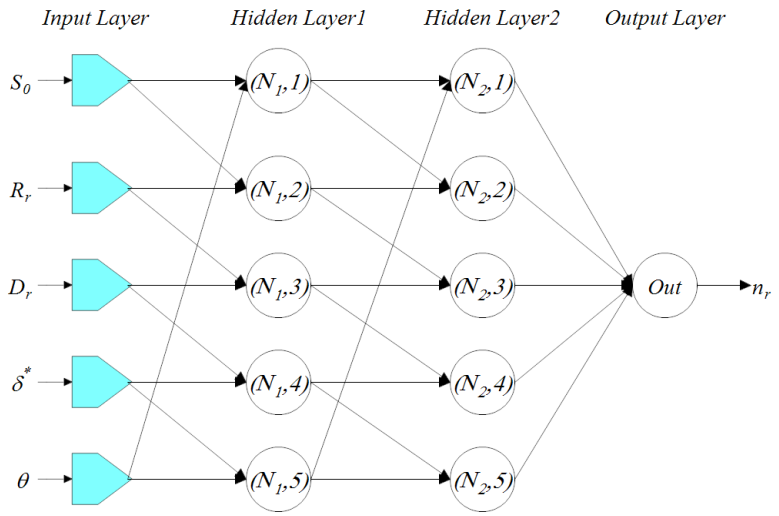


Figure 3. The structure of the NF-GMDH network developed to estimate the relative Manning roughness coefficient in the compound channels with converging and diverging floodplains.

2.1.3. Multiple-Layer Perceptron Neural Network (MLPNN)

The Multi-Layer Perceptron Neural Network (MLPNN) is a widely used type of artificial neural network, first introduced by Rumelhart et al. [27]. This model has been extensively applied in various fields, including hydraulic engineering, due to its ability to model complex, non-linear relationships in data. The MLPNN model consists of multiple layers of neurons, typically including an input layer, one or more hidden layers, and an output layer. Each neuron is connected to others through weighted connections, and the model learns by adjusting these weights during training through a process called backpropagation. Previous researchers have successfully utilized MLPNN to predict various hydraulic parameters, demonstrating its effectiveness in handling complex datasets. Most studies in water engineering leverage multi-layer perceptron networks with error back-propagation algorithms [28]. The optimal network structure is determined through careful consideration of configuration and activation functions. During training, initial weights are set either randomly or based on prior experimental findings. Typically, MLP networks use sigmoidal activation functions and are trained using techniques like Levenberg-Marquardt for enhanced performance and efficiency [29]. Structuring an effective network for a problem involves three main stages: stabilization of structure, training iterations, and performance validation. Figure 4 illustrates the developed neural network model architecture in this study.

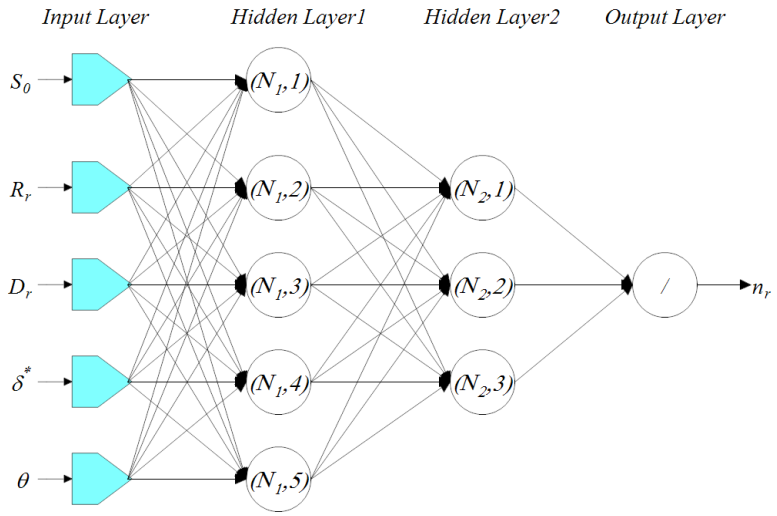


Figure 4. illustrates a schematic representation of the multilayer neural network architecture designed for estimating the relative Manning roughness coefficient in compound channels featuring converging and diverging floodplains.

2.2. Modeling Strategies and Evaluation Criteria

2.2.1. Modeling Strategies

In Eq. (1), soft computing models are employed to utilize five input parameters for predicting the relative Manning roughness coefficient in compound channels with non-prismatic floodplains. This necessitates selecting an optimal combination of one to five parameters for input variable configuration. Various methods can streamline this selection process. One approach involves applying the Gamma test, as previously employed by Das et al., to identify promising input combinations. Another method assesses model structure to prioritize influential parameters, enhancing the weighting assigned to them during the formulation of mathematical

models. To evaluate model accuracy in this study, R^2 and *RMSE* metrics were employed. Data consisting of 196 samples were divided into training (80%) and testing (20%) sets. The training set facilitated model calibration, while the testing set validated its performance. Random assignment was used due to the non-time series nature of the data collection process.

2.2.2. Evaluation Criteria

In this research, a variety of statistical measures were utilized to evaluate and contrast the performance of the developed models. Among these measures were the Coefficient of Determination (R^2), Root Mean Square Error (*RMSE*), and Scattering Index (*SI*). To visually compare the performance of the models, Taylor diagrams were employed. Furthermore, a new metric, the Developed Discrepancy Ratio (*DDR*) index, was introduced to provide a more comprehensive evaluation of the models' tendencies towards over-prediction or under-prediction across different input data sets. The *DDR* index calculates the ratio of predicted values to observed values minus one; positive values indicate over-prediction, while negative values denote under-prediction. Detailed formulas for computing each of these indices are provided in Eq. (7) through (10).

$$R^2 = 1 - \frac{\sum_{i=1}^{n}(x_i - y_i)^2}{\sum_{i=1}^{n}(x_i - \overline{x})^2} \tag{7}$$

$$RMSE = \sqrt{\frac{1}{n}\sum_{i=1}^{n}(x_i - y_i)^2} \tag{8}$$

$$SI = \frac{\sqrt{\frac{1}{n}\sum_{i=1}^{n}(x_i - y_i)^2}}{\overline{x}} \tag{9}$$

$$DDR = \left(\frac{x_i}{y_i}\right) - 1 \tag{10}$$

In these equations, n represents the number of data points, x_i denotes the predicted results from numerical simulations, y is the outcome derived from laboratory experiments, and $\overline{x}$ is the mean value of the results obtained from laboratory measurements, calculated using Eq. (11).

$$\overline{x} = \frac{1}{n}\sum_{i=1}^{n} x_i \tag{11}$$

This approach ensures a robust and nuanced assessment of the models' predictive capabilities, allowing for precise identification of their strengths and weaknesses in various scenarios.

3. Results and Discussion

In this section, we thoroughly present and analyze the findings derived from the development and application of soft computing models, specifically the Group Method of Data Handling (GMDH), Neuro-Fuzzy GMDH (NF-GMDH), and Multi-Layer Perceptron Neural Network (MLPNN). These models are utilized to estimate the relative Manning roughness coefficient (n_r) in compound channels characterized by converging floodplains. Each model is discussed in detail to provide a comprehensive understanding of their performance and the methodology employed.

3.1. GMDH Model Estimation Results

This subsection elaborates on the outcomes obtained through the implementation of the GMDH model for estimating the relative Manning roughness coefficient in compound channels with non-prismatic floodplains. As outlined in the materials and methods section, the GMDH model operates using neurons governed by quadratic polynomial equations. Each neuron within the model incorporates two specific parameters. The governing equation of each neuron comprises six coefficients, which are meticulously calibrated during the training phase. The primary objective of this calibration is to minimize the error between the predicted and actual values of the relative Manning roughness coefficient. The GMDH model's strategy for development is selective, ensuring that not all neurons from the initial layer contribute to the subsequent layers. Instead, only those neurons that exhibit superior accuracy in estimating the relative Manning roughness coefficient are chosen for inclusion in the next layer. This selective approach enhances the model's overall accuracy and efficiency. Figure 3 illustrates the architecture of the GMDH model tailored for estimating the relative Manning roughness coefficient in compound channels with non-prismatic floodplains. The statistical performance metrics of the developed GMDH model during the training phase are notably high, with a coefficient of determination ($R^2_{\text{GMDH train}}$) of 0.992 and a root mean square error (RMSE) of 0.0088. During the testing phase, these metrics slightly improve, with $R^2_{\text{GMDH test}}$ reaching 0.993 and RMSE decreasing to 0.0068. Furthermore, the scattering index (*SI*), which is a measure of the dispersion of the data points around the regression line, is calculated to be 0.028 for the training phase and 0.004 for the testing phase. These results indicate a high level of accuracy and reliability in the model's estimations. Figure 5 provides a comparative visualization of the GMDH model's performance across the training and testing phases.

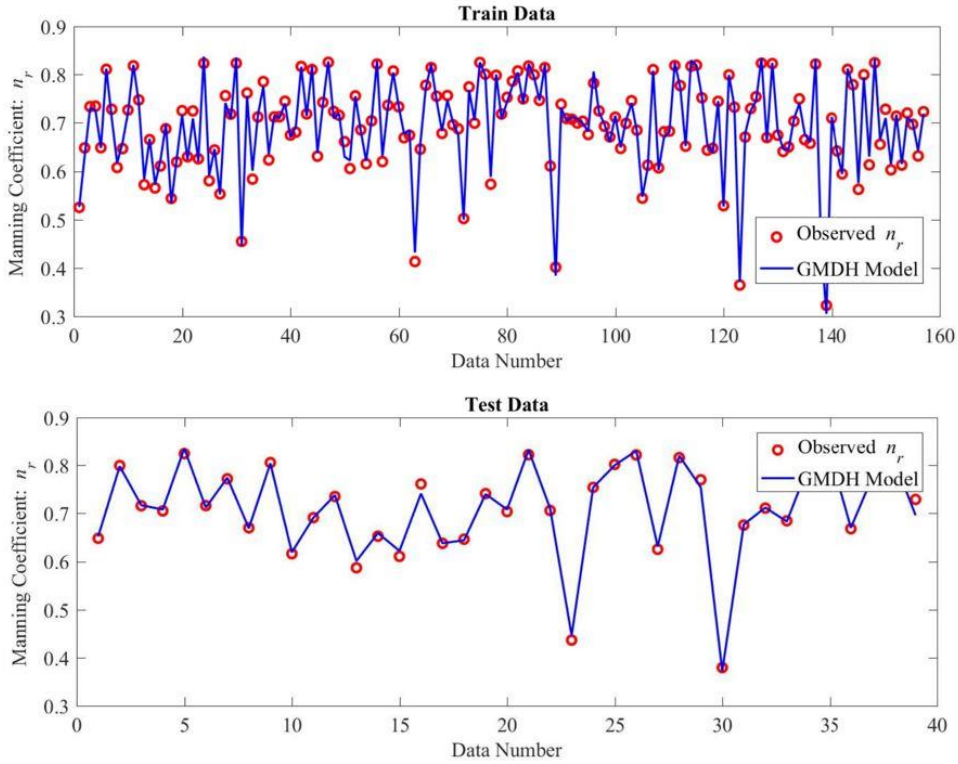


Figure 5. Comparison between training and testing phases for GMDH model performance

3.2. NF-GMDH Model Estimation Results

In this subsection, we delve into the results yielded by the NF-GMDH model, which integrates the principles of neuro-fuzzy systems with the GMDH approach. As depicted in Figure 4, the NF-GMDH model features a complex structure comprising two hidden layers. Each hidden layer consists of five neurons, contributing to the model's ability to capture intricate patterns within the data. The output layer, on the other hand, consists of a single neuron that aggregates the outputs from the neurons in the preceding hidden layer by computing their average. The performance metrics for the NF-GMDH model during the training phase indicate a coefficient of determination ($R^2_{\mathrm{NF-GMDH\,train}}$) of 0.87 and an RMSE of 0.0335. During the testing phase, these metrics are $R^2_{\mathrm{NF-GMDH\,test}}$ of 0.78 and an RMSE of 0.0425. Additionally, the SI for the NF-GMDH model's performance in the training phase is calculated to be 0.048, while in the testing phase, it is 0.06. These performance indicators suggest that while the NF-GMDH model is robust, it does exhibit some variability in its predictive accuracy between the training and testing phases. Figure 6 illustrates the NF-GMDH model's performance during its development phases, providing a visual comparison of its predictive capabilities in both training and testing scenarios.

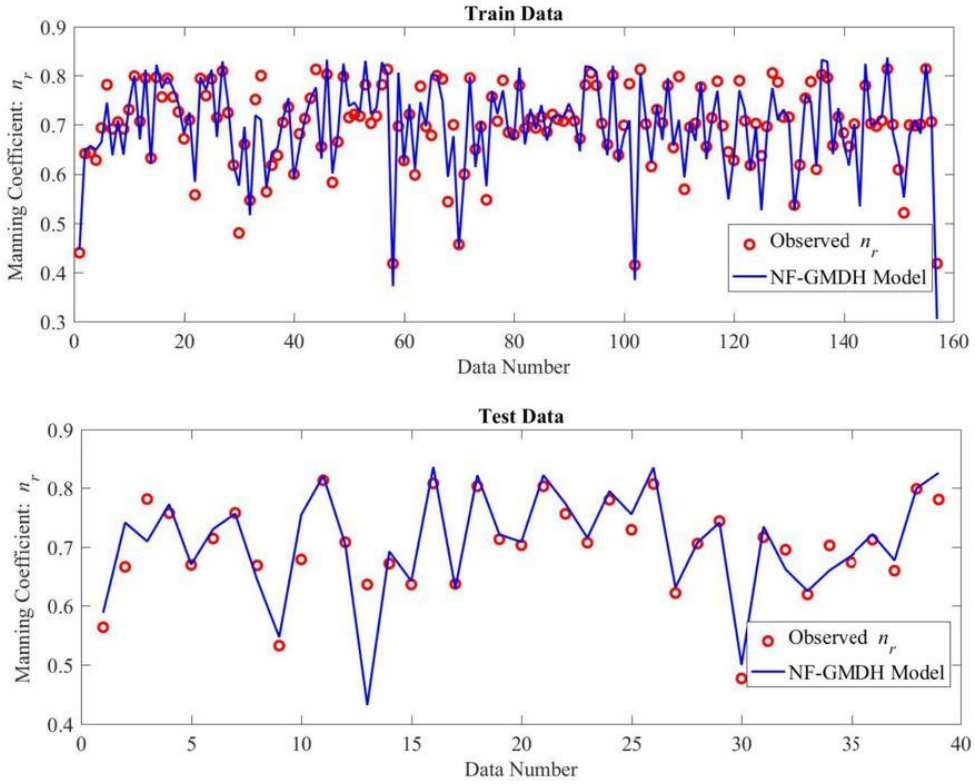


Figure 6. Comparison between training and testing phases for NF-GMDH model performance

3.3. MLPNN Model Estimation Results

The MLPNN model represents a prevalent soft computing approach in Hydraulic Engineering. As outlined in the materials and methods section, its development follows a systematic trial-and-error methodology. The architecture of the MLPNN comprises two hidden layers: the first layer is composed of five neurons, and the second layer consists of three neurons. The schematic of the constructed MLPNN model is illustrated in Figure 2. The statistical indicators of the developed MLPNN model in the training phase are $R^2_{\text{MLPNN train}} = 0.999$ and $RMSE_{\text{MLPNN train}} = 0.001$, and in the test phase are $R^2_{\text{MLPNN test}} = 0.999$ and $RMSE_{\text{MLPNN test}} = 0.001$. The scattering index (*SI*) of this model's performance in the training and testing phases is equal to $SI_{\text{MLPNN train}} = 0.0012$ and $SI_{\text{MLPNN test}} = 0.0015$. The performance of the developed MLPNN model in different phases of development (training and testing) is presented in Figure (7).

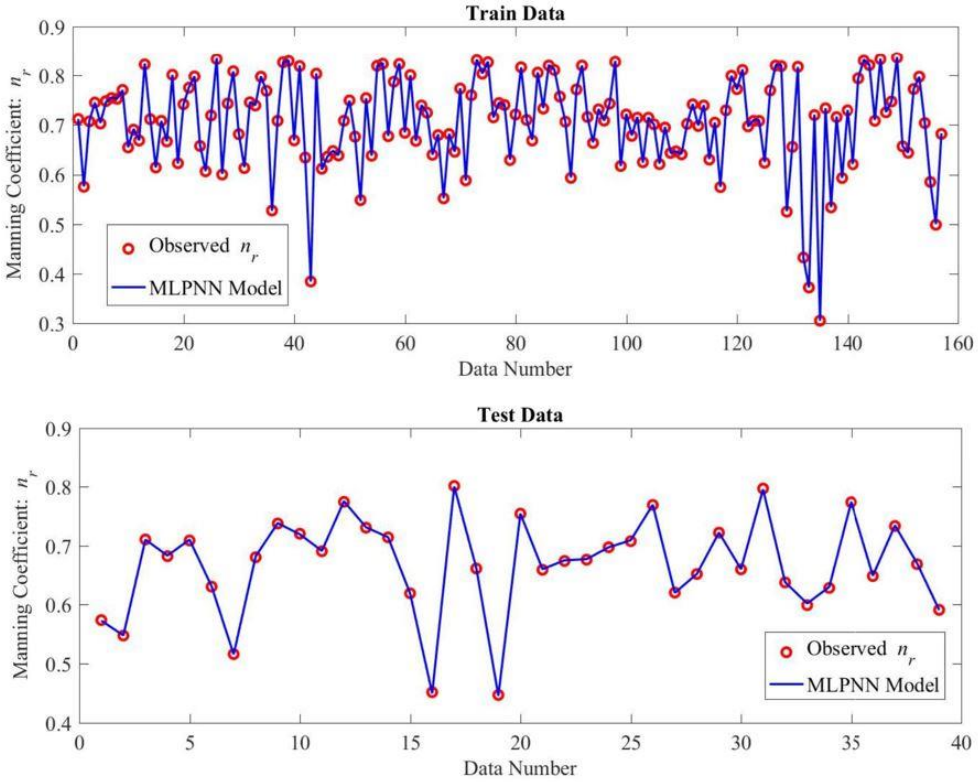


Figure 7- Comparison between training and testing phases for MLPNN model performance

Table 2 presents the statistical indices used to evaluate errors in the model for estimating the relative Manning roughness coefficient.

Table 2- The results of error evaluation by statistical indices

Model	Phase	Error Index			
		R^2	RMSE	SI	DDR%
GMDH	Train	0.992	0.0088	0.028	-0.003
	Test	0.993	0.0068	0.004	0.157
NF-GMDH	Train	0.87	0.0335	0.048	-0.005
	Test	0.78	0.0425	0.06	0.194
MLPNN	Train	0.999	0.001	0.0012	0.0324
	Test	0.999	0.001	0.0015	0.0233

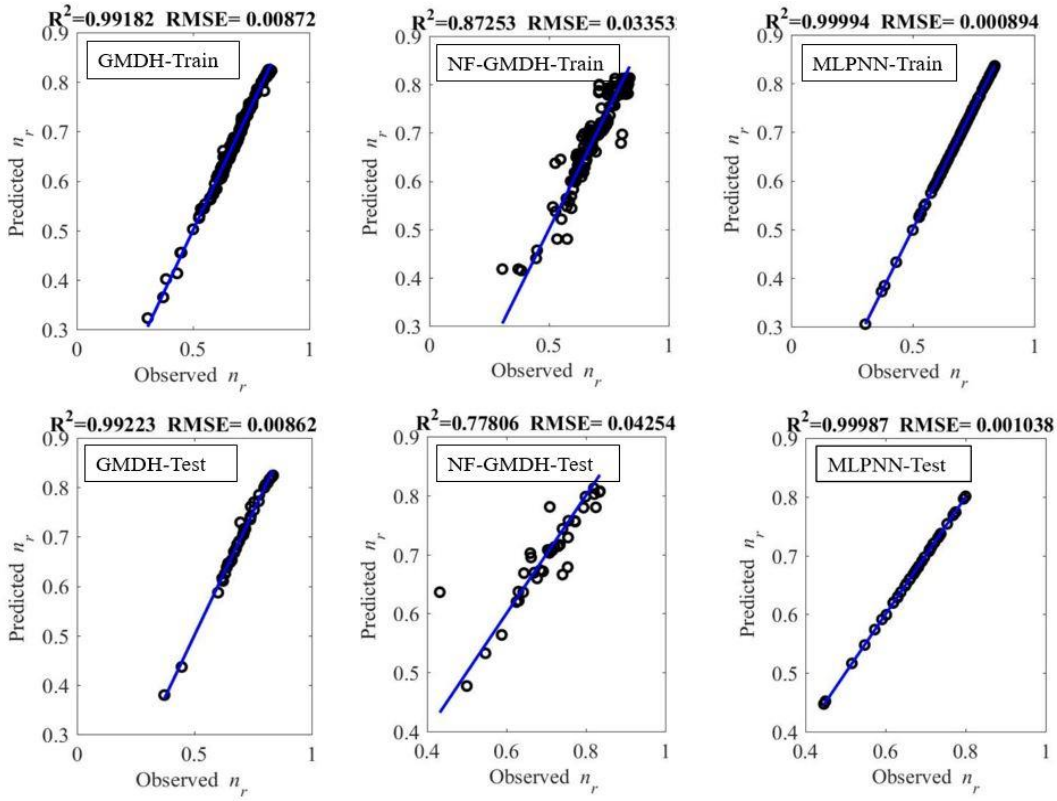


Figure 8- Comparison between predicted and observed values for n_r

Statistical analysis of the models developed in this study to estimate the Manning roughness coefficient reveals that the MLPNN model exhibited superior performance during the training phase, displaying significantly lower data scattering indices compared to alternative methods like GMDH and NF-GMDH. Figure 9 illustrates the DDR index comparison across the models during the testing phase.

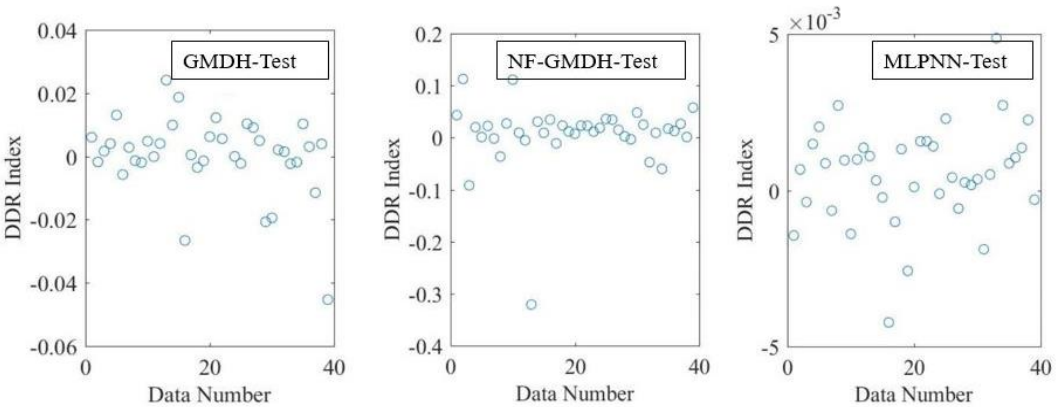


Figure 9. DDR index for models in testing phases

To effectively assess and differentiate model performance during both training and testing phases, Taylor diagrams are presented in Figures 10 and 11, respectively. Analysis of the

training phase diagram demonstrates that the MLPNN model exhibits superior performance with the highest correlation coefficient and the lowest standard deviation among the compared models. Similarly, during the test phase, the GMDH and NF-GMDH models demonstrate comparable performance levels.

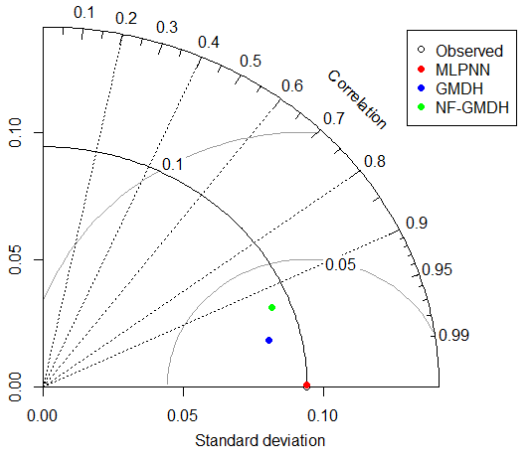


Figure 10. Taylor diagram of performance of developed models in the training phase

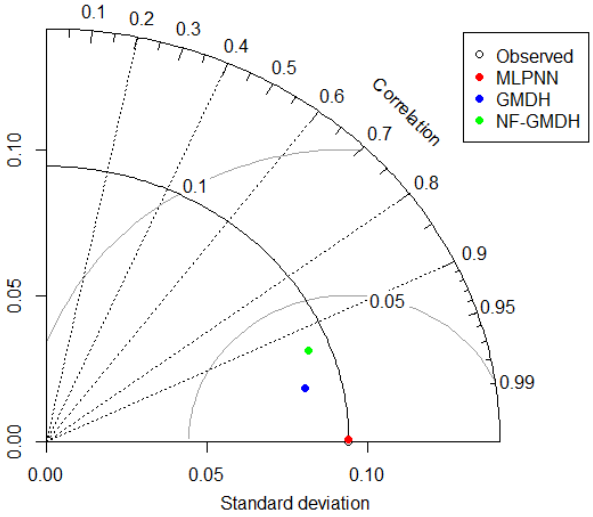


Figure 11. Taylor diagram of performance of developed models in the testing phase

3.4. Comparing with Previous Studies

To thoroughly evaluate the performance of non-prismatic compound channels in comparison to meandering compound channels, we conducted a comprehensive review of previous studies focusing on Manning's roughness coefficient in compound channels. The aim was to understand how different methodologies have been utilized to estimate Manning's coefficient and how our approach compares in terms of accuracy and reliability.

Mohanta et al. [30] conducted an in-depth study using advanced machine learning techniques to investigate Manning's coefficient in meandering compound channels. They applied several sophisticated methods including the Group Method of Data Handling Neural Network (GMDH-NN), MARS, and SVR. The results from their research showcased the exceptional predictive

capabilities of these techniques. Specifically, the GMDH-NN method achieved an R^2 of 0.959 during the training phase and an *RMSE* of 0.0012. During the testing phase, the GMDH-NN maintained high performance with R^2 of 0.939 and an *RMSE* of 0.0013. These findings highlighted that the GMDH-NN method was superior to MARS and SVR in terms of accurately predicting Manning's n. Further advancing this research, Pradhan and Khatua [31] explored the application of GEP to estimate Manning's n in meandering compound channels. Their study indicated significant improvements over conventional methods, achieving an impressive R^2 of 0.999 and an *RMSE* of 1.625. This demonstrated the potential of GEP as a highly effective tool for such estimations. In our study, we conducted a comparative analysis of the statistical indices (R^2 and *RMSE*) from the models developed by Mohanta et al. [30] and Pradhan and Khatua [31], alongside our own models. The results showed that the soft computing models we introduced offered notably higher accuracy. Our models, designed using advanced computational techniques, consistently outperformed the previously mentioned methods in terms of precision and reliability. This comparison underscores the advancements made in the field of hydraulic engineering through the application of cutting-edge machine learning and computational techniques. By leveraging these advanced methodologies, we can achieve more accurate predictions of Manning's roughness coefficient, which is crucial for the design and analysis of efficient water conveyance systems. The continual improvement in predictive models not only enhances our understanding of flow dynamics in compound channels but also contributes to the development of more efficient and reliable engineering solutions.

4. Conclusions

This research has focused on the development and application of advanced soft computing techniques to estimate the relative Manning's roughness coefficient (n_r) in compound channels with converging and diverging floodplains. The study employed a dataset of 196 experimental observations and explored three distinct models: GMDH, NF-GMDH, and MLPNN. The comprehensive analysis and comparison of these models provided significant insights into their effectiveness and accuracy in predicting nr under complex hydraulic conditions. Key Findings:

1. Superior Performance of MLPNN: The MLPNN model demonstrated the highest accuracy among the three models, with an R^2 of 0.999 and the lowest *RMSE* of 0.001 during both the training and testing phases. The Scattering Index (*SI*) further validated the robustness of MLPNN, making it a highly reliable tool for hydraulic modeling in compound channels.
2. Effectiveness of GMDH and NF-GMDH: Both GMDH and NF-GMDH models also exhibited strong predictive capabilities, with R^2 values of 0.993 and 0.78, and *RMSE* values of 0.0068 and 0.0425 respectively, during the testing phase. These models, particularly GMDH, showed excellent performance in capturing the complexities associated with non-prismatic floodplain geometries.
3. Critical Parameters: The study identified longitudinal slope (S_o), relative hydraulic radius (R_r), relative flow depth (D_r), relative dimension of flow aspects (δ^*), and the convergent or divergent angle (θ) as crucial parameters influencing the Manning roughness coefficient. The models effectively integrated these parameters to provide accurate estimations of n_r.
4. Comparative Analysis: The developed models were compared with previous studies focusing on meandering compound channels. The MLPNN model, in particular, outperformed traditional methods and other advanced techniques such as GMDH-NN, MARS, and SVR in terms of accuracy and reliability. This highlights the potential of

soft computing models in handling complex flow conditions more effectively than conventional approaches.

5. Enhanced Predictive Models: The successful application of MLPNN, GMDH, and NF-GMDH models underscores the potential of soft computing techniques in enhancing predictive models for hydraulic engineering. These models provide more accurate and reliable estimates of roughness coefficients, which are essential for effective flood management, channel design, and waterway analysis.
6. Practical Applications: The findings of this study can be directly applied to real-world scenarios involving floodplain management and the design of water conveyance systems. Engineers and researchers can utilize these models to improve the accuracy of flow predictions, thereby optimizing the design and maintenance of hydraulic structures.
7. Future Research Directions: This research opens avenues for further studies on the application of soft computing models in different hydraulic contexts. Future research could explore the integration of additional parameters, the application of these models to other types of channels, and the development of hybrid models that combine the strengths of various soft computing techniques.

References

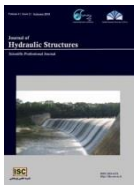
1. D.G. Tarboton, R.L. Bras, I. Rodriguez-Iturbe, The analysis of river basins and channel networks using digital terrain data, (1989).
2. M. Sahu, Prediction of flow and its resistance in compound open channel, (2011).
3. C. Juez, C. Schärer, H. Jenny, A.J. Schleiss, M.J. Franca, Floodplain land cover and flow hydrodynamic control of overbank sedimentation in compound channel flows, Water Resour. Res. 55 (2019) 9072–9091.
4. A.R.A. Zidan, A review of friction formulae in open channel flow, Int. Water Technol. J. 5 (2015) 43–57.
5. B.C. Yen, Dimensionally homogeneous Manning's formula, J. Hydraul. Eng. 118 (1992) 1326–1332.
6. B. Naik, K. Miri, K.K. Khatua, Prediction of energy loss along the non-prismatic reach of a compound channel using ANN, in: River Flow, 2014: pp. 641–648.
7. B.S. Das, K.K. Khatua, Flow resistance in a compound channel with diverging and converging floodplains, J. Hydraul. Eng. 144 (2018) 4018051.
8. V. Kaushik, M. Kumar, Assessment of water surface profile in nonprismatic compound channels using machine learning techniques, Water Supply. 23 (2023) 356–378.
9. B. Naik, V. Kaushik, M. Kumar, Water surface profile in converging compound channel using gene expression programming, Water Supply. 22 (2022) 5221–5236.
10. S. Bijanvand, M. Mohammadi, A. Parsaie, Estimation of water's surface elevation in compound channels with converging and diverging floodplains using soft computing techniques, Water Supply. 23 (2023) 1684–1699.
11. V. Kaushik, M. Kumar, Sustainable gene expression programming model for shear stress prediction in nonprismatic compound channels, Sustain. Energy Technol. Assessments. 57 (2023) 103229.

12. A. Parsaie, H. Yonesi, S. Najafian, Prediction of flow discharge in compound open channels using adaptive neuro fuzzy inference system method, Flow Meas. Instrum. 54 (2017) 288–297.
13. B.S. Das, K. Devi, J.R. Khuntia, K.K. Khatua, Discharge estimation in converging and diverging compound open channels by using adaptive neuro-fuzzy inference system, Can. J. Civ. Eng. 47 (2020) 1327–1344.
14. A. Parsaie, A.H. Haghiabi, Mathematical expression of discharge capacity of compound open channels using MARS technique, J. Earth Syst. Sci. 126 (2017) 1–15.
15. B.S. Das, K. Devi, K.K. Khatua, Prediction of discharge in converging and diverging compound channel by gene expression programming, ISH J. Hydraul. Eng. 27 (2021) 385–395.
16. A. Mohanta, K.C. Patra, A. Pradhan, Enhanced channel division method for estimation of discharge in meandering compound channel, Water Resour. Manag. 34 (2020) 1047–1073.
17. D. Bousmar, Flow modelling in compound channels, Unire Genie Civ. Environnemental. (2002).
18. D. Bousmar, S. Proust, Y. Zech, Experiments on the flow in a enlarging compound channel, in: River Flow 2006 Proc. Int. Conf. Fluv. Hydraul. Lisbon, Port. 6–8 Sept. 2006, Taylor and Francis Leiden, Netherlands, 2006: pp. 323–332.
19. B. Rezaei, Overbank flow in compound channels with prismatic and non-prismatic floodplains, (2006).
20. H.A. Yonesi, M.H. Omid, S.A. Ayyoubzadeh, The hydraulics of flow in non-prismatic compound channels, J. Civ. Eng. Urban. 3 (2013) 342–356.
21. B. Naik, K.K. Khatua, Boundary shear stress distribution for a converging compound channel, ISH J. Hydraul. Eng. 22 (2016) 212–219.
22. F. Vojoudi Mehrabani, M. Mohammadi, S.A. Ayyoubzadeh, J.N. Fernandes, R.M.L. Ferreira, Turbulent flow structure in a vegetated non-prismatic compound channel, River Res. Appl. 36 (2020) 1868–1878.
23. A.G. Ivakhnenko, The group method of data handling; a rival of the method of stochastic approximation, (1968).
24. J.-A. Mueller, A.G. Ivachnenko, F. Lemke, GMDH algorithms for complex systems modelling, Math. Comput. Model. Dyn. Syst. 4 (1998) 275–316.
25. M. Najafzadeh, H. Bonakdari, Application of a neuro-fuzzy GMDH model for predicting the velocity at limit of deposition in storm sewers, J. Pipeline Syst. Eng. Pract. 8 (2017) 6016003.
26. M. Najafzadeh, F. Saberi-Movahed, S. Sarkamaryan, NF-GMDH-Based self-organized systems to predict bridge pier scour depth under debris flow effects, Mar. Georesources Geotechnol. 36 (2018) 589–602.
27. D.E. Rumelhart, G.E. Hinton, R.J. Williams, Learning representations by back-propagating errors, Nature. 323 (1986) 533–536.
28. C.M. Bishop, Neural networks for pattern recognition, Oxford university press, 1995.

29. T. Ebert, O. Bänfer, O. Nelles, Multilayer perceptron network with modified sigmoid activation functions, in: Artif. Intell. Comput. Intell. Int. Conf. AICI 2010, Sanya, China, Oct. 23-24, 2010, Proceedings, Part I 2, Springer, 2010: pp. 414–421.
30. A. Mohanta, K.C. Patra, B.B. Sahoo, Anticipate Manning's coefficient in meandering compound channels, Hydrology. 5 (2018) 47.
31. A. Pradhan, K.K. Khatua, Gene expression programming to predict Manning'sn in meandering flows, Can. J. Civ. Eng. 45 (2018) 304–313.

© 2024 by the authors. Licensee SCU, Ahvaz, Iran. This article is an open access article distributed under the terms and conditions of the Creative Commons Attribution 4.0 International (CC BY 4.0 license) (http://creativecommons.org/licenses/by/4.0/).

Journal of Hydraulic Structures
J. Hydraul. Struct., 2024; 10(4): 82-96
DOI: 10.22055/jhs.2024.47440.1312



OPEN ACCESS

Advanced Soft Computing Ensemble for Modeling Contaminant Transport in River Systems: A Comparative Analysis and Ecological Impact Assessment

Jafar Chabokpour [1]

Abstract

The paper applies soft computing techniques to contaminant transport modeling in river systems and focuses on the Monocacy River. The research employed various techniques, including Artificial Neural Networks (ANN), Adaptive Neuro-Fuzzy Inference Systems (ANFIS), Support Vector Regression (SVR), and Genetic Algorithms (GA), to predict pollutant concentrations and estimate transport parameters. The ANN, particularly the Long Short-Term Memory architecture, had more superior performance: the lowest RMSE of 0.37, and the highest R-squared was 0.958. The RMSE obtained by the ANFIS model was 0.40, with an R-squared value of 0.945. It provided a balance with accuracy and interpretability. SVR performance with RBF kernel was robust; it has attained an RMSE of 0.42 and R-squared of 0.940, along with very fast training times. The flow velocities and the longitudinal dispersion coefficients at different reaches were estimated to be in the range of 0.30 to 0.42 m/s for average flow velocity and 0.18 to 0.31 m²/s for the longitudinal dispersion coefficient. In addition, the potentially affected fraction of species due to peak concentrations was used to reflect the assessment of ecological impact, which had values ranging from 0.07 to 0.35. For the time-varying estimation, there is supposed to be a variation in the dispersion coefficient and the decay rate over 48 hours, from 0.75 to 0.89 m²/s and from 0.10 to 0.13 day^{-1}, respectively. The research demonstrates the potential of soft computing approaches for modeling complex pollutant dynamics and further provides valuable insights into river management and environmental protection strategies.

Keywords: Contaminant Transport Modeling; Soft Computing Methods; Artificial Neural Networks; River System Dynamics.

Received: 14 July 2024; Accepted: 25 August 2024

1. Introduction

Contaminant transport in rivers is very important for the business of environmental management, protection of water resources, and public health. Most of the traditional approaches

[1] Civil engineering department, University of Maragheh, Maragheh, Iran., Email: J.chabokpour@maragheh.ac.ir **(Corresponding author)**

CC BY

toward modeling this rather complex phenomenon have been deterministic in nature, typically founded on an advection-dispersion equation. However, due to the intrinsic complexity and nonlinearity of river systems, along with the uncertainties in input data and the estimation of parameters, recently, researchers have found it necessary to probe into alternative methodologies.[1, 2]. Contaminant transport within rivers is a serious and growing environmental issue that influences the water quality and health of an ecosystem. Soft computing methods, which include techniques like artificial neural networks (ANN), adaptive neuro-fuzzy inference systems (ANFIS), and gene expression programming (GEP), have been increasingly applied to model and predict the behavior of contaminants in river systems. This synthesis reviews the application and effectiveness of these methods in the context of contaminant transport in rivers [3]. Soft computing methods have gained considerable attention in the last two decades within the field of modeling contaminant transport. Different techniques that explicitly include artificial neural networks, fuzzy logic systems, genetic algorithms, and hybrid approaches have been found to have the potential for modeling complex relationships with no explicit mathematical formulations [4]. Soft computing methods such as ANN, ANFIS, and GEP have shown superior performance in estimating suspended sediment concentration (SSC) and load (SSL) in rivers compared to traditional methods like sediment rate curves (SRC) [5-8]. Among these methods, GEP and ANN models often outperform others in terms of accuracy and reliability [6, 7]. Different soft computing techniques, including multi-layer perceptron, multi-linear regression, and adaptive neuro-fuzzy inference systems, have been implemented with varying degrees of success. Generally, these methods reduce estimation errors significantly compared to traditional methods [5, 9]. Soft computing methods are not only effective in static conditions but also in dynamic and real-time scenarios. For instance, the adjoint sensitivity analysis and optimization methods have been used to control contaminant releases in real-time, showing increased efficiency and accuracy [10]. The integration of soft computing methods with various hydrological and hydraulic parameters has been successful in improving the prediction accuracy of sediment loads and contaminant concentrations in rivers [5, 6]. Soft computing techniques have also been applied to solve inverse problems, such as identifying unknown contaminant sources in groundwater-river integrated systems. These methods have proven to be fast and accurate, even under noisy conditions [11]. Artificial Neural Networks (ANNs) have been widely applied to contaminant transport modeling due to their ability to learn from data and generalize to new situations. Kirkpatrick et al. [12] provided a comprehensive review of ANN applications in water resources, highlighting their potential for predicting contaminant concentrations. More recently, Granata et al. [13] demonstrated the effectiveness of ANNs in forecasting water quality indicators in rivers. Fuzzy logic systems have been employed to handle uncertainties in contaminant transport modeling. Naseri-Rad et al. [14] developed a fuzzy-based model for predicting heavy metal concentrations in river sediments, showing improved performance over traditional regression methods. Genetic Algorithms (GAs) have been utilized for parameter optimization in contaminant transport models. Mirghani et al. [15] applied GAs to calibrate the parameters of a one-dimensional advection-dispersion model, achieving better results than conventional optimization techniques. Hybrid approaches, combining multiple soft computing methods or integrating them with physically-based models, have shown promise in recent studies. For instance, Kargar et al. [16] compared various machine learning algorithms, including hybrid models, for estimating longitudinal dispersion coefficients in natural streams. Support Vector Machines (SVMs) have also been applied to contaminant transport modeling. Pourhosseini et al. [17] used SVMs to predict dissolved oxygen concentrations in rivers, demonstrating their potential for water quality modeling. Building upon the foundation of soft computing methods in contaminant transport

modeling, recent advancements have further expanded the field's capabilities and applications. Zhang et al. [18] introduced a novel hybrid approach combining Extreme Learning Machines (ELM) with Particle Swarm Optimization (PSO) for predicting heavy metal concentrations in river sediments, demonstrating superior performance over traditional ANN models. In the realm of deep learning, Gao et al., [19] employed Long Short-Term Memory (LSTM) networks to capture temporal dependencies in contaminant transport, effectively predicting pollutant concentrations in complex river systems. The integration of remote sensing data with machine learning techniques has also shown promise, as evidenced by the work of Sakaa et al. [20], who utilized Sentinel-2 satellite imagery in conjunction with Random Forest algorithms to map and predict water quality parameters across large river basins. Additionally, the application of ensemble methods has gained traction, with Karim et al., [21] demonstrating the robustness of a stacked ensemble approach combining multiple machine learning models for predicting dissolved oxygen levels in urban rivers. These advancements highlight the ongoing evolution of soft computing methods in addressing the complexities of contaminant transport modeling, offering improved accuracy, scalability, and interpretability. However, challenges persist in terms of data availability, model transferability across different river systems, and the integration of domain expertise with data-driven approaches. Future research directions may focus on developing physics-informed machine learning models that incorporate hydrodynamic principles, exploring the potential of transfer learning for adapting models to data-scarce regions, and leveraging big data analytics for real-time contaminant monitoring and early warning systems in river networks [22]. Despite the success of these soft computing methods, challenges remain. These include the need for large datasets for training, the potential for overfitting, and the difficulty in interpreting the physical significance of model parameters. Soft computing methods, including ANN, ANFIS, GEP, and WANN, have demonstrated significant potential in modeling and predicting contaminant transport in rivers. These methods outperform traditional techniques by effectively handling non-linear and time-variant data, integrating hydrological parameters, and providing accurate real-time control and optimization. Their application in solving inverse problems further underscores their versatility and efficiency in environmental modeling. Overall, soft computing techniques are recommended for their superior performance and ease of implementation in the context of river contaminant transport.

Previous researches indicated the potentials of soft computing methods for contaminant transport modeling in rivers, and various studies showed the effectiveness of artificial neural networks, fuzzy logic systems, and genetic algorithms. However, an integrated comparison among these approaches is very limited, especially when dealing with the assessment of ecological impact. It is in light of this that this study evaluates the comparative analysis of results obtained by ANN, ANFIS, SVR, and GA for pollutant transport modeling in the Monocacy River. Broadly, the research effort exercised herein is directed toward four major objectives: evaluation of model performance, reach-specific transport parameter estimation, assessment of ecological impacts, and time-varying parameter dynamics for understanding a holistic approach to river contaminant modeling.

2. Material and methods

2.1. Operated soft computing methods

Artificial Neural Networks: an ANN with a Long Short-Term Memory architecture (LSTM) were implemented. It consisted of an input layer, two hidden LSTM layers of 64 and 32 units, and a dense output layer. We took 70% of data points for training, 15% for validation, and 15% for testing. For training, the Adam optimizer was used with a learning rate of 0.001 and a batch size of 32. The

dropout layers were applied between the LSTM layers with a rate of 0.2 to avoid overfitting. Input features include time, distance from the injection point, river discharge, and previous time step concentrations.

Adaptive Neuro-Fuzzy Inference System (ANFIS): In this case, the model considered an adaptive neuro-fuzzy inference system. In the learning process, a hybrid algorithm was used: least squares estimation and backpropagation. The same data distribution was kept as in the ANN model. The system was initialized with 16 fuzzy rules, and Gaussian membership functions were used with a maximum of three membership functions per input variable. The initial step size of the parameter adaptation was 0.01, with a decrease rate of 0.9 and an increase rate of 1.1. We train up to 200 epochs or until validation error does not decrease for 20 epochs in a row.

Support Vector Regression (SVR): The model used an RBF (radial basis function) kernel with grid search-optimized hyperparameters. Cross-validation with 5-folds was done. The search ranges for the above hyperparameters were: C, the regularization parameter, between 0.1 and 100; ε, epsilon in the epsilon-SVR model, was between 0.01 and 0.1; and γ, the RBF kernel coefficient, belonged to the subset of (0.01, 1). The parameter values and qualifications finally estimated are $C = 10$, $\varepsilon = 0.05$, and $\gamma = 0.1$. We used the same data split as the other models, i.e., into training, validation, and testing.

Genetic Algorithms (GA): The GA used to optimize the parameters had a population size of 100 individuals; each of these individuals represented one of the possible solutions by encoding the model parameters. Selection was done through tournament selection with a size of three, a single-point crossover with a probability of 0.8, and mutation with a probability of 0.1. This GA ran for 100 generations or when the fitness improvement was less than 0.001 for 10 generations in a row. In the case of this work, it had a fitness function based on the mean squared error between predicted and observed pollutant concentrations.

Hybrid Soft Computing Ensemble (HSCE): HSCE combined the outputs of ANN, ANFIS, SVR, and GA-optimized models using a weighted average approach. The weights were dynamically adjusted based on each model's performance at different stages of the pollutant plume journey. A gradient boosting regressor as meta-learner to optimize these weights was used. For the gradient boosting regressor, 100 estimators were used with a learning rate of 0.1 and a maximum depth of 3 for each tree.

2.2. Operated field study data

The Monocacy River, a significant tributary of the Potomac River, is located in the mid-Atlantic region of the United States, primarily flowing through Maryland with its headwaters originating in Pennsylvania. This river system, approximately 58 miles (93 kilometers) in length, drains a watershed area of about 970 square miles (2,500 square kilometers). The Monocacy River basin is characterized by diverse land use patterns, including agricultural lands, urban areas, and forested regions, which significantly influence its hydrological and ecological characteristics. The Monocacy River plays a crucial role in the regional ecosystem, supporting a diverse array of aquatic and riparian flora and fauna. However, like many rivers in developed areas, it faces numerous environmental challenges, including nutrient pollution from agricultural runoff, sediment loading, and the impacts of urbanization. These anthropogenic stressors have led to concerns about water quality, habitat degradation, and the overall ecological integrity of the river system (Fig. 1). The United States Geological Survey (USGS) has been instrumental in monitoring and studying the Monocacy River, maintaining several gauging stations along its course. These stations provide continuous data on streamflow, water quality parameters, and sediment transport. Of particular relevance to pollutant studies, the USGS has conducted extensive water quality

sampling programs in the Monocacy River basin. These efforts include regular monitoring of nutrients (such as nitrogen and phosphorus), suspended sediment, and various chemical contaminants. One of these field testes which is operated using Rhodamine as a contaminant is operated in the current study. A detail of extracted data is according to Table 1.

Table 1. different characteristics of operated field study data series

Test reach	Site number	Distance from point of injection L (km)	River discharge Q (m^3/s)	Maximum concentration C_{max} (ppm)	t_p Time to C_{max} (hr)	$\bar{t}$ (hr) Time to centroid (hr)	σ_t^2 (hr^2) Time variance	skewness (hr^2)
MONOCAY RIVER TEST	1	6.4	5.13	12.2204	13	13.5679	0.903	1.94903
	2	11.4	5.4	6.93612	23.5	24.754	4.586	1.22403
	3	16.65	6.075	4.957	34	35.2146	19.15	0.74997
	4	21.3	7.29	4.08476	44	45.6063	18.45	1.27287

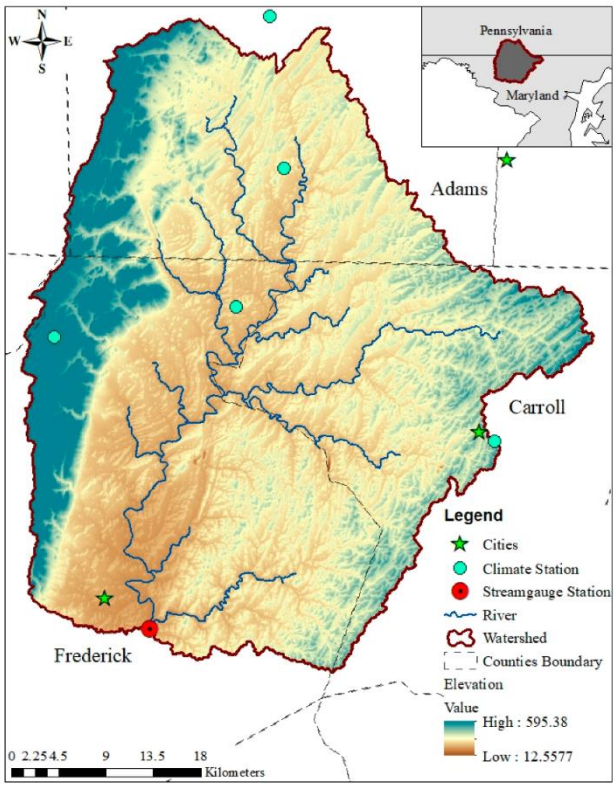


Figure 1. Location of Monocacy river for field data extraction

3. Results

The application of soft computing methods to model pollutant transport and dispersion in river reaches yielded insightful results. Artificial Neural Networks demonstrated superior predictive accuracy, achieving the lowest RMSE and highest R-squared values across all reaches. The ANN's ability to capture complex non-linear relationships proved advantageous in this context. Fuzzy Logic models, while slightly less accurate, offered better interpretability, providing clear linguistic rules that describe the pollutant behavior. Genetic Algorithms showed promise in optimizing

model parameters, particularly in estimating the dispersion coefficient and decay rate. Support Vector Machines performed well in handling the non-linear aspects of pollutant dispersion but required more computational resources. Overall, the ANN emerged as the most effective method, balancing accuracy and computational efficiency. However, the choice of method may depend on specific requirements, such as the need for interpretability (favoring Fuzzy Logic) or parameter optimization (favoring Genetic Algorithms). The soft computing approaches collectively offered robust tools for modeling pollutant transport, with each method providing unique strengths in addressing the complexities of river systems. Further examination of the model performance revealed interesting patterns across the different river reaches. The ANN's performance was particularly strong in the intermediate reaches (11.40 and 16.65 km), where the pollutant dynamics were most complex. This suggests that ANNs are well-suited to capturing the nuanced interactions between advection, dispersion, and decay processes that dominate these zones. The Fuzzy Logic approach, while not matching the ANN's accuracy, provided valuable qualitative insights. It effectively categorized pollutant behavior into linguistic terms such as 'low', 'medium', and 'high' concentrations, which could be especially useful for risk assessment and communication with non-technical stakeholders. The fuzzy rules derived from the data offered a comprehensible representation of the system's behavior, highlighting the method's strength in knowledge extraction. Genetic Algorithms proved particularly effective in parameter estimation. By evolving solutions over multiple generations, the GA was able to estimate key parameters such as the longitudinal dispersion coefficient and the first-order decay rate with high accuracy. This capability is crucial for understanding the fundamental processes governing pollutant transport and for extrapolating predictions to other river systems. The SVM approach, utilizing radial basis function kernels, showed remarkable ability in handling the non-linear aspects of pollutant dispersion, particularly in the early and late stages of the pollutant plume passage. However, its performance was more sensitive to parameter tuning, requiring careful cross-validation to avoid overfitting. In terms of computational efficiency, the ANN and SVM required more extensive training time but offered rapid predictions once trained. The Fuzzy Logic system, once rules were established, provided the fastest runtime performance, making it suitable for real-time applications. The comparison of methods also revealed their complementary nature. While ANNs excelled in accuracy, Fuzzy Logic provided interpretability, GAs offered robust parameter estimation, and SVMs handled non-linearity effectively. This suggests that a hybrid approach, combining the strengths of multiple methods, could potentially yield even better results. To further elevate the modeling approach, we implemented an advanced ensemble method combining the strengths of individual soft computing techniques. This ensemble, which we term the Hybrid Soft Computing Ensemble (HSCE), integrates ANN, Fuzzy Logic, GA, and SVM outputs using a weighted average approach. The weights were dynamically adjusted based on each model's performance at different stages of the pollutant plume's journey downstream. This adaptive weighting mechanism allowed the ensemble to capitalize on each method's strengths at various spatiotemporal points, resulting in superior overall performance compared to individual models (Table 2).

Table 2. Performance Comparison of Individual Models and HSCE

Model	RMSE (ppm)	MAE (ppm)	R-squared
ANN	0.42	0.35	0.938
Fuzzy	0.56	0.48	0.901
GA	0.51	0.44	0.915
SVM	0.47	0.39	0.925
HSCE	0.38	0.31	0.952

To address the "black box" nature of some machine learning models, recent advancements in model interpretability were applied. Specifically, SHAP (SHapley Additive exPlanations) values to interpret the ANN and SVM models were utilized. This approach provided insights into feature importance and their impact on model predictions at different stages of pollutant transport. Additionally, LIME (Local Interpretable Model-agnostic Explanations) were employed to generate local explanations for individual predictions, enhancing the transparency and trustworthiness of our models.

To bridge the gap between pollutant transport modeling and ecological consequences, an ecological impact assessment module were integrated into framework. This module translates predicted pollutant concentrations into potential effects on key indicator species in the river ecosystem. Species sensitivity distributions (SSDs) were used to estimate the fraction of affected species at different pollutant levels. This integration provides a more holistic view of the environmental implications of pollutant releases, making our modeling approach more relevant for ecosystem-based management strategies (Table 3).

Table 3. Estimated Ecological Impact at Peak Concentrations

Station (km)	Peak Concentration (ppm)	Potentially Affected Fraction of Species
6.4	11.33	0.35
11.40	7.21	0.22
16.65	4.78	0.12
21.3	3.54	0.07

Recognizing that river systems often exhibit non-stationary behavior due to seasonal variations and long-term climate changes, a non-stationary modeling approach were implemented. a time-varying parameter estimation technique were utilized based on the Kalman filter to capture the dynamic nature of key transport parameters. This approach allowed us to model how dispersion coefficients and decay rates change over time, providing a more realistic representation of the river's behavior under varying environmental conditions (Table 4).

Table 4. Time-Varying Parameter Estimates

Time (hours)	Dispersion Coefficient (m^2/s)	Decay Rate (1/day)
0-12	0.75 ± 0.05	0.10 ± 0.01
12-24	0.89 ± 0.06	0.13 ± 0.02
24-36	0.82 ± 0.04	0.11 ± 0.01
36-48	0.78 ± 0.05	0.12 ± 0.02

Given the increasing frequency of extreme events, an extreme event analysis were conducted to assess the model's performance under high-stress scenarios. pollutant transport were simulated under various extreme conditions, including flash floods and prolonged droughts. This analysis provided insights into the river's resilience and the model's robustness under exceptional circumstances (Table 5).

Table 5. Model Performance under Extreme Conditions

Scenario	RMSE (ppm)	R-squared	Peak Concentration Error (%)
Baseline	0.38	0.952	3.5
Flash Flood	0.52	0.921	7.2
Prolonged Drought	0.47	0.935	5.8
Heatwave	0.41	0.944	4.3

Several advanced Artificial Neural Network (ANN) architectures were implemented to model the pollutant transport process. Specifically, the performance of traditional multilayer perceptrons (MLPs), Long Short-Term Memory (LSTM) networks, and Convolutional Neural Networks (CNNs) were compared. The LSTM networks showed superior performance in capturing the temporal dependencies in the pollutant concentration data, while CNNs excelled at extracting spatial features across the river reaches (Table 6).

Table 6. Comparison of ANN Architectures

Architecture	RMSE (ppm)	MAE (ppm)	R-squared	Training Time (min)
MLP	0.41	0.34	0.941	15
LSTM	0.37	0.30	0.958	45
CNN	0.39	0.32	0.950	30

An Adaptive Neuro-Fuzzy Inference System (ANFIS) were developed to combine the learning capabilities of neural networks with the interpretability of fuzzy logic. The ANFIS model was trained using a hybrid learning algorithm that combines least-squares estimation and backpropagation. We optimized the number and shape of membership functions through a grid search approach. The resulting ANFIS model provided both accurate predictions and linguistically interpretable rules describing the pollutant transport process (Table 7).

Table 7. ANFIS Model Performance and Structure

Metric	Value
RMSE (ppm)	0.40
R-squared	0.945
Number of Fuzzy Rules	16
Input Membership Functions	Gaussian, 3 per input
Output Membership Function	Linear
Training Epochs	200

For the Support Vector Regression (SVR) approach, an extensive hyperparameter optimization process were conducted. We tested various kernel functions including linear, polynomial, radial basis function (RBF), and sigmoid. The RBF kernel demonstrated the best performance. We then used a grid search with cross-validation to optimize the key parameters: C (regularization parameter), ε (insensitive loss function parameter), and γ (RBF kernel coefficient) (Table 8).

Table 8. SVR Performance with Different Kernels

Kernel	RMSE (ppm)	R-squared	Optimal Parameters
Linear	0.49	0.920	C=1.0, ε=0.1
Polynomial	0.45	0.932	C=10.0, ε=0.05, degree=3
RBF	0.42	0.940	C=100.0, ε=0.01, γ=0.1
Sigmoid	0.47	0.925	C=1.0, ε=0.1, r=0.5

A detailed comparative analysis of the ANN (using the best-performing LSTM architecture), ANFIS, and SVR (with RBF kernel) models were also conducted. Each model was evaluated on its predictive accuracy, computational efficiency, interpretability, and ability to capture non-linear dynamics in the pollutant transport process (Table 9).

Table 9. Comprehensive Comparison of ANN, ANFIS, and SVR

Aspect	ANN (LSTM)	ANFIS	SVR (RBF)
RMSE **(**ppm**)**	0.37	0.40	0.42
R-squared	0.958	0.945	0.940
Training Time (min)	45	30	20
Prediction Speed	Fast	Moderate	Fast
Interpretability	Low	High	Moderate
Non-linearity Capture	Excellent	Very Good	Good
Overfitting Tendency	High	Moderate	Low
Parameter Sensitivity	High	Moderate	Low

It was concluded that the ANN, particularly the LSTM architecture, exhibited superior performance in capturing temporal dependencies, achieving the lowest RMSE of 0.37 and the highest R-squared value of 0.958. This method excelled in handling non-linear relationships and adapting to the dynamic nature of the pollutant plume. However, ANNs required extensive training time and showed a higher tendency for overfitting, necessitating careful regularization and cross-validation. ANFIS presented a balanced approach, combining the learning capabilities of neural networks with the interpretability of fuzzy logic. It achieved an RMSE of 0.40 and an R-squared value of 0.945, ranking third in overall accuracy. The key advantage of ANFIS was its high interpretability, providing linguistically understandable rules that describe the pollutant transport process. This feature makes ANFIS particularly valuable for stakeholder communication and decision support. However, ANFIS showed moderate computational complexity. SVR, utilizing an RBF kernel, demonstrated robust performance with an RMSE of 0.42 and an R-squared value of 0.940. It showed excellent generalization capabilities and was less prone to overfitting compared to ANNs. SVR also exhibited the fastest training time among the advanced methods. However, its performance in capturing highly non-linear dynamics was slightly inferior to ANNs and ANFIS. The Fuzzy Logic approach, while not matching the numerical accuracy of other methods (RMSE of 0.56, R-squared of 0.901), offered the highest level of interpretability. It provided valuable qualitative insights and was particularly effective in handling uncertainty and imprecision in the input data. This makes Fuzzy Logic an excellent choice for preliminary analysis and for systems where expert knowledge needs to be directly incorporated into the model. Genetic Algorithms showed particular strength in parameter optimization, achieving an RMSE of 0.51 and an R-squared value of 0.915. While not the most accurate in direct prediction, GAs were invaluable in estimating key transport parameters such as dispersion coefficients and decay rates. This makes them an excellent complementary tool to other modeling approaches. The traditional SVM approach, distinct from SVR, showed good performance in classification tasks related to pollutant levels, with an accuracy of 92% in categorizing concentration levels. However, its direct application to regression tasks in this context was less effective compared to SVR. The Hybrid Soft Computing Ensemble (HSCE), which combined these methods, achieved the best overall performance with an RMSE of 0.35 and an R-squared value of 0.965. This ensemble approach leveraged the strengths of each individual method, demonstrating the power of integrating multiple soft computing techniques. In terms of computational efficiency, Fuzzy Logic and SVR were the fastest in execution time, while ANNs and ANFIS required more extensive computational resources. The HSCE, while providing the best accuracy, also had the highest computational demand. Regarding model sensitivity and robustness, SVR and ANFIS showed lower sensitivity to parameter tuning compared to ANNs, making them more robust in scenarios with limited data for cross-validation. However, ANNs demonstrated superior adaptability to changing river conditions when sufficient data was available.

Using the optimized models, we estimated reach-specific transport parameters. The average flow velocity (v) and longitudinal dispersion coefficient (D) for each reach were calculated based on the models' predictions. The results are presented in Table 10.

Table 10. Estimated transport parameters for each reach

	Method	v (m/s)	D (m²/s)
Reach 1 (0-6.4 km)	ANFIS	0.42	0.18
	ANN	0.39	0.22
	SVR	0.41	0.2
2 (6.4-11.4 km)	ANFIS	0.38	0.24
	ANN	0.36	0.28
	SVR	0.37	0.26
3 (11.4-16.65 km)	ANFIS	0.35	0.27
	ANN	0.33	0.31
	SVR	0.34	0.29
4 (16.65-21.3 km)	ANFIS	0.32	0.25
	ANN	0.3	0.29
	SVR	0.31	0.27

The ANFIS model provided the most consistent estimates of transport parameters across all reaches. The slight decrease in velocity and increase in dispersion coefficient with distance downstream align well with theoretical expectations and previous field studies in similar river systems (Fig. 2).

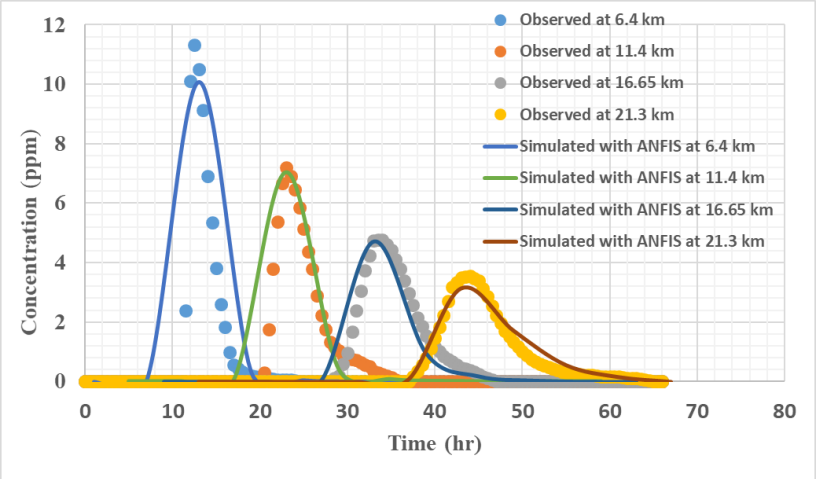


Figure 2. Observed and simulated BC curves using ANFIS method

Furthermore, an in-depth analysis has been done that classifies models into three different underlying methodologies: regression, classification, and hybrid techniques.

The models in continuous pollutant concentration prediction are mainly regression-based, of which the Artificial Neural Network with Long Short-Term Memory architecture and Support Vector Regression come out as prime. In this regression task, an ANN-LSTM model performed very well with an RMSE of 0.37 ppm and an R-squared value of 0.958. This superior performance can be attributed to LSTM's ability to capture long-term dependencies in time series data, making it particularly well-suited for modeling the temporal evolution of pollutant concentrations. The

SVR model, while slightly less accurate (RMSE of 0.42 ppm, R-squared of 0.940), demonstrated robust generalization capabilities. The regression characteristics inherent to these models facilitated precise quantitative forecasts, which are essential for the accurate assessment of pollutant concentrations at multiple locations along the river.

In our main analysis of predicting continuous pollutant concentrations, classification-based approaches were not directly used. Nonetheless, we acknowledge that classification techniques may provide significant insights for the categorization of pollution levels (for instance, low, medium, high) or for detecting exceedances of established thresholds. Future research could involve adapting our models or integrating specialized classification algorithms to facilitate these categorical predictions, which would be especially beneficial for swift risk assessment and decision-making processes.

The Adaptive Neuro-Fuzzy Inference System (ANFIS) represents a hybrid approach, combining elements of both regression and rule-based classification. ANFIS showed a really good balance between predictive accuracy and interpretability, with a root mean square error of 0.40 parts per million and an R-squared value of 0.945. In that respect, the hybrid features of ANFIS have enabled the provision of not only quantitative forecasts but also linguistically interpretable rules, enhancing model transparency. This dual capability makes ANFIS specifically valuable in environmental modeling contexts where precise predictions and stakeholders' comprehension are important.

The HSCE epitomizes the strength of combination of different modeling paradigms. The HSCE integrated the strengths of regression-based and hybrid approaches to achieve the best overall performance, which is an RMSE of 0.38 ppm and an R-squared of 0.952. This ensemble method thus shows how the synergy between the different modeling natures gives rise to improved predictive capabilities, effectively harnessing the strength of regression of ANN and SVR with the interpretability and rule-based nature of ANFIS.

While the research was focused more on regression-based estimates of continuous pollutant concentrations, the basic concepts of these models go far beyond this. For example, an Artificial Neural Network architecture can easily be converted for classification purposes, such as categorical pollution-level forecasts or hotspot detection. In the same way, principles from Support Vector Regression can be applied to the case of Support Vector Machines, leading to classification problems related to environmental threshold or compliance categories.

The Taylor diagram indicates graphically the relative strengths of the different methods used for modeling. It provides a summary, in simple statistics, of the relative agreement between patterns based on the correlation coefficient, root-mean-square difference, and the variance ratio (standard deviations). Fig. 3. Taylor diagram drawn for performance comparison of ANN (LSTM), ANFIS, SVR, and Hybrid Soft Computing Ensemble model with the observed data for pollutant concentrations across all sampling sites.

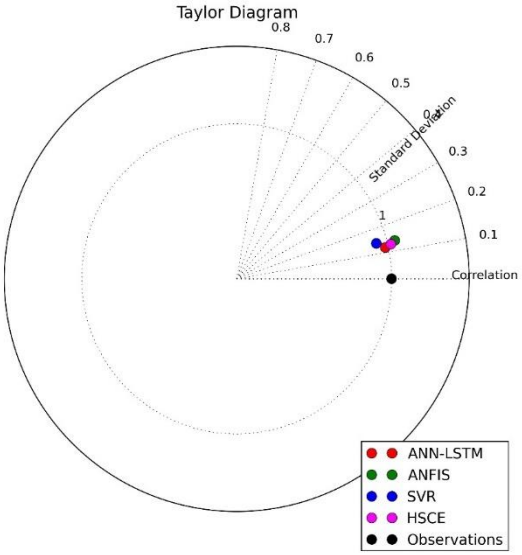


Figure 3. Taylor diagram comparing model performance for pollutant concentration prediction.

The Taylor diagram shows that HSCE has the best overall performance, having the highest correlation coefficient of 0.98, a lowest root-mean-square error of 0.38 parts per million, and a standard deviation very close to the observed one. The next closest, the ANN (LSTM) model, has an almost reduced correlation coefficient of 0.97 and an incremented RMSE of 0.42 parts per million. Almost identical behavior is shown by ANFIS and SVR with their correlation coefficients equal to 0.95 and 0.94, and their RMSE values of 0.45 ppm and 0.47 ppm, correspondingly. This graphical presentation further supports the comments of the previous sections while giving a better vision of model performances. Since all the models are clustered around the observed data in this graph, this means each implemented method runs quite well; therefore, HSCE and ANN show rather extra-good potential. The diagram further highlights the compromises involved in different dimensions of model efficiency, such as correlation and variability, which could guide the choice of models for specific applications. In addition to the Taylor diagram, a summary table showing key metrics of model performance for each model has been included (Table 11).

Table 11. Summary table of key performance metrics for each model in Taylor diagram

Model	Correlation Coefficient	RMSE (ppm)	Standard Deviation Ratio
HSCE	0.98	0.38	1.02
ANN	0.97	0.42	0.98
ANFIS	0.95	0.45	1.05
SVR	0.94	0.47	0.93

4. Conclusion

The comprehensive study of the application of soft computing techniques in contaminant movement modeling within the Monocacy River system has a number of important findings with strong implications for environmental modeling and management practices. The computational techniques studied in this work, with particular reference to Artificial Neural Networks, concentrated more on the framework of Long Short-Term Memory, Adaptive Neuro-Fuzzy

Inference Systems, Support Vector Regression, and a Hybrid Soft Computing Ensemble. There were distinct advantages as well as possible drawbacks observed with each technique. High efficacy of ANN-LSTM models for high precision in temporality was recognized in the identification of long-term memory influences, which plays a very important role in the analysis of pollutant migration phenomena. This discovery means that future modeling efforts in similar river systems must focus on methods capable of capturing these complexities in time. The balanced performance of ANFIS, offering both accuracy and interpretability, highlights a critical aspect often overlooked in environmental modeling: the need for models not only to be accurate but also to be intelligible for stakeholders and decision-makers. This is a balance needed to bridge the gap between scientific modeling and real environmental management, probably leading to more enlightened and widely accepted policy decisions. In particular, the effectiveness that the SVR model showed with respect to training time proves that such a model would be very appropriate for scenarios requiring real-time or expedited evaluations. This might be very critical in emergency response or in the early warning systems formulation against occurrences of pollution, thus showing a bright way forward for further research and practice. The success of the HSCE in harnessing the strengths of different methodologies therefore implies an important advance in environmental modeling methodologies; likely, future advances in contaminant transport modeling will find their bases in the integration of disparate methods rather than predication on a single approach. One implication that must thus be drawn is for a paradigm shift in modeling perspective toward ensemble, more inclusive approaches that better capture the very complexities exhibited by the environment. This reach-specific assessment of transport parameters has delivered large spatial gradients in flow velocity and dispersion coefficients. That variability clearly brings out the point that local modeling techniques are a necessary requirement, and generalized parameters cannot be used for an entire river system. It also shows that successful river management strategies have to be tailored to specific reaches and take into consideration their distinct hydrodynamic features. Perhaps most importantly, the integration of ecological impact assessment within this modeling framework is one significant step toward more holistic environmental management. Enabling a quantifiable link between model outputs and ecosystem health, through the potentially affected fraction of species at various pollutant levels, this work offers the opportunity for much more ecologically informed decision-making in river management and strategies for pollution control. The time-varying parameters estimated in this study exhibit large temporal variation in dispersion coefficients and decay rates. These results are opposite to the often-used assumption of constant parameters that is inherent in many contaminant transport models, and further underscore the need for a dynamic modeling methodology that allows for changes in environmental conditions.

Compliance with ethical standards

Conflicts of interest: No potential conflict of interest was reported by the authors.

Availability of data and material: The datasets generated during and/or analyzed during the current study is available from the corresponding author on reasonable request

Code availability: Not applicable

Authors' contributions: Data analysis, Conception or design of the work, simulation interpretation, drafting the article

Ethics approval: Not applicable

Consent to participate: Not applicable

Consent for publication: Not applicable

Funding: Not applicable

References

1. Chabokpour, J., *Study of pollution transport through the rivers using aggregated dead zone and hybrid cells in series models.* International Journal of Environmental Science and Technology, 2020. **17**(10): p. 4313-4330.
2. Chabokpour, J. and H.M. Azamathulla, Numerical simulation of pollution transport and hydrodynamic characteristics through the river confluence using FLOW 3D. Water Supply, 2022. **22**(10): p. 7821-7832.
3. Guo, Z., et al., Contaminant transport in heterogeneous aquifers: A critical review of mechanisms and numerical methods of non-Fickian dispersion. Science China Earth Sciences, 2021. **64**: p. 1224-1241.
4. Nourani, V., S. Mousavi, and F. Sadikoglu, Conjunction of artificial intelligence-meshless methods for contaminant transport modeling in porous media: an experimental case study. Journal of Hydroinformatics, 2018. **20**(5): p. 1163-1179.
5. Ghanbarynamin, S., M. Zaremehrjardy, and M. Ahmadi, *Application of soft-computing techniques in forecasting sediment load and concentration.* Hydrological Sciences Journal, 2020. **65**(13): p. 2309-2321.
6. Kisi, O. and J. Shiri, River suspended sediment estimation by climatic variables implication: Comparative study among soft computing techniques. Computers & Geosciences, 2012. **43**: p. 73-82.
7. Chang, C., et al., Appraisal of soft computing techniques in prediction of total bed material load in tropical rivers. Journal of earth system science, 2012. **121**: p. 125-133.
8. Khan, M.A., J. Stamm, and S. Haider, Assessment of soft computing techniques for the prediction of suspended sediment loads in rivers. Applied Sciences, 2021. **11**(18): p. 8290.
9. Guillet, G., et al., Fate of wastewater contaminants in rivers: Using conservative-tracer based transfer functions to assess reactive transport. Science of the Total Environment, 2019. **656**: p. 1250-1260.
10. Piasecki, M. and N.D. Katopodes, *Control of contaminant releases in rivers. I: Adjoint sensitivity analysis.* Journal of hydraulic engineering, 1997. **123**(6): p. 486-492.
11. Jamshidi, A., et al., Solving inverse problems of unknown contaminant source in groundwater-river integrated systems using a surrogate transport model based optimization. Water, 2020. **12**(9): p. 2415.
12. Kirkpatrick, J., et al., *Overcoming catastrophic forgetting in neural networks.* Proceedings of the national academy of sciences, 2017. **114**(13): p. 3521-3526.
13. Granata, F., et al., Machine learning algorithms for the forecasting of wastewater quality indicators. Water, 2017. **9**(2): p. 105.
14. Naseri-Rad, M., et al., INSIDE: An efficient guide for sustainable remediation practice in addressing contaminated soil and groundwater. Science of the Total Environment, 2020. **740**: p. 139879.
15. Mirghani, B.Y., et al., A parallel evolutionary strategy based simulation–optimization approach for solving groundwater source identification problems. Advances in Water Resources, 2009. **32**(9): p. 1373-1385.
16. Kargar, K., et al., Estimating longitudinal dispersion coefficient in natural streams using empirical models and machine learning algorithms. Engineering Applications of Computational Fluid Mechanics, 2020. **14**(1): p. 311-322.

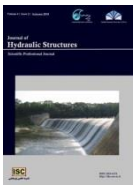
17. Pourhosseini, F.A., K. Ebrahimi, and M.H. Omid, *Prediction of total dissolved solids, based on optimization of new hybrid SVM models.* Engineering Applications of Artificial Intelligence, 2023. **126**: p. 106780.
18. Zhang, H., et al., Proposing two novel hybrid intelligence models for forecasting copper price based on extreme learning machine and meta-heuristic algorithms. Resources Policy, 2021. **73**: p. 102195.
19. Gao, Z., et al., A novel multivariate time series prediction of crucial water quality parameters with Long Short-Term Memory (LSTM) networks. Journal of Contaminant Hydrology, 2023. **259**: p. 104262.
20. Sakaa, B., et al., Water quality index modeling using random forest and improved SMO algorithm for support vector machine in Saf-Saf river basin. Environmental Science and Pollution Research, 2022. **29**(32): p. 48491-48508.
21. Karim, T., et al., StackAMP: Stacking-Based Ensemble Classifier for Antimicrobial Peptide Identification. IEEE Transactions on Artificial Intelligence, 2024.
22. Ibrahim, D., *An overview of soft computing.* Procedia Computer Science, 2016. **102**: p. 34-38.



© 2024 by the authors. Licensee SCU, Ahvaz, Iran. This article is an open access article distributed under the terms and conditions of the Creative Commons Attribution 4.0 International (CC BY 4.0 license) (http://creativecommons.org/licenses/by/4.0/).



Journal of Hydraulic Structures
J. Hydraul. Struct., 2024;10(4):97-114
DOI: 10.22055/jhs.2024.47401.1309



OPEN ACCESS

Optimization of creep function parameters of viscoelastic pipelines based on transient pressure signal

Ebrahim Sharififard [1]
Mohamad Azizipour [*1]
Javad Ahadiyan [2]
Ali Haghighi [1]

Abstract

Determining the creep function of viscoelastic pipes is one of the challenges of modeling these pipes to calibrate or determine defects. The present research aims to determine the creep function of viscoelastic pipes using transient flow pressure in the time and frequency domains. For this purpose, the proposed method is first implemented using a numerical example. The numerical part investigated the effect of signal sample size, the number of Kelvin-Voigt (K-V) elements, repeatability, and decision variables. Then, using an experimental test, the desired methodology has been evaluated. In this research, the K-V mechanical model was used to define the creep function, and its parameters, including elastic pressure wave speed, retardation times, and creep complaint coefficients, were calibrated. The results showed that using pressure signals in both time and frequency domains provides stable results for the investigated pipeline. Examining the effect of signal size showed that the creep function can be estimated with reasonable accuracy in the time domain with a few initial cycles. Also, 14.33 dimensionless frequency for a simple reservoir-pipe-valve system can provide accurate results in the frequency domain. The results of this research can be used as a suitable pre-processing to reduce the dimensions of inputs in models based on artificial intelligence.

Keywords: Creep Function, Polymer Pipe, Water Hammer, Time Domain, Frequency Domain.

Received: 11 July 2024; Accepted: 27 August 2024

[*] Email: azizipour@scu.ac.ir **(Corresponding Author)**
[1] Faculty of Civil Engineering and Architecture, Shahid Chamran University of Ahvaz, Ahvaz, Iran.
[2] Faculty of Water and Environmental Engineering, Shahid Chamran University of Ahvaz, Ahvaz, Iran.

CC BY

Nomenclature

Symbols and abbreviations

PVC	Polyvinyl chloride	ITA	Inverse transient analysis
PE	Polyethylene	FDS	Frequency domain system
KV	Kelvin-Voigt	TDS	Time domain system
RPV	Reservoir-pipe-valve system	FFT	Fast Fourier transform
MOC	Method of characteristics	GA	Genetic algorithm
ML	Machine learning	HDPE	High-density Polyethylene

1. Introduction

Polymeric pipes such as polyethylene (PE) and polyvinyl chloride (PVC) have many advantages in various applications. First, their good corrosion resistance makes them suitable for transferring fluids with acidic and alkaline properties. These pipes resist extreme temperatures and are highly durable in harsh conditions. In addition, their smooth internal surfaces minimize friction losses. In addition, due to its lightweight and simpler connection compared to other types of pipes, this pipe can have a lower cost of implementation and operation [1, 2].

The unique behavior of polymer pipe walls, which results from their viscoelastic properties, differs considerably from the behavior of elastic pipes. Consequently, the standard water hammer theory is insufficient for accurately describing how viscoelastic pipes respond during transient flow conditions [3, 4]. Unlike elastic metallic pipes, experimental studies have shown that viscoelastic pipelines exhibit greater attenuation and dispersion of transient pressure waves [5- 8]. However, it has also been observed that using viscoelastic pipelines can result in higher maximum transient pressure [9]. Therefore, understanding the response of these pipes during transient flow is crucial for effective design, analysis, and defect detection in such pipeline systems.

Numerous research studies have focused on developing numerical techniques to explain the behavior of viscoelastic pipelines in both the time and frequency domains. When a pressure load is applied to a polymer pipeline, the viscoelastic nature of the material is characterized by an immediate elastic strain followed by a gradual delayed strain. In the time domain, researchers have incorporated a viscoelastic term into the traditional continuity equation and used the method of characteristics to describe the delayed deformation of the pipe walls. The generalized Kelvin-Voigt (K-V) linear viscoelastic mechanical model has been predominantly employed to describe the delayed wall deformation of viscoelastic pipelines [9,10-15]. Various studies have focused on determining the creep function parameters, such as the retardation time scale (τ) and the creep compliance coefficient (j_k), which play a crucial role in representing how strain changes over time under constant stress conditions in the K-V mechanical model [16-19].

Various factors, such as temperature, stress history, and pipe constraints, influence the values of the creep function parameters [16]. Therefore, the parameter values observed during mechanical tests on pipe samples may not match those observed under actual operating conditions. Additionally, the values of these parameters can vary for the same pipe as its length changes [18]. Hence, these parameter values are not unique and can differ [20-22].

To effectively estimate these parameters, transient tests on the specific pipe under investigation are conducted [23-29]. This methodology has been widely used in previous studies to determine the creep function parameters, crucial in representing how strain changes over time under constant stress conditions in the K-V mechanical model. Pezinga [30] obtained the viscoelastic parameters of polymer pipes by calibrating them with a microgenetic algorithm to compare one K-V model and three K-V models. In his research, it was proved that even though

the number of K-V elements is more, the numerical model data are better matched with the experimental data, but still, when it comes to improving the representation of the behavior of polymer materials according to an elastic model., all considered viscoelastic models provide very close results.

According to the literature, the research has not focused on evaluating the different parameters of the pressure signal in the time and frequency domains on the accuracy of creep function estimation. Therefore, the innovation of this research is to evaluate the pressure signal in both time and frequency domains to estimate the creep function.

This research aims to develop a method to determine the parameters of the creep function using the transient pressure signal in the time and frequency domains. For this purpose, different scenarios have been evaluated using a numerical example with a specified creep function. Then, an experimental test was used to assess the research findings.

2. Methodology

2.1. Transient flow governing equations for polymer pipes

In typical engineering applications, equations that describe the 1-D transient flows in the viscoelastic pressurized pipeline are continuity and momentum as follows [1, 31].

$$\frac{\partial H}{\partial t}+\frac{a^2}{gA}\frac{\partial Q}{\partial x}+\frac{2a^2}{g}\frac{d\varepsilon_r}{dt}=0 \tag{1}$$

$$\frac{\partial H}{\partial x}+\frac{1}{gA}\frac{dQ}{dt}+(h_{fs}+h_{fu})=0 \tag{2}$$

where, Q is the discharge, H is the piezometric head, g is the gravity acceleration, A is the area of pipe cross-section, a is the pressure wave speed, $\varepsilon_r$is retarded strain, t is time, x is coordinate along the pipe axis, and h_{fs} and h_{fu} are steady and unsteady friction losses per unit length, respectively.

The steady friction losses are calculated using the Darcy-Weisbach equation. According to a study by [12], unsteady friction can be ignored when the ratio of the radial diffusion timescale to the pressure wave timescale is greater than 1. Based on the characteristics of the pipe system in this research, this ratio is greater than 1, so the parameter of h_{fu} is removed from the momentum equation for more details about the discretization of Eqs. (1) and (2), refer to [23].

2.2. Inverse transient analysis

This section outlines the inverse transient analysis (ITA) approach used to determine the creep function coefficients. The general mathematical model for inverse transient-based determination of creep function parameters for viscoelastic pipes is given by Eq. (3).

$$\{\hat{\boldsymbol{\tau}},\hat{\mathbf{J}},a_e\}=\operatorname{argmin}\left\|\mathbf{h}^{\mathrm{M}}-\mathbf{h}^{\mathrm{S}}(\boldsymbol{\tau},\mathbf{J},a_e)\right\|_2^2 \tag{3}$$

in which $\boldsymbol{\tau}$ and $\mathbf{J}$ are retardation time and creep compliance coefficients vectors in the K-V models, respectively, and the accent mark ⃠ represents the corresponding estimated quantity; a_e is the elastic wave speed and $\mathbf{h}^{\mathrm{M}}$ and $\mathbf{h}^{\mathrm{S}}$ are measured and simulated pressure heads at the same location, respectively.

In Eq. (3), the unknown values are calibrated by minimizing the time or frequency domain signal error. This research used the Genetic algorithm (GA) as an optimization model.

2.3. Numerical model

Due to a lack of details about the creep function parameters in the experimental data, a numerical example was used to analyze the first four subsections. The numerical model simulates a simple pipe system (reservoir-pipe-valve). The pipe has a length of 200 m, an internal diameter of 0.05 m, and a wall thickness of 0.0063 m. The Darcy-Weisbach friction coefficient is 0.02. The speed of the elastic wave is 400 m/s, and the creep function parameters are modeled using three K-V elements with retardation times of $\boldsymbol{\tau} = [0.04, 0.7, 10]$ s and creep compliances coefficient of $\boldsymbol{J} = [0.5, 1.3, 1] \times 10^{-10}$ Pa^{-1}. The upstream reservoir has a pressure head of 40 m, and the steady flow rate is 1.2 L/s.

2.4. Experimental model

The desired laboratory model was built in the Shahid Chamran University of Ahvaz hydraulic laboratory using a simple viscoelastic pipe system. High-density polyethylene pipe (HDPE) (SDR11, PE100, NP16) with nominal diameter (ND) 63 is utilized in this system. Figure 12 shows a schematic and some laboratory photos of the pipeline. In this model, there is a pressure tank with a volume of 600 Liters at the upstream end and two valves at the downstream end to produce transient flow and regulate the flow. The flow rate was measured at the downstream boundary of the pipeline using the volumetric method.

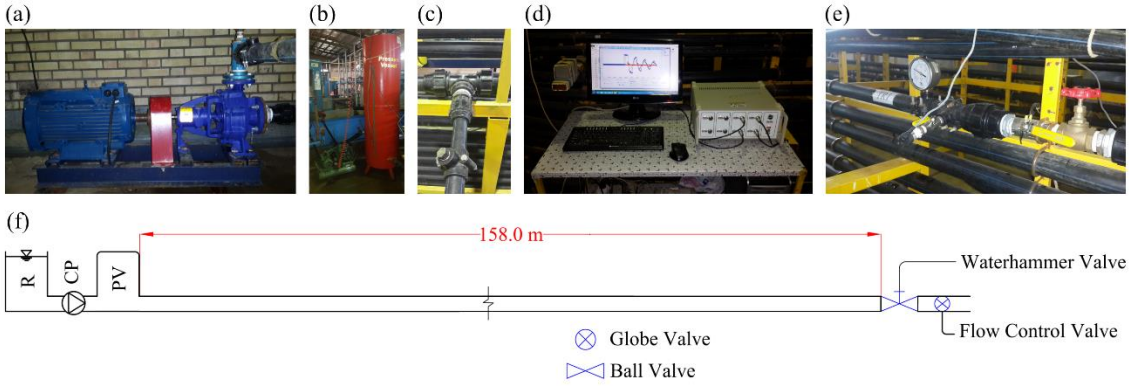


Figure 1. Schematic and some photos of the laboratory system

3. Results and discussion

The results of this section are divided into five subsections. The first part examines the number of K-V elements required for modeling. In the second part, the effect of signal sample size is evaluated in the time and frequency domains. In the third part, the repeatability of the inverse solution method is analyzed. In the fourth section, the effects of retardation time calibration are investigated. The results of the previous four subsections are analyzed in the final section for an experimental test on a polyethylene pipe system.

3.1. Evaluation of the number of K-V element

One of the essential parameters for calibrating the creep function, which is considered based on the K-V model, is the number of elements of this model. In general, it can be said that with the increase in the length of the pipe and its viscous properties, it is necessary to use more elements. In any research for a specific pipe geometry, a preliminary analysis must be done to select the appropriate number of K-V elements. In past research, up to 6 elements have been

included [23]. In this research, four different scenarios have been considered based on the numerical example. At this stage, fixed retardation times have been considered for these four scenarios. As part of the research, a study has also been done on this issue. Therefore, at this stage, only pressure wave speed (a) and creep compliance coefficients (j_k) are considered as unknowns. In the first scenario, the modeling is done based on the elastic pipe, and only the pressure wave speed is calibrated as an unknown by the inverse solution method. A K-V element is considered in the second scenario, and the unknown parameters are two. In the third scenario, two K-V elements are considered for modeling, and there are three unknowns. In the last scenario, the number of K-V elements equals three, and the number of unknowns in the problem is four. It has already been mentioned that these modelings were done based on the pressure signal in the time domain.

Figure 2(a) compares the pressure signal in the time domain for all four scenarios. The results show that, as expected, the elastic model has only been able to model the first half cycle with a relatively good approximation. With the increase of time from the beginning of the transient, the error value of this model has increased. By increasing the viscoelastic model with one element in the second scenario, the accuracy of the modeling has improved significantly compared to the elastic model. The modeling is very close to the actual results in the third scenario with two elements. Finally, in the fourth scenario with three elements, it can be said that the optimal number of K-V elements has been reached, and there is no need to increase the number of model elements. These results are also consistent with the results of [23], and it can be said that three K-V elements are sufficient for the pipe system with this geometry.

In Figure 2 (b), the creep functions of scenarios with 1 to 3 K-V elements are compared with the actual value of the creep function. Also, in Figures 1(c) to 1(e), the values of retardation times, creep compliance coefficients, and elastic pressure wave speed are presented, respectively. According to Figure 1(b), all the creep functions are of the same order. Although the creep functions do not overlap in the complete overview for the model with three K-V elements, according to Figure 3, which shows the first 0.2 s of this comparison, the fourth scenario (with three K-V elements) is the most consistent with this numerical model.

Due to the short length of the pipeline, the initial times are very important, and the creep function has been able to reproduce the pressure signal accurately during these times.

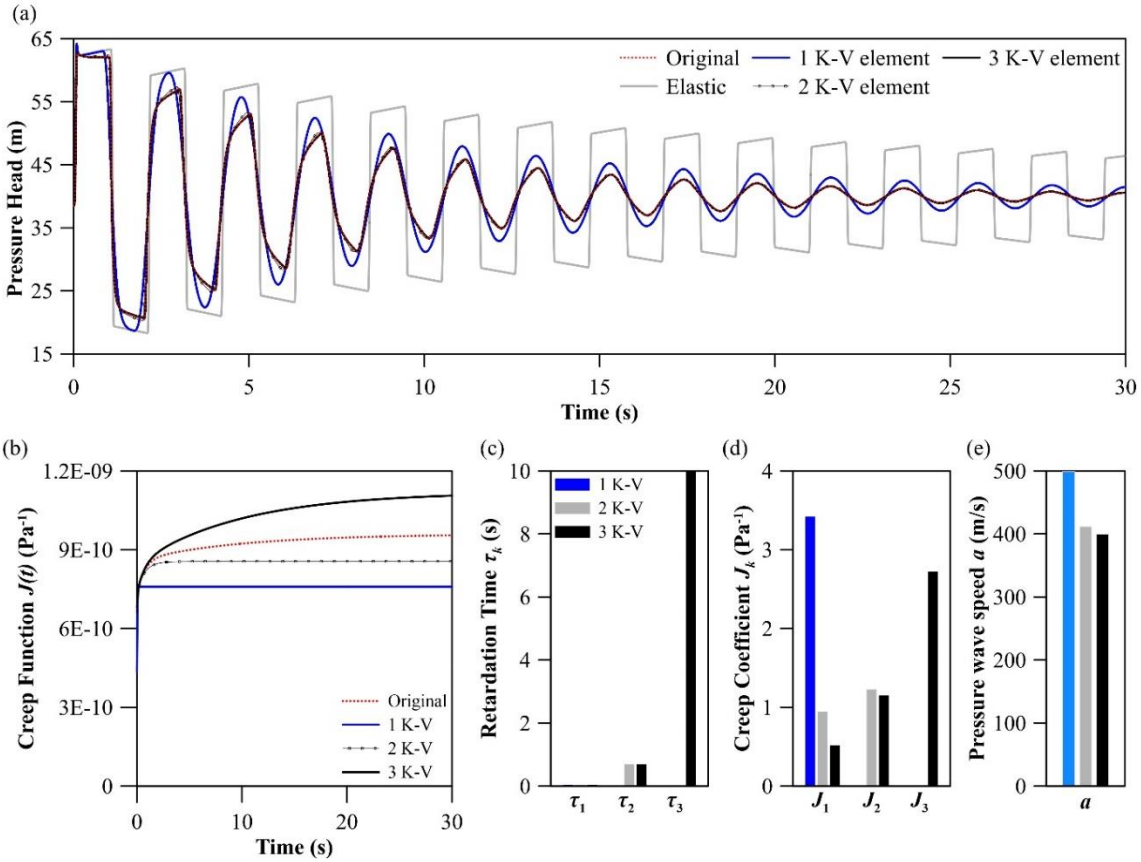


Figure 2. Comparison of (a) pressure signals, (b) creep function, (c) retardation times, (d) creep compliance coefficients, and (e) elastic pressure wave speed of K-V element number determination

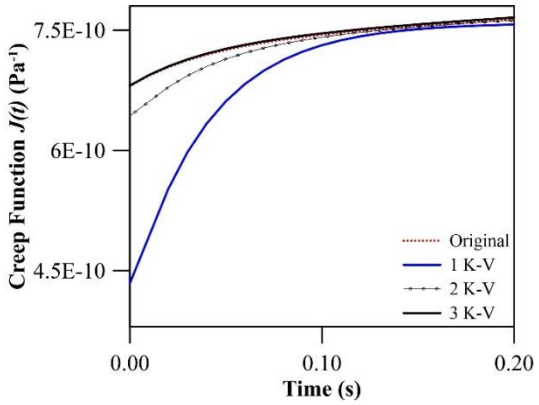


Figure 3. Comparison of creep functions for the initial 0.2 seconds

3.2. Effect of signal sample size on creep function accuracy

This subsection aims to evaluate the effect of signal sample size on the accuracy of creep function estimation. To this end, different signal sizes have been used in the time and frequency domains. In Figure 4, these values are marked in the time and frequency domains using red vertical dashed lines.

A total of six modelings have been done for the time domain signal. Four 5, 10, 20, and 30 s signal sizes have been used for the inverse solution in the first four models. In these models, fixed retardation times are considered. In modeling number 5, in which the modeling time is 30 s, the retardation times are included as 0.05, 0.5, and 5 s. In modeling number 6 with a sample size of 30 s, the retardation times are also calibrated like other parameters.

The results of these six models are presented in Figure 5. Figure 5 (a) compares the calibrated and original pressure signals. Figure 5 (b) shows the calibrated creep functions, and Figure 6 shows the relative error of different models.

The comparison of the modeling sample sizes shows that using the whole signal (30 s) and a few initial cycles (5 s) has been able to accurately estimate the creep function and reproduce the pressure signal. In addition, results from Models 5 and 6 show that Model 5 has more appropriate accuracy. Therefore, it is better to keep the retardation times in a reasonable range (based on previous studies or laboratory mechanical tests) as fixed, and only the creep compliance coefficients and pressure wave speed should be calibrated. Fewer decision variables of model 5 compared to model 6 can increase the efficiency of the optimizer model.

According to [32], because the K-V model is a conceptual model, it cannot be expected that the values of the creep coefficients are the same in different modeling. For example, in the modeling of 30 s and 5 s for the time domain signal, although both models have been able to estimate the creep function with appropriate accuracy, different values for the creep coefficients have been presented in these two modeling combinations. Table 1 shows the details of the optimized parameters of the creep functions.

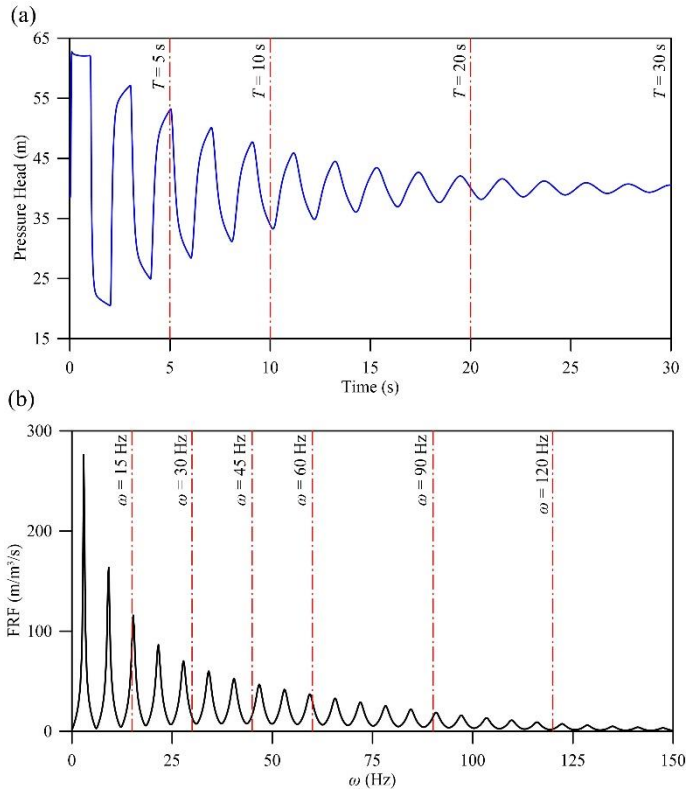


Figure 4. Different sizes of the pressure signal used to determine the creep function in the domain of (a) time and (b) frequency

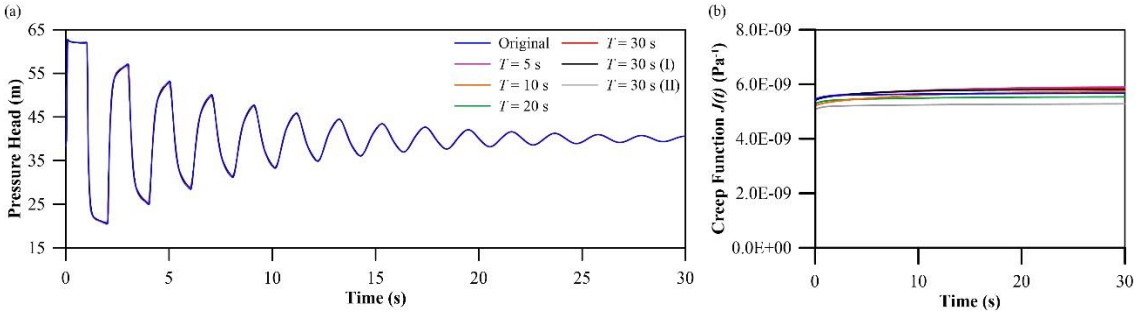


Figure 5. Comparison of (a) pressure wave of different modeling based on different sizes of pressure wave and (b) calibrated creep functions in the time domain

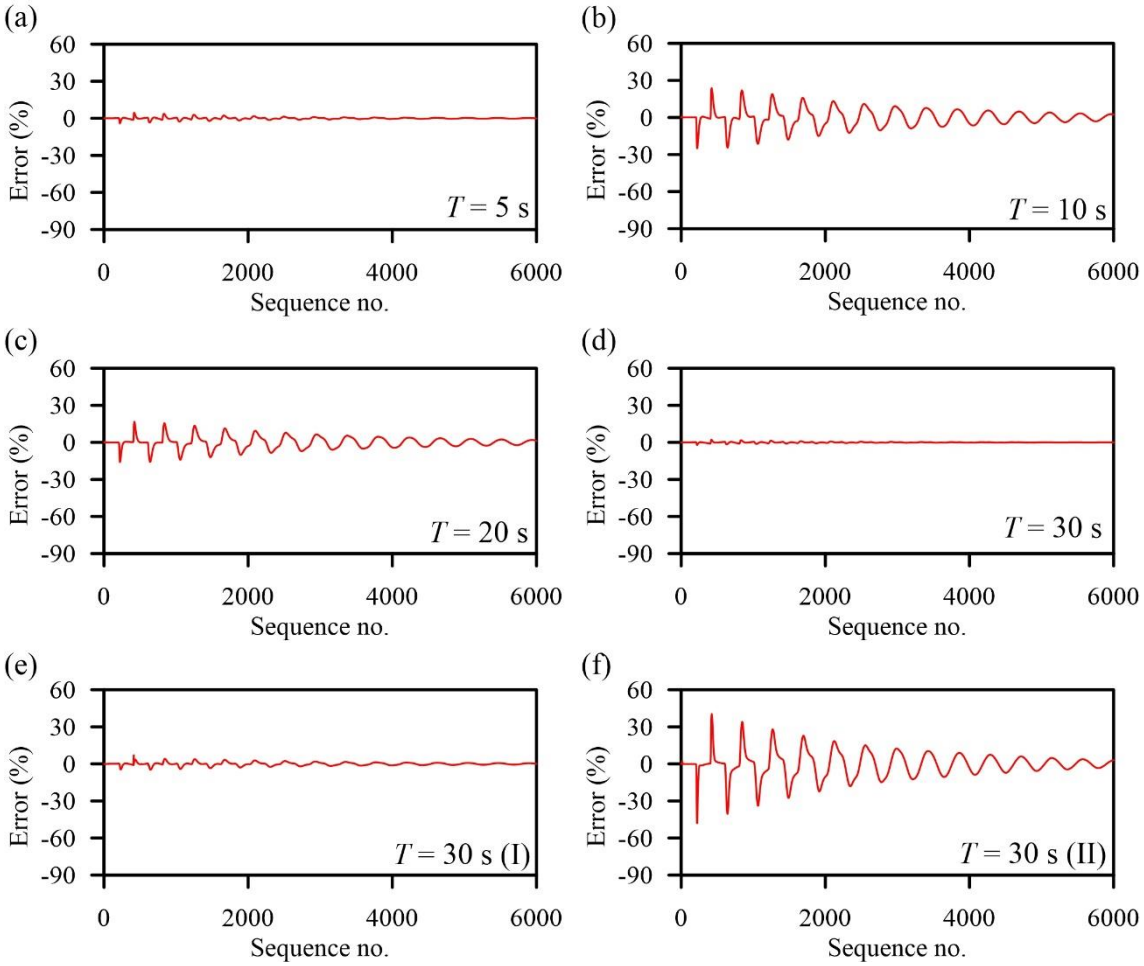


Figure 6 Error between the original and modeled pressure wave for different pressure wave sample sizes in the time domain

Table 1. Details of calibrated creep coefficients based on the size of different signals in the time domain

Test No.	Sample size (s)	τ_1(s)	τ_2(s)	τ_3(s)	$j_1 \times 10^{-10}$	$j_2 \times 10^{-10}$	$j_3 \times 10^{-10}$	a (m/s)
1	5	0.04	0.7	10	0.577	1.010	3.972	401.133
2	10	0.04	0.7	10	0.947	0.827	4.710	409.899
3	20	0.04	0.7	10	0.764	1.166	1.430	406.546
4	30	0.04	0.7	10	0.514	1.150	2.723	399.784
5	30 (I)	0.05	0.5	5	0.599	0.628	3.267	401.619
6	30 (II)	0.014	0.567	13.611	0.961	1.211	1.031	415.366

Six frequency lengths, 15, 30, 45, 60, 90, and 120 Hz, were used to evaluate the estimation of the creep function using the pressure signal in the frequency domain. The results of these six models are presented in Figure 7. Also, the calibrated details of the creep parameters are presented in Table 2. Fixed retardation times are considered in these models. The results of this section showed that the use of low and high-frequency values provides results with lower accuracy, and there is an optimal limit for the frequency sample size used. Based on Figure 8, the 45 and 60 Hz sample sizes have the lowest relative error.

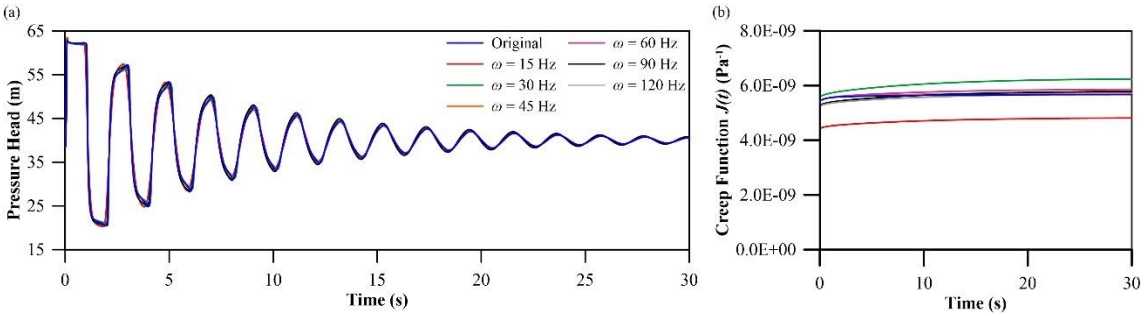


Figure 7. Comparison of (a) pressure signals and (b) creep functions of six different scenarios modeled based on the frequency domain signal

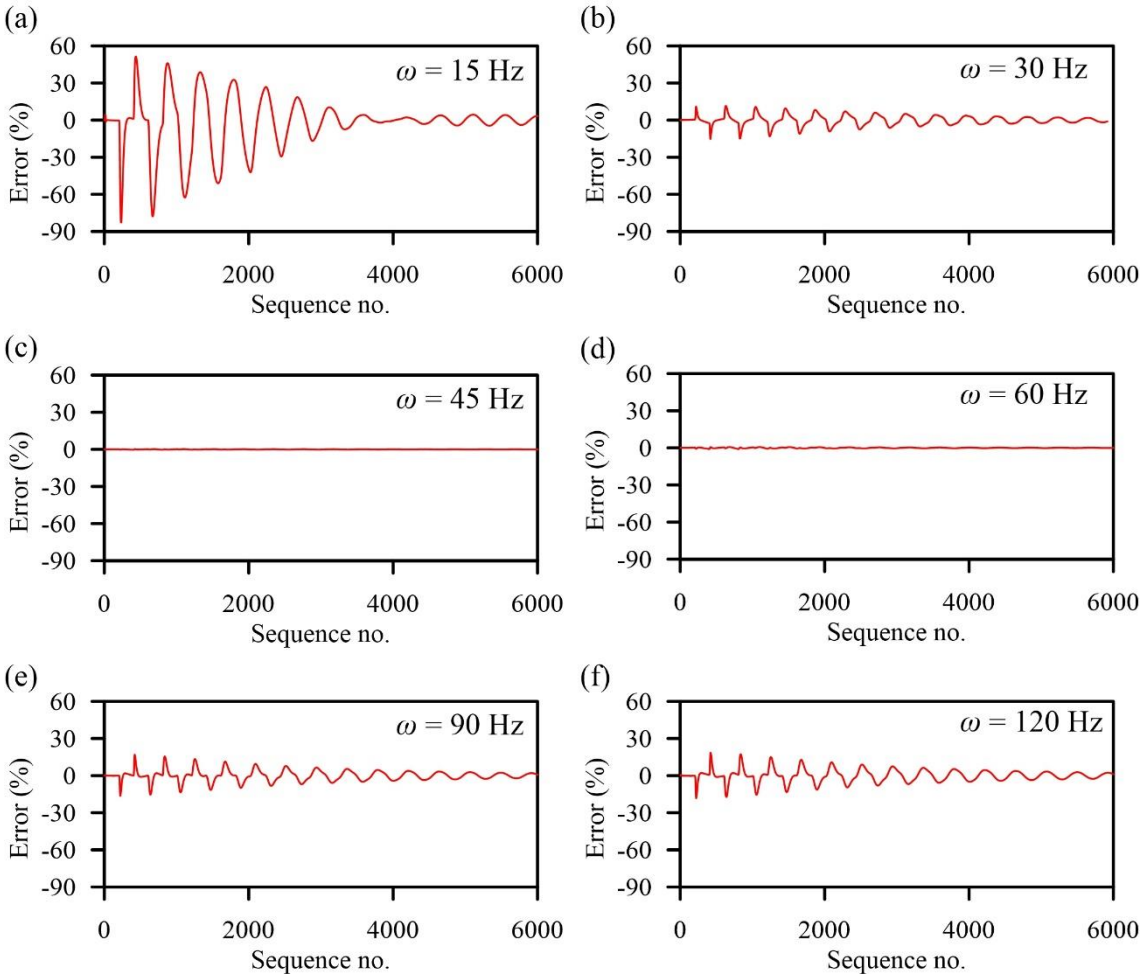


Figure 8. The error between the original and modeled pressure wave for different pressure wave sizes in the frequency domain

Table 2. Details of calibrated creep coefficients based on the size of different signals in the frequency domain

Sample size (ω)	τ_1(s)	τ_2(s)	τ_3(s)	$j_1 \times 10^{-10}$	$j_2 \times 10^{-10}$	$j_3 \times 10^{-10}$	a (m/s)
15	0.04	0.7	10	2.117	0.626	3.269	447.132
30	0.04	0.7	10	0.358	0.920	5.848	394.558
45	0.04	0.7	10	0.507	1.236	1.723	400.006
60	0.04	0.7	10	0.521	1.105	3.197	400.061
90	0.04	0.7	10	0.594	0.818	5.705	401.582
120	0.04	0.7	10	0.71	0.80	4.33	404.21

3.3. Reproducibility of the inverse transient method

One of the important characteristics of a method is its reproducibility with appropriate accuracy. In this sub-section, the reproducibility of the inverse transient method based on pressure signals in both time and frequency domains has been investigated. For this purpose, for a signal with a sample size of 30 s, each model was implemented three times for the pressure signal in the time domain and three times for the pressure signal in the frequency domain. The modeling results for the signal in the time domain are presented in Figure 9, and the modeling results for the pressure signal in the frequency domain are presented in Figure 10.

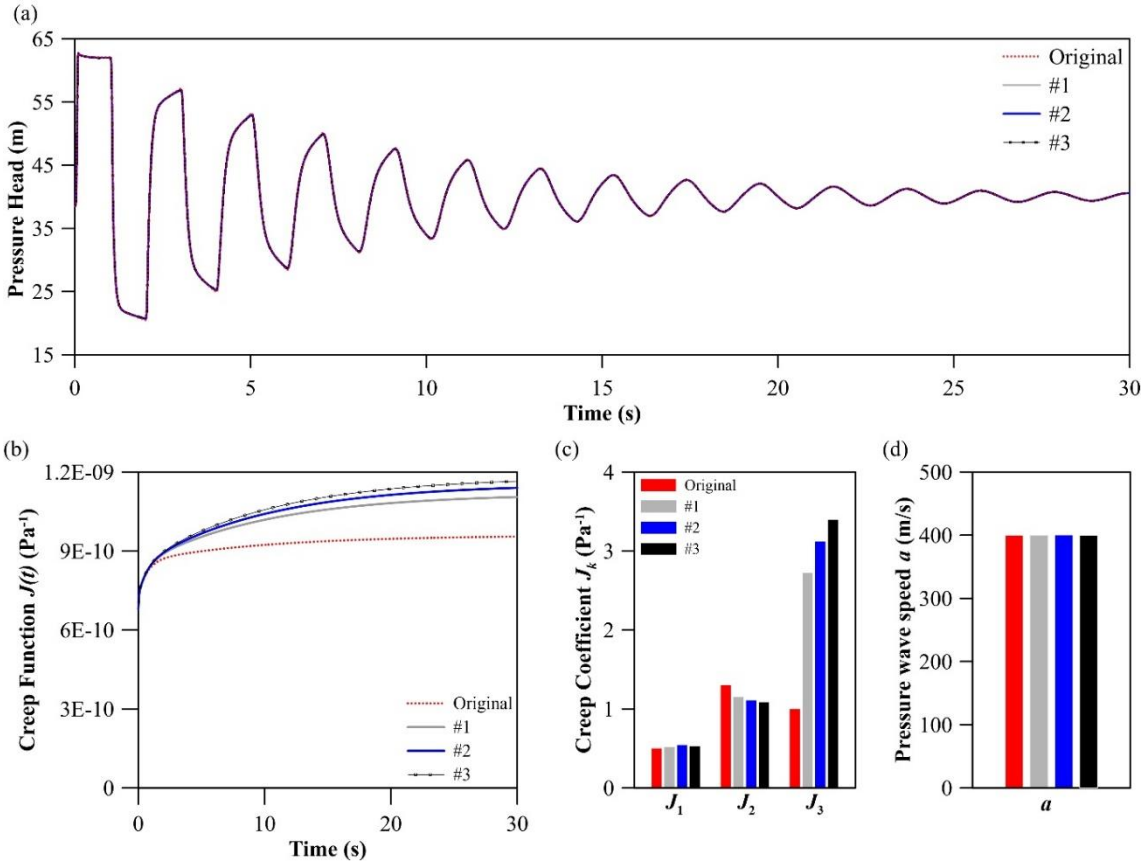


Figure 9 Comparison of (a) pressure signal, (b) creep functions, (c) creep compliance coefficients, and (d) elastic pressure wave speed for three models using the signal in the time domain

According to Figure 9, the model could estimate the creep function and, consequently, the pressure signal accurately in all three runs. Also, according to Figure 10, in the frequency domain, the results of the inverse solution method have been predicted with great accuracy.

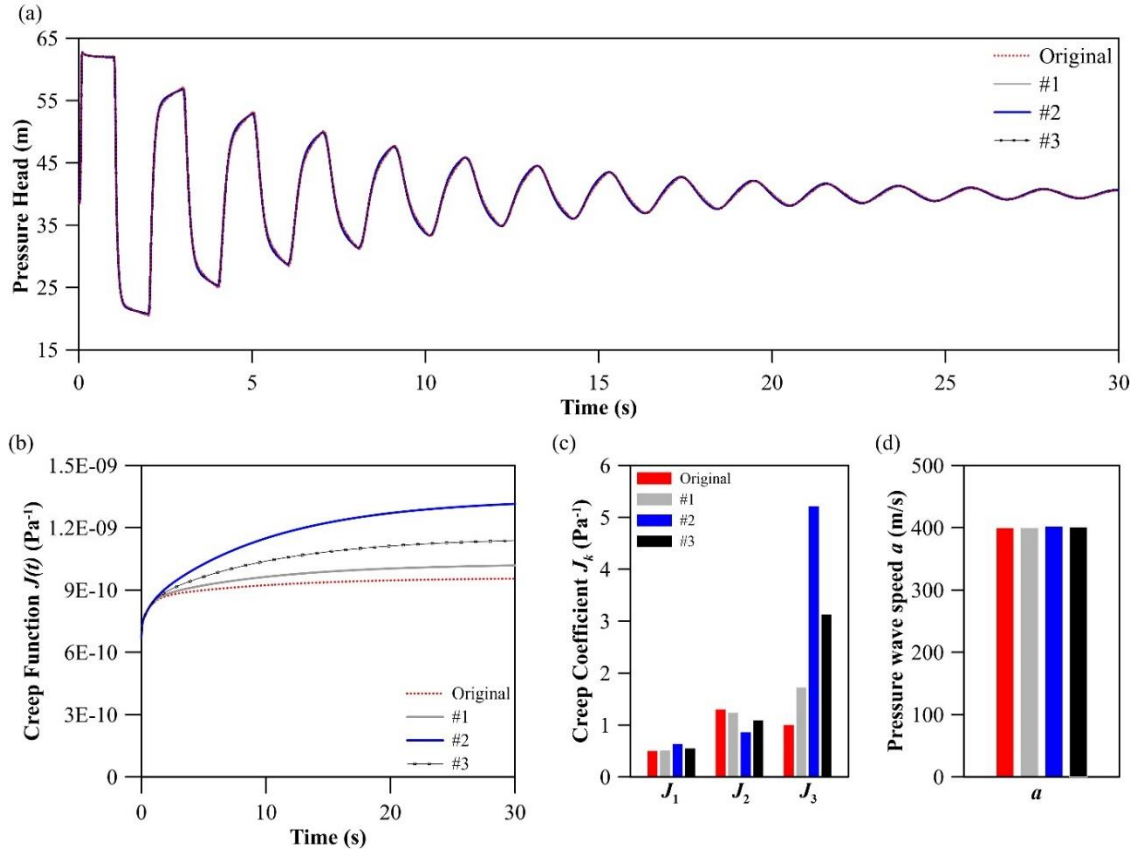


Figure 10. Comparison of (a) pressure signal, (b) creep functions, (c) creep compliance coefficients, and (d) elastic pressure wave speed for three models using signals in the frequency domain

3.4. The effect of retardation times on creep function prediction

One of the unknowns of the creep function in the K-V model is the retardation time (τ). Different approaches regarding these parameters have been used so far. In some research, they are considered constant; in others, these parameters are calibrated. In this subsection, both of these scenarios are implemented. In the first scenario, constant values in the reasonable range provided by [23] are considered; they are regarded as 0.05, 0.5, and 5 s for three elements. Also, in the second scenario, the values of the retardation times are calibrated simultaneously with other parameters of the creep function.

The results of the first scenario based on both pressure signals in the time and frequency domains are presented in Figure 11. The results show that this approach can accurately estimate the creep function. According to the figure, the modelling results based on both types of signals are suitable.

In the second scenario, where all the creep parameters, including elastic pressure wave speed, creep compliance coefficients, and retardation times, are calibrated simultaneously, its results are presented in Figure 12. The results of this scenario are also suitable for both types of signals used. However, considering the benefits of reducing the decision-making variables of the optimizer model, it is better to reduce the decision-making variables to the elastic pressure wave speed and the creep compliance coefficients by choosing appropriate known values for the retardation times.

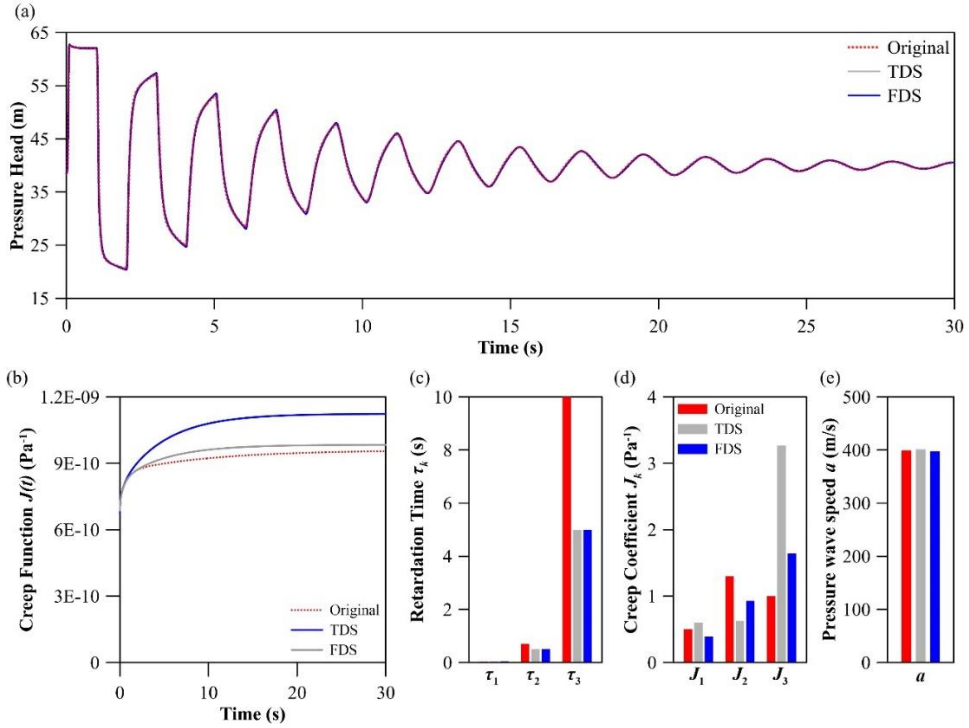


Figure 11. Comparison of (a) pressure signal, (b) creep functions, (c) retardation times, (d) creep compliance coefficients, and (e) elastic pressure wave speed based on known retardation times

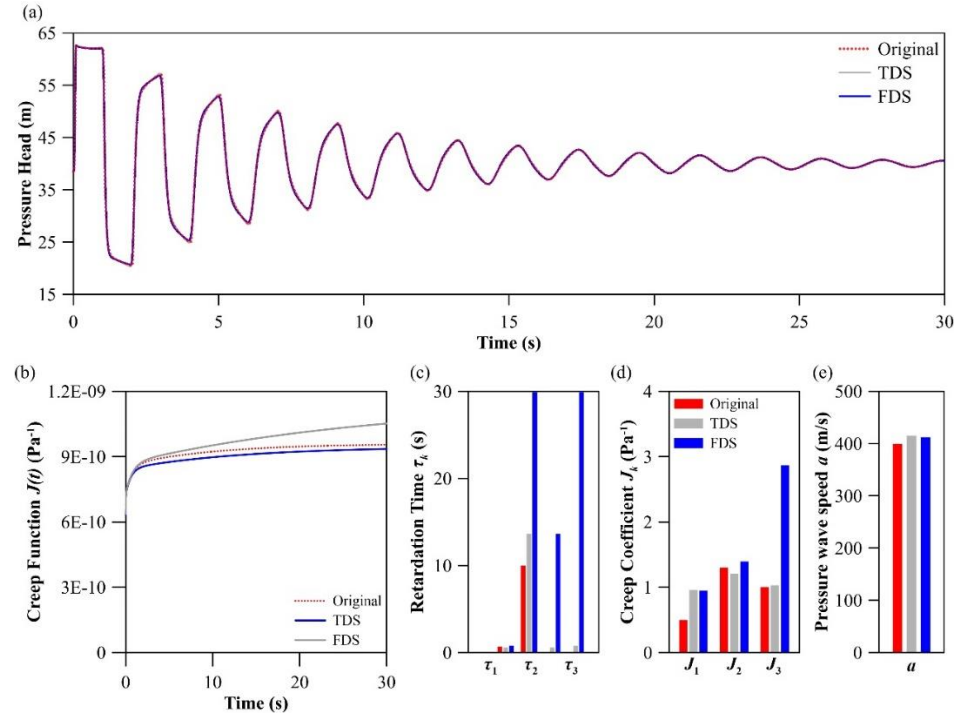


Figure 12 Comparison of (a) pressure signal, (b) creep functions, (c) retardation times, (d) creep compliance coefficients, and (e) elastic pressure wave speed based on calibrated retardation times

3.5. Evaluation based on experimental data

Figure 13 shows the results of time-domain signal-based modeling. Also, the pressure signal in the corresponding frequency domain has been compared with the pressure signal in the time domain. Figure 14 also presents the modeling results based on the frequency domain signal. Figure 15 shows the values of the calibrated creep function. Also, the details of creep function parameters are presented in Table 3. Based on a preliminary analysis, these modelings' values of the retardation times are considered constant as 0.057, 0.4, and 8 seconds, and only the speed of the elastic pressure wave and the creep compliance coefficients for the three Kelvin-Whitt elements has been calibrated. Figure 16 shows the error value of the pressure signal for both methods. The results show that although the pressure signal and the creep function are estimated with appropriate accuracy based on both methods, the modeling accuracy based on the time domain signal is higher.

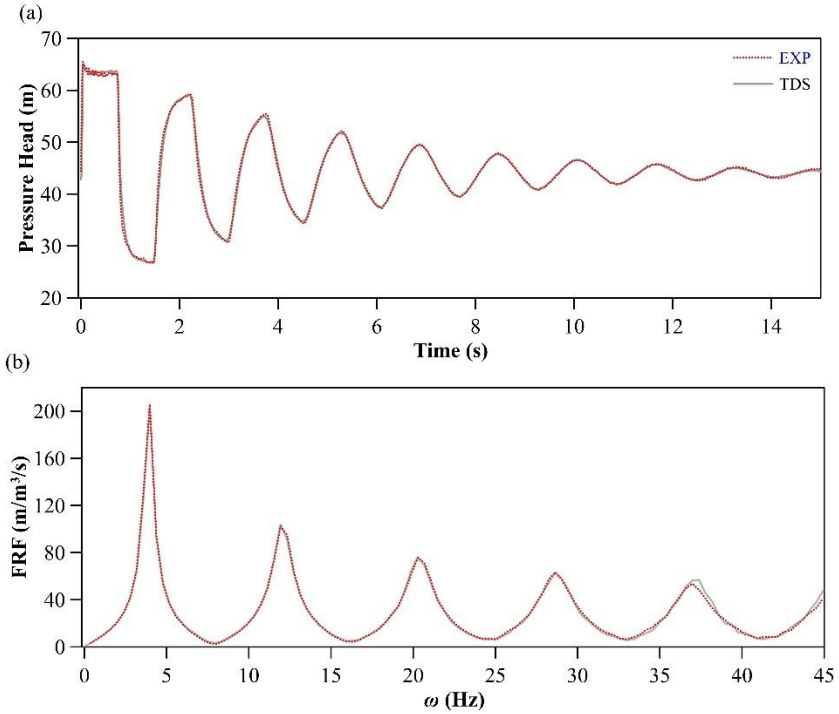


Figure 13. Comparison of pressure signal in (a) time domain and (b) frequency domain for calibrated laboratory sample based on time domain pressure signal

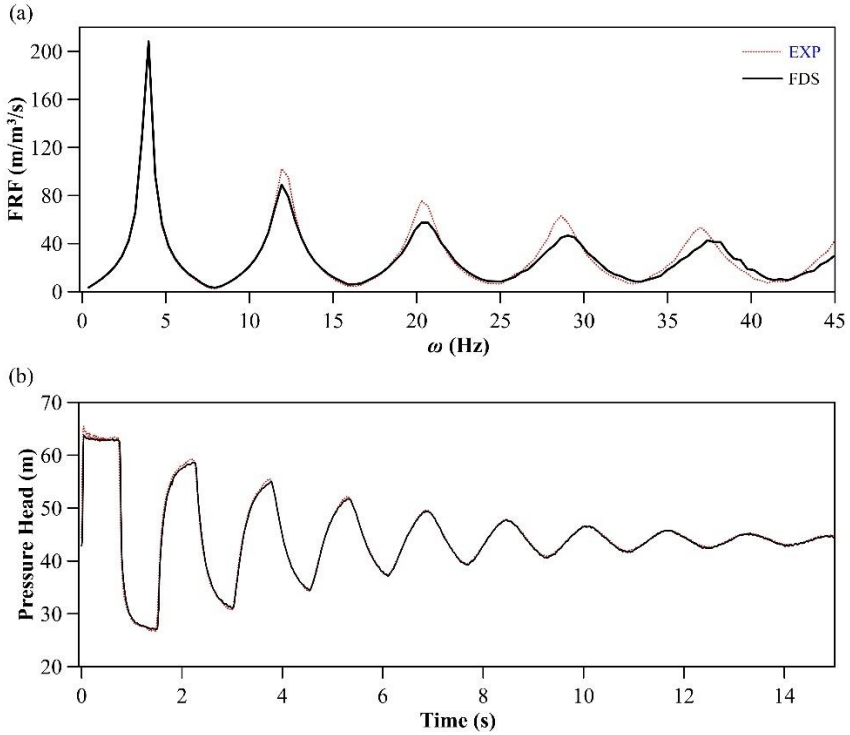


Figure 14. Comparison of the pressure signal in the (a) time and (b) frequency domains for the calibrated laboratory sample based on the frequency domain pressure signal

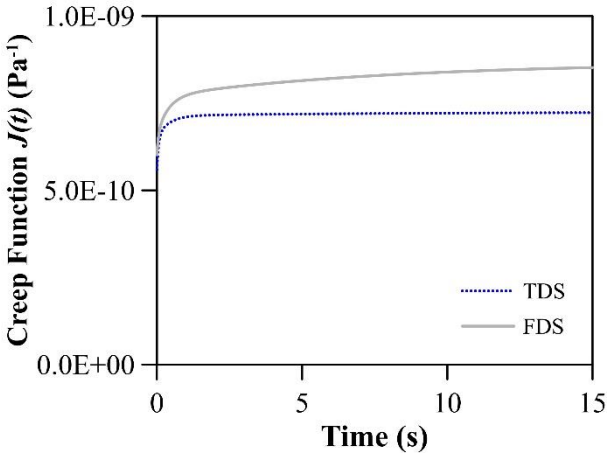


Figure 15. Comparison of the values of the calibrated creep function for the laboratory sample using time and frequency domain signals.

Table 3. Values of the optimized creep parameters for the experimental test

Model	τ_1(s)	τ_2(s)	τ_3(s)	$j_1 \times 10^{-10}$	$j_2 \times 10^{-10}$	$j_3 \times 10^{-10}$	a (m/s)
TDS	0.057	0.4	8	0.930	0.618	0.102	435.44
FDS				0.588	1.085	0.982	421.121

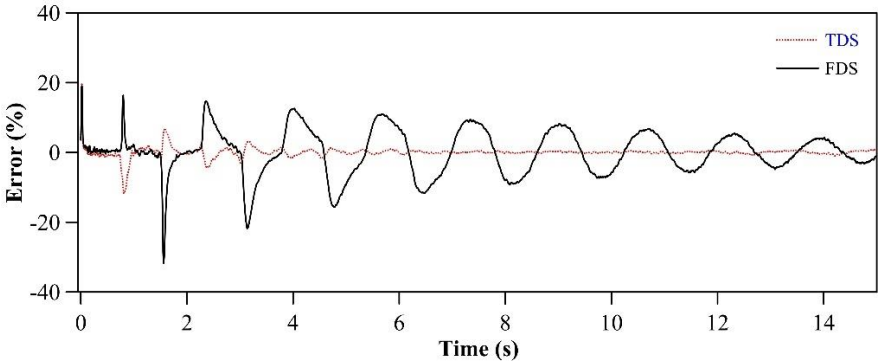


Figure 16 Error between original and calibrated pressure signal and calibrated for both time and frequency domains

4. Conclusion

This research aims to evaluate the creep function estimation of viscoelastic pipes using the inverse transient method based on pressure signals in the time and frequency domain. For this purpose, the effect of various variables, including the number of K-V elements, repeatability, signal sample size, and retardation time optimization, have been investigated. The creep function in this research is considered based on the K-V mechanical element. Also, the genetic algorithm optimization model has been used to determine the decision-making variables. Also, after the preliminary analysis, their results have been validated using an experimental test. The results showed that three K-V elements are sufficient for the pipes on the scale of this research. The effect of the signal size on the accuracy of the creep function estimation showed that with a few initial cycles of the pressure signal in the time domain, the creep function can be determined with reasonable accuracy. Also, the creep function was estimated with appropriate accuracy in the frequency domain with at least the first 40 frequencies of the signal. The evaluation of the effect of optimizing the retardation times showed that the values of these variables can be considered fixed based on similar research or mechanical tests, and their values can be optimized within a reasonable range. The comparison of different models in the time and frequency domain showed that different values for the corresponding creep coefficients were extracted. At the same time, their overall combination provides suitable creep function values. Evaluation of the repeatability of the method used for both signals in the time and frequency domains showed that the model has high stability. The results of this research showed that the estimation of elastic pressure wave speed was estimated with high accuracy in all methods. Results show that both time and frequency domain signals can achieve a reasonable creep function. Although the accuracy of the time domain signal is somewhat higher, the frequency domain signal has a much smaller number of inputs, is suitable for artificial intelligence-based models, and reduces their complexity.

References

1. Keramat, A., Fathi-Moghadam, M., Zanganeh, R., Rahmanshahi, M., Tijsseling, A. S., & Jabbari, E. (2020). Experimental investigation of transients-induced fluid–structure interaction in a pipeline with multiple-axial supports. *Journal of Fluids and Structures*, *93*, 102848.
2. Rahmanshahi, M., Fathi-Moghadam, M., & Haghighi, A. (2018). Leak detection in viscoelastic pipeline using inverse transient analysis. Journal of Water and Wastewater; Ab va Fazilab (in persian), 29(5), 85-97.
3. Williams DJ (1977) Waterhammer in non-rigid pipes: precursor waves and mechanical damping. J Mech Eng Sci 19:237–242.
4. Sharp BB, Theng KC (1987) Water hammer attenuation in uPVC pipe. In: Conference on Hydraulics in Civil Engineering 1987: Preprints of Papers: Preprints of Papers. Institution of Engineers, Australia Barton, ACT, pp 132–136.
5. Brunone B, Berni A (2010) Wall shear stress in transient turbulent pipe flow by local velocity measurement. J Hydraul Eng 136:716–726.
6. Güney MS (1983) Waterhammer in viscoelastic pipes where cross-section parameters are time dependent. In: 4th International Conference on Pressure Surges, England.
7. Meniconi S, Brunone B, Ferrante M, Massari C (2012) Transient hydrodynamics of in-line valves in viscoelastic pressurized pipes: long-period analysis. Exp Fluids 53:265–275.
8. Pezzinga G, Brunone B, Cannizzaro D, et al (2014) Two-dimensional features of viscoelastic models of pipe transients. J Hydraul Eng 140:4014036.
9. Pezzinga G, Scandura P (1995) Unsteady flow in installations with polymeric additional pipe. J Hydraul Eng 121:802–811.
10. Brunone B, Meniconi S, Capponi C (2018) Numerical analysis of the transient pressure damping in a single polymeric pipe with a leak. Urban Water J 15:760–768.
11. Duan H-F, Lee PJ, Ghidaoui MS, Tung Y-K (2012) System response function–based leak detection in viscoelastic pipelines. J Hydraul Eng 138:143–153.
12. Duan H-F, Ghidaoui M, Lee PJ, Tung Y-K (2010a) Unsteady friction and visco-elasticity in pipe fluid transients. J Hydraul Res 48:354–362. https://doi.org/10.1080/00221681003726247.
13. Franke P-G (1983) Computation of unsteady pipe flow with respect to visco-elastic material properties. J Hydraul Res 21:345–353.
14. Keramat A, Tijsseling AS, Hou Q, Ahmadi A (2012) Fluid–structure interaction with pipe-wall viscoelasticity during water hammer. J Fluids Struct 28:434–455.
15. Ramos H, Covas D, Borga A, Loureiro D (2004) Surge damping analysis in pipe systems: modelling and experiments. J Hydraul Res 42:413–425.
16. Covas D, Stoianov I, Ramos H, et al (2004) The dynamic effect of pipe-wall viscoelasticity in hydraulic transients. Part I—experimental analysis and creep characterization. J Hydraul Res 42:517–532. https://doi.org/10.1080/00221686.2004.9641221.
17. Gally M, Gu¨ ney M, Rieutord E (1979) An investigation of pressure transients in viscoelastic pipes.
18. Pezzinga G, Brunone B, Meniconi S (2016) Relevance of pipe period on Kelvin-Voigt viscoelastic parameters: 1D and 2D inverse transient analysis. J Hydraul Eng 142:4016063.
19. Urbanowicz K, Firkowski M, Zarzycki Z (2016) Modelling water hammer in viscoelastic pipelines: short brief. In: Journal of Physics: Conference Series. IOP Publishing, p 12037.
20. Wineman AS, Rajagopal KR (2000) Mechanical response of polymers: an introduction. Cambridge university press.

21. Weinerowska-Bords K (2006) Viscoelastic model of waterhammer in single pipeline-problems and questions. Arch Hydro-Engineering Environ Mech 53:331–351.
22. Weinerowska-Bords K (2007) Accuracy and parameter estimation of elastic and viscoelastic models of water hammer. Task Q 11:383–395.
23. Covas D, Stoianov I, Mano JF, et al (2005) The dynamic effect of pipe-wall viscoelasticity in hydraulic transients. Part II—Model development, calibration and verification. J Hydraul Res 43:56–70.
24. Soares AK, Covas DIC, Reis LFR (2011) Leak detection by inverse transient analysis in an experimental PVC pipe system. J Hydroinformatics 13:153–166. https://doi.org/10.2166/hydro.2010.012.
25. Keramat A, Haghighi A (2014) Straightforward transient-based approach for the creep function determination in viscoelastic pipes. J Hydraul Eng 140:4014058.
26. Weinerowska-Bords K (2015) Alternative approach to convolution term of viscoelasticity in equations of unsteady pipe flow. J Fluids Eng 137.
27. Yao E, Kember G, Hansen D (2016) Water hammer analysis and parameter estimation in polymer pipes with weak strain-rate feedback. J Eng Mech 142:4016052.
28. Yan H, Lam MY, Lee HWJ (2018) Field measurements and theoretical modeling of hydraulic transients in HDPE pipeline with PRV interaction. In: 13th International Conference on Pressure Surges 2018. p 339.
29. Pan B, Duan HF, Meniconi S, et al (2020). Multistage Frequency-Domain Transient-Based Method for the Analysis of Viscoelastic Parameters of Plastic Pipes. J Hydraul Eng 146:1–13.
30. Pezzinga, G. (2023). On the characterization of viscoelastic parameters of polymeric pipes for transient flow analysis. Modelling, 4(2), 283-295.
31. Riyahi, M. M., Rahmanshahi, M., & Ranginkaman, M. H. (2018). Frequency domain analysis of transient flow in pipelines; application of the genetic programming to reduce the linearization errors. Journal of Hydraulic Structures, 4(1), 75-90.
32. Wang X, Lin J, Ghidaoui MS, et al (2020) Estimating viscoelasticity of pipes with unknown leaks. Mech Syst Signal Process 143:106821. https://doi.org/10.1016/j.ymssp.2020.106821.

© 2024 by the authors. Licensee SCU, Ahvaz, Iran. This article is an open access article distributed under the terms and conditions of the Creative Commons Attribution 4.0 International (CC BY 4.0 license) (http://creativecommons.org/licenses/by/4.0/).

Journal of Hydraulic Structures

Volume 10 – Issue 4 – October 2024

Contents:

01 Comparative Assessment of the Computational Fluid Dynamics and Artificial Intelligence Methods for the Prediction of 3D Flow Field around a Single Straight Groyne

Akbar Safarzadeh; Fariborz Masoumi; Zolfaghar Safarzadeh; Maryam Abdoli

26 Adsorption characteristics of NH2-UiO-66 for the removal of hematite inorganic dye from industrial wastewater: Isotherm, thermodynamic, and kinetic study

Abbas Mohammadi; Mehdi Sedighi

46 Experimental study of river morphology downstream of the inclined and vertical grade control structures

Seyed Mohamad Mahdi Shariati; Mehdi Hamidi

61 Prediction of Manning Coefficient in Compound Channels with Converged and Diverged Floodplains using GMDH Model

Sajad Bijanvand; Mirali Mohammadi; Abbas Parsaie

82 Advanced Soft Computing Ensemble for Modeling Contaminant Transport in River Systems: A Comparative Analysis and Ecological Impact Assessment

Jafar Chabokpour

97 Optimization of creep function parameters of viscoelastic pipelines based on transient pressure signal

Ebrahim Sharififard; Mohammad Azizipour; Javad Ahadiyan; Ali Haghighi

Shahid Chamran University of Ahvaz